

Computational Analysis of an Extracorporeal Access
Device and the Effect of Physiological and
Geometrical Conditions on the Risk of Thrombosis

Nicholas Goring



A Thesis Submitted for the Degree of Master of Research
in the
Graduate School of Biomedical Engineering
Faculty of Engineering
University of New South Wales

October 2013

ORIGINALITY STATEMENT

'I hereby declare that this submission is my own work and to the best of my knowledge it contains no materials previously published or written by another person, or substantial proportions of material which have been accepted for the award of any other degree or diploma at UNSW or any other educational institution, except where due acknowledgement is made in the thesis. Any contribution made to the research by others, with whom I have worked at UNSW or elsewhere, is explicitly acknowledged in the thesis. I also declare that the intellectual content of this thesis is the product of my own work, except to the extent that assistance from others in the project's design and conception or in style, presentation and linguistic expression is acknowledged.'

Signed

Date

Abstract

Explanted extracorporeal access devices exhibit different degrees of thrombus formation as a result of different physiological factors *in vivo*. Numerous computational techniques have been developed to predict regions of thrombus formation based on mechanical factors. The prediction of thrombosis in these studies has been limited to isolated cases and specific conditions to validate their use. They have not been implemented for clinical applications and the impact of physiological factors has not been investigated. This thesis explored the effect of physiological factors on the likelihood of thrombus formation in an extracorporeal access device. Four physiological velocity waves (triphasic, biphasic, sharp monophasic, and blunt monophasic) were identified in the femoral artery as a result of different levels of peripheral arterial disease progression. The four waves were used to compare the effect of different pulsatile flow conditions on the likelihood of thrombus formation. This thesis also explored the effect of different geometrical design factors on the likelihood of thrombus formation to optimise its design. Computational fluid dynamics was used to simulate the flow conditions in an occlusive femoral artery with an attached extracorporeal access device. Residence time was used to predict the location and size of thrombus formation on the surface of the cavity. It was shown that the retrograde flow had a considerable impact on the likelihood of thrombus formation, which increased as the integrity of the physiological wave decreased. The predicted location of thrombus was always in the same location, but varied in size depending on the velocity wave. It was also shown that of the device design factors, the angle of the device has the greatest impact on the likelihood of thrombus formation. The computational results were compared to five explanted devices and demonstrated similar locations and sizes of thrombus formation. This thesis examined the likelihood of thrombus formation in a particular extracorporeal access device; however, the methods adapted are beneficial in a wider context and possess a clinical relevance to patient prognostics when prescribing the implantation of a medical device.

Acknowledgements

I would like to extend my thanks to:

- ... Professor Anne Simmons and Associate Professor Tracie Barber, for supervising me in this endeavour and always believing that if I exerted myself I could make it through.
- ... My review panel, Dr. Socrates Dokos, Scientia Professor Nigel Lovell, and Dr. Penny Martens for all of their help and direction over the years.
- ... Joe Tscherry, for all of his help in understanding the complexities of Laser Doppler Anemometry systems.
- ... The workshop staff in the Willis Annexe, for their design recommendations and manufacturing of the experimental rig.
- ... My undergraduate thesis students, especially Josh Yen, who made the laser laboratory an enjoyable experience.
- ... Funding through the Australian Postgraduate Award and Supplementary Engineering Award.

On a personal note, I would never have made it to the end if it weren't for:

- ... My parents, Bill and Ronaldah, for bringing me to Sydney to start this endeavour and encouraging me to finish.
- ... My family for supporting me from across the border.

And, especially:

- ... Lauren.

CONTENTS

CHAPTER 1 - Introduction and Literature Review	1
1.1 <i>Explanted Devices</i>	2
1.2 <i>Haemostasis and Thrombosis</i>	7
1.2.1 Thrombogenesis	7
1.2.2 Mechanical Factors	9
1.3 <i>Measuring Disturbed Flow Conditions</i>	13
1.3.1 Wall Shear Stress	13
1.3.2 Shear Strain Rate	14
1.3.3 Oscillatory Shear Index.....	15
1.3.4 Residence Time	16
1.4 <i>Rationale</i>	17
1.5 <i>Hypothesis and Aims</i>	21
1.6 <i>Thesis Outline</i>	21
CHAPTER 2 - Methods	23
2.1 <i>Computational Model</i>	23
2.1.1 Pathological Conditions	23
2.1.2 Geometry	25
2.1.3 Boundary Conditions	25
2.1.4 Validation	26
2.1.5 Physiological Conditions	26
2.2 <i>Mechanical Indicators of Stagnation</i>	27
2.3 <i>Geometrical Conditions</i>	31
2.3.1 Diameter	31
2.3.2 Angle.....	32
2.3.3 Depth.....	32
2.3.4 Distance	33
2.4 <i>Explanted Extracorporeal Access Devices</i>	33
CHAPTER 3 - Validation and Verification	35
3.1 <i>Verification</i>	37
3.1.1 Mesh Size.....	38
3.1.2 Residual Target.....	40
3.2 <i>Validation</i>	42
3.2.1 Steady Flow Comparison.....	42
3.2.2 Unsteady Flow Comparison.....	44
3.2.2.1 Temporal/Time Step.....	45

3.2.3	Blunt Monophasic Velocity Wave.....	48
CHAPTER 4 -	Results	50
4.1	<i>Physiological Velocity Waves.....</i>	50
4.1.1	Blunt Monophasic Velocity Wave.....	50
4.1.2	Sharp Monophasic Velocity Wave.....	57
4.1.3	Biphasic Velocity Wave.....	63
4.1.4	Triphasic Velocity Wave.....	69
4.2	<i>Vessel Size.....</i>	76
4.2.1	Blunt Monophasic Velocity Wave.....	77
4.2.2	Sharp Monophasic Velocity Wave.....	81
4.2.3	Biphasic Velocity Wave.....	85
4.2.4	Triphasic Velocity Wave.....	88
CHAPTER 5 -	Results	93
5.1	<i>Distance.....</i>	93
5.2	<i>Depth.....</i>	94
5.2.1	Blunt Monophasic.....	95
5.2.2	Sharp Monophasic.....	97
5.2.3	Biphasic.....	100
5.2.4	Triphasic.....	102
5.3	<i>Angle.....</i>	106
5.3.1	Blunt Monophasic.....	106
5.3.2	Sharp Monophasic.....	109
5.3.3	Biphasic.....	112
5.3.4	Triphasic.....	116
5.4	<i>Angle + Depth.....</i>	120
CHAPTER 6 -	Discussion.....	123
6.1	<i>Stagnation.....</i>	123
6.2	<i>Physiological Factors.....</i>	127
6.2.1	Physiological Velocity Waves.....	127
6.2.1.1	Vector Plots	129
6.2.1.2	SSR.....	132
6.2.1.3	Area of Stagnation	133
6.2.2	Vessel Diameter.....	136
6.3	<i>Geometrical Factors.....</i>	138
6.3.1	Distance	138
6.3.2	Depth.....	138
6.3.3	Angle.....	139
6.4	<i>Explanted Extracorporeal Access Devices.....</i>	142
CHAPTER 7 -	Conclusions.....	145
7.1	<i>Future Work.....</i>	146
References	148

LIST OF FIGURES

Figure 1. The cross section of the extracorporeal access device. The grey area identifies the stopper and the red area identifies the cavity created by the device when attached to the femoral artery (PTFE, polytetrafluoroethylene).	2
Figure 2. The explanted device of patient #1.	3
Figure 3. The location of thrombus formation in the cross section of explanted devices #2 and #3.	4
Figure 4. Thrombus formation in the proximal corner of explanted device #2.	4
Figure 5. Thrombus formation in the proximal corner and edge of the stopper in explanted device #3.	5
Figure 6. The location of the thrombosis in the cross section of explanted devices #4 and #5.	5
Figure 7. The occlusive thrombus formed in explanted device #4.	6
Figure 8. The occlusive thrombus formed in explanted device #5.	6
Figure 9. Geometry (cross section) of the computational model.	25
Figure 10. The healthy triphasic femoral velocity wave and three pathological waves.	27
Figure 11. The surface of the cavity that will be analysed for stagnation, including the stopper surface (white) and 1mm of the cavity wall perpendicular to the stopper (black/grey).	31
Figure 12. Comparison of the velocity profile at the throat of the stenosis for the three mesh sizes.	39
Figure 13. Comparison of the velocity profile at the throat of the stenosis for the four residual targets.	41
Figure 14. Comparison of the reattachment length between published data and the computational results (SST).	43
Figure 15. Comparison of the velocity profile at the throat of the stenosis between the published data and computational results for flow at $Re = 500$	43
Figure 16. Comparison of the velocity profile at the throat of the stenosis between the published data and computational results for flow at $Re = 1000$	44
Figure 17. The velocity profile for the pulsatile model, measured upstream of the stenosis.	45
Figure 18. Comparison of the velocity profile, at peak flow, at the throat of the stenosis for the four time steps.	46
Figure 19. Comparison of the centreline axial velocity, at peak flow, downstream of the stenosis between the published data and computational results.	47
Figure 20. Comparison of the velocity profile at the throat of the stenosis between the published data and the computational results.	47
Figure 21. Comparison of the velocity profile at the throat of the stenosis for blunt monophasic velocity wave at four time steps.	48
Figure 22. A cross section view of the velocity field in the cavity for the blunt monophasic velocity wave – as defined in Chapter 2.	51

Figure 23. The area of stagnation, measured using the SSR threshold, on the surface of the cavity at each time step for the blunt monophasic velocity wave.....	53
Figure 24. The location of the area of stagnation, $SSR < 10s^{-1}$, on the surface of the stopper at discrete time steps during the peak flow of the blunt monophasic velocity wave (Red) and for the entire cycle, $SI=1$ (Blue).....	54
Figure 25. The location of the area of stagnation, $SSR < 10s^{-1}$, on the surface of the stopper at discrete time steps at the end of the blunt monophasic velocity wave (Red) and for the entire cycle, $SI=1$ (Blue).....	55
Figure 26. The SI and OSI on the surface of the cavity for the blunt monophasic velocity wave.	56
Figure 27. The location of the area of stagnation calculated from the RT ($RT > 1$) and the SSR threshold for the blunt monophasic velocity wave.....	57
Figure 28. The velocity field in the cavity for the sharp monophasic velocity wave – as defined in Chapter 2.	58
Figure 29. The area of stagnation, measured using the SSR threshold, on the surface of the cavity at each time step for the sharp monophasic velocity wave.	59
Figure 30. The location of the area of stagnation, $SSR < 10s^{-1}$, on the surface of the stopper at discrete time steps during the fastest flow of the sharp monophasic velocity wave (Red) and for the entire cycle, $SI=1$ (Blue).....	60
Figure 31. The location of the area of stagnation, $SSR < 10s^{-1}$, on the surface of the stopper at discrete time steps at the end of the sharp monophasic velocity wave (Red) and for the entire cycle, $SI=1$ (Blue).	61
Figure 32. The SI and OSI on the surface of the cavity for the sharp monophasic velocity wave.	62
Figure 33. The location of the area of stagnation calculated from the RT ($RT > 1$) and the SSR threshold for the sharp monophasic velocity wave.	62
Figure 34. The velocity field in the cavity for the biphasic velocity wave - as defined in Chapter 2.	63
Figure 35. The area of stagnation, measured using the SSR threshold, on the surface of the cavity at each time step for the biphasic velocity wave.....	64
Figure 36. The location of the area of stagnation, $SSR < 10s^{-1}$, on the surface of the stopper at discrete time steps during the forward flow of the biphasic velocity wave (Red) and for the entire cycle, $SI=1$ (Blue).	65
Figure 37. The location of the area of stagnation, $SSR < 10s^{-1}$, on the surface of the stopper at discrete time steps during the change in direction of flow of the biphasic velocity wave (Red) and for the entire cycle, $SI=1$ (Blue).	66
Figure 38. The location of the area of stagnation, $SSR < 10s^{-1}$, on the surface of the stopper at discrete time steps during the reverse flow of the biphasic velocity wave (Red) and for the entire cycle, $SI=1$ (Blue).	67
Figure 39. The location of the area of stagnation, $SSR < 10s^{-1}$, on the surface of the stopper at discrete time steps during the flow at the end of the biphasic velocity wave (Red) and for the entire cycle, $SI=1$ (Blue).	67
Figure 40. The SI and OSI on the surface of the cavity for the biphasic velocity wave.....	68
Figure 41. The location of the area of stagnation determined from the RT ($RT > 1$) and the SSR threshold for the biphasic velocity wave.....	68
Figure 42. The velocity field in the cavity during the forward flow in triphasic velocity wave – as defined in Chapter 2.	69

Figure 43. The area of stagnation, measured using the SSR threshold, on the surface of the cavity at each time step for the triphasic velocity wave.	70
Figure 44. The location of the area of stagnation, $SSR < 10s^{-1}$, on the surface of the stopper at discrete time steps during the forward flow of the triphasic velocity wave (Red) and for the entire cycle, $SI=1$ (Blue).	72
Figure 45. The location of the area of stagnation, $SSR < 10s^{-1}$, on the surface of the stopper at discrete time steps during the change in flow direction flow of the triphasic velocity wave (Red) and for the entire cycle, $SI=1$ (Blue).	73
Figure 46. The location of the area of stagnation, $SSR < 10s^{-1}$, on the surface of the stopper at discrete time steps during the reverse flow of the triphasic velocity wave (Red) and for the entire cycle, $SI=1$ (Blue).	73
Figure 47. The location of the area of stagnation, $SSR < 10s^{-1}$, on the surface of the stopper at discrete time steps during the flow at the end of the triphasic velocity wave (Red) and for the entire cycle, $SI=1$ (Blue).	74
Figure 48. The SI on the surface of the cavity for the triphasic velocity wave.	75
Figure 49. The location of the area of stagnation determined from the RT ($RT > 1$) and the SSR threshold for the triphasic velocity wave.	75
Figure 50. The distribution of the RT magnitude for the four physiological velocity waves.	76
Figure 51. The area of stagnation, measured using the SSR threshold, on the surface of the cavity at each time step for the blunt monophasic velocity profile in the 8mm vessel.	77
Figure 52. Comparison of the blunt monophasic velocity field for the 8mm and 10mm cases at 0.1, 0.15, and 0.2s.	78
Figure 53. Comparison of the area of stagnation, $SSR < 10s^{-1}$, on the stopper surface between the 10mm and 8mm diameter vessels for the blunt monophasic wave (Red) and for the entire cycle, $SI=1$ (Blue).	79
Figure 54. Comparison of the SI and RT ($RT > 1$) between the 10mm and 8mm diameter vessels for the blunt monophasic wave.	80
Figure 55. The area of stagnation, measured using the SSR threshold, on the surface of the cavity at each time step for the sharp monophasic velocity profile in the 8mm vessel.	81
Figure 56. Comparison of the sharp monophasic velocity field for the 8mm and 10mm cases at 0.05, 0.1, and 0.25s.	82
Figure 57. Comparison of the area of stagnation, $SSR < 10s^{-1}$, on the stopper surface between the 10mm and 8mm diameter vessels for the sharp monophasic wave (Red) and for the entire cycle, $SI=1$ (Blue).	83
Figure 58. Comparison of the SI and RT ($RT > 1$) between the 10mm and 8mm diameter vessels for the sharp monophasic wave.	84
Figure 59. The area of stagnation, measured using the SSR threshold, on the surface of the cavity at each time step for the biphasic velocity profile in the 8mm vessel.	85
Figure 60. Comparison of the biphasic velocity field for the 8mm and 10mm cases at 0.1 and 0.25s.	86
Figure 61. Comparison of the area of stagnation, $SSR < 10s^{-1}$, on the stopper surface between the 10mm and 8mm diameter vessels for the biphasic wave (Red) and for the entire cycle, $SI=1$ (Blue).	87
Figure 62. Comparison of the SI and RT ($RT > 1$) between the 10mm and 8mm diameter vessels for the biphasic wave.	88
Figure 63. The area of stagnation, measured using the SSR threshold, on the surface of the cavity at each time step for the triphasic velocity profile in the 8mm vessel.	89

Figure 64. Comparison of the triphasic velocity field for the 8mm and 10mm cases at 0.1, 0.15, 0.2, and 0.25s.	90
Figure 65. Comparison of the area of stagnation, $SSR < 10s^{-1}$, on the stopper surface between the 10mm and 8mm diameter vessels for the triphasic wave (Red) and for the entire cycle, $SI=1$ (Blue).	91
Figure 66. Comparison of the SI and RT ($RT > 1$) between the 10mm and 8mm diameter vessels for the triphasic wave.	92
Figure 67. The area of stagnation on the surface of the cavity, $RT > 1$, with the device at 5D, 10D, and 15D upstream of the femoral occlusion.	94
Figure 68. Comparison of RT ($RT > 1$) and SI on the surface of the cavity for the three cavity depths of 1mm, 3mm, and 5mm for the blunt monophasic wave.	95
Figure 69. Comparison of the area of stagnation, $SSR < 10s^{-1}$, at 0.15s and 0.25s for the three cavity depths of 1mm, 3mm, and 5mm for the blunt monophasic wave (Red) and for the entire cycle, $SI=1$ (Blue).	96
Figure 70. Comparison of the velocity field in the cavity at 0.15s and 0.25s for the three cavity depths of 1mm, 3mm, and 5mm for the blunt monophasic wave.	97
Figure 71. Comparison of the RT ($RT > 1$) and SI on the surface of the cavity for the three cavity depths of 1mm, 3mm, and 5mm for the sharp monophasic wave.	98
Figure 72. Comparison of the area of stagnation, $SSR < 10s^{-1}$, at 0.1s for the three cavity depths of 1mm, 3mm, and 5mm for the sharp monophasic wave (Red) and for the entire cycle, $SI=1$ (Blue).	99
Figure 73. Comparison of the velocity field in the cavity at 0.1s for the three cavity depths of 1mm, 3mm, and 5mm for the sharp monophasic wave.	99
Figure 74. Comparison of the RT ($RT > 1$) and SI on the surface of the cavity for the three cavity depths of 1mm, 3mm, and 5mm for the biphasic wave.	100
Figure 75. Comparison of the area of stagnation, $SSR < 10s^{-1}$, at 0.1s and 0.3s for the three cavity depths of 1mm, 3mm, and 5mm for the biphasic wave (Red) and for the entire cycle, $SI=1$ (Blue).	101
Figure 76. Comparison of the velocity field in the cavity at 0.1s and 0.3s for the three cavity depths of 1mm, 3mm, and 5mm for the biphasic wave.	102
Figure 77. Comparison of the RT ($RT > 1$) and SI on the surface of the cavity for the three cavity depths of 1mm, 3mm, and 5mm for the triphasic wave.	103
Figure 78. Comparison of the area of stagnation, $SSR < 10s^{-1}$, at 0.1s, 0.15s, 0.25s, and 0.3s for the three cavity depths of 1mm, 3mm, and 5mm for the triphasic wave (Red) and for the entire cycle, $SI=1$ (Blue). ...	104
Figure 79. Comparison of the velocity field in the cavity at 0.1s, 0.15s, 0.25s, and 0.3s for the three cavity depths of 1mm, 3mm, and 5mm for the triphasic wave.	105
Figure 80. Comparison of the RT ($RT > 1$) and SI on the surface of the cavity for the three device angles of 45°, 90°, and 135° for the blunt monophasic wave.	107
Figure 81. Comparison of the area of stagnation, $SSR < 10s^{-1}$, at 0.1s and 0.15s for the three device angles of 45°, 90°, and 135° for the blunt monophasic wave (Red) and for the entire cycle, $SI=1$ (Blue).	108
Figure 82. Comparison of the blunt monophasic velocity field in the cavity at 0.1s, 0.15s, and 0.2s for the three device angles of 45°, 90°, and 135°.	109
Figure 83. Comparison of the RT ($RT > 1$) and SI on the surface of the cavity for the three device angles of 45°, 90°, and 135° for the sharp monophasic wave.	110
Figure 84. Comparison of the area of stagnation, $SSR < 10s^{-1}$, at 0.05s and 0.1s for the three device angles of 45°, 90°, and 135° for the sharp monophasic wave (Red) and for the entire cycle, $SI=1$ (Blue).	111

Figure 85. Comparison of the sharp monophasic velocity field in the cavity at 0.05s and 0.1s for the three device angles of 45°, 90°, and 135°.....	112
Figure 86. Comparison of the RT (RT>1) and SI on the surface of the cavity for the three device angles of 45°, 90°, and 135° for the biphasic wave.....	113
Figure 87. Comparison of the area of stagnation, $SSR < 10s^{-1}$, at 0.05s, 0.1s, 0.15s and 0.2s for the three device angles of 45°, 90°, and 135° for the biphasic wave (Red) and for the entire cycle, SI=1 (Blue).....	114
Figure 88. Comparison of the biphasic velocity field in the cavity at 0.05s, 0.1s, 0.15s and 0.2s for the three device angles of 45°, 90°, and 135°.....	116
Figure 89. Comparison of the RT (RT>1) and SI on the surface of the cavity for the three device angles of 45°, 90°, and 135° for the triphasic wave.	117
Figure 90. Comparison of the area of stagnation, $SSR < 10s^{-1}$, at 0.1s, 0.15s, 0.2s, and 0.25s for the three device angles of 45°, 90°, and 135° for the triphasic wave (Red) and for the entire cycle, SI=1 (Blue).	118
Figure 91. Comparison of the triphasic velocity field in the cavity at 0.1s, 0.15s, 0.2s, and 0.25s for the three device angles of 45°, 90°, and 135°.....	120
Figure 92. Comparison of the area of stagnation for all of the device configurations.....	122

LIST OF TABLES

Table 1. Description of the patient characteristics and thrombus formation in the explanted devices.3

Table 2. Summary of studies predicting thrombus formation.20

Table 3. Comparison of the reattachment length downstream of the stenosis for the three mesh sizes.40

Table 4. Comparison of the reattachment length downstream of the stenosis for the four residual targets.41

Table 5. Comparison of the reattachment length downstream of the stenosis for the four time steps.46

Table 6. Comparison of the reattachment length downstream of the stenosis for the blunt monophasic velocity wave at four time steps.49

GLOSSARY

Abbreviations		Range	Threshold / Range
vWF	von Willebrand Factor	--	--
WSS	Wall Shear Stress	--	< 1 MPa
SSR	Shear Strain Rate	--	< 10 s ⁻¹
OSI	Oscillatory Shear Index	0 – 0.5	--
RT	Residence Time	--	> 1
SI	Stagnation Index	0 – 1	--
TAWSS	Time Average Wall Shear Stress	--	--

CHAPTER 1 - INTRODUCTION AND LITERATURE REVIEW

Peripheral vascular disease is the gradual reduction in blood flow to one or more limbs as a result of atherosclerosis [1-9]. In the late stages it progresses to ischaemic ulceration and gangrene [3, 5, 7-9] and it is an important risk factor for lower limb amputation [1, 3, 5, 7, 9]. A novel treatment has been developed to prevent amputation in patients with severe peripheral vascular disease. It aims to stimulate arteriogenesis and collateral growth in the region of the diseased vessels, and restore blood flow to the peripheral limb via high pressure perfusion (or hyper-perfusion). This treatment employs a long-term extracorporeal access device, which remains implanted for the duration of the treatment and facilitates access to the femoral artery. However, the introduction of an extracorporeal access device to the femoral artery creates an environment that increases the risk of thrombosis.

The device exists in two states; active, when perfusion of the lower limb takes place, and inactive, when the device is still attached to the femoral artery but is sealed off between treatments. The inactive device creates a unique cavity adjoining the vessel and can potentially lead to flow conditions suitable for thrombus formation.

1.1 EXPLANTED DEVICES

A schematic of the extracorporeal access device used to provide access to the femoral artery for the hyper-perfusion treatment is shown in Figure 1. It identifies the cross section of the device and the position of the stopper when the device is in the closed state.



Figure 1.The cross section of the extracorporeal access device. The grey area identifies the stopper and the red area identifies the cavity created by the device when attached to the femoral artery (PTFE, polytetrafluoroethylene).

The two layers of polytetrafluoroethylene (PTFE) are used to secure the device to the wall of the femoral artery and make up the wall of the cavity. The stopper in the lumen of the device is placed in line with the silicone tube and closes off the cavity. The dashed line indicates the shape of the cavity (red) when the device is attached to the femoral artery.

Explanted extracorporeal access devices from 5 patients were available for analysis and revealed a range of outcomes ranging from the absence of any sign of thrombosis to solid occlusive thrombus on the stopper surface. Table 1 identifies the known patient characteristics and a description of the thrombus formation in the explanted device. Photos

of the explanted devices were used to show and compare the location and degree of thrombosis in the devices to the computational results.

Table 1. Description of the patient characteristics and thrombus formation in the explanted devices.

Device #	Sex	Age	Description of Thrombus
1	F	62	No thrombus formation
2	---	---	Thrombus formation in the proximal corner
3	---	---	Thrombus formation on the proximal corner and the edge of the stopper surface
4	---	---	Occlusive thrombus
5	M	77	Occlusive thrombus

Figure 2 shows the lumen of explanted device #1, which revealed no signs of thrombus formation anywhere on the lumen of the device. Device #1 was retrieved from a female and it is likely the explanted device performed well as a result of a smaller femoral artery.

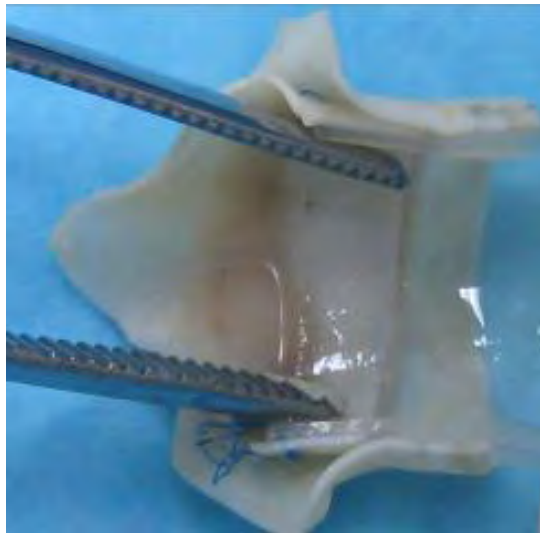


Figure 2. The explanted device of patient #1.

Figure 3 provides an indication of the location of the thrombus formation in the cross section of the device with the stopper present for device #2 and #3.

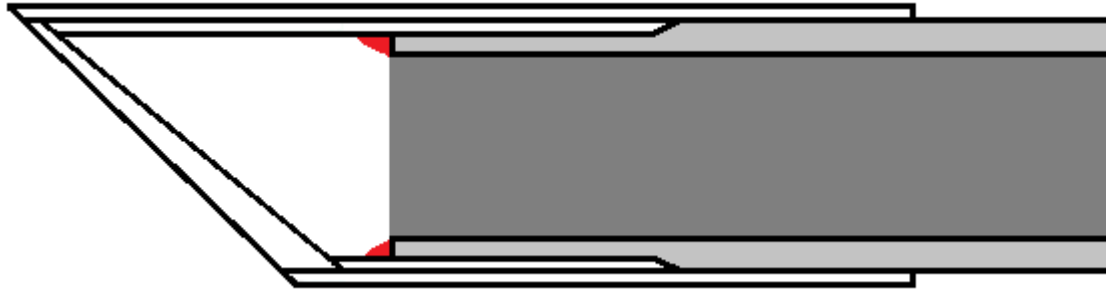


Figure 3. The location of thrombus formation in the cross section of explanted devices #2 and #3.

Figure 4 shows the lumen of explanted device #2, which exhibits the initiation of thrombus formation in the corner of the cavity. It illustrates the early stages of thrombus formation in the cavity. The thrombus is located in the proximal corner of the cavity and the deepest point from the femoral flow. The photo shows some signs of the thrombus extending along the wall of the cavity and around the edge of the stopper surface.



Figure 4. Thrombus formation in the proximal corner of explanted device #2.

Figure 5 shows the lumen of explanted device #3, which shows the progression of thrombus formation around the edge of the stopper surface and along the cavity wall. It

shows thickening of the thrombus in the proximal cavity and around the edge of the stopper.



Figure 5. Thrombus formation in the proximal corner and edge of the stopper in explanted device #3.

Figure 6 provides an indication of the location of the thrombus in the cross section of explanted devices #4 and #5.

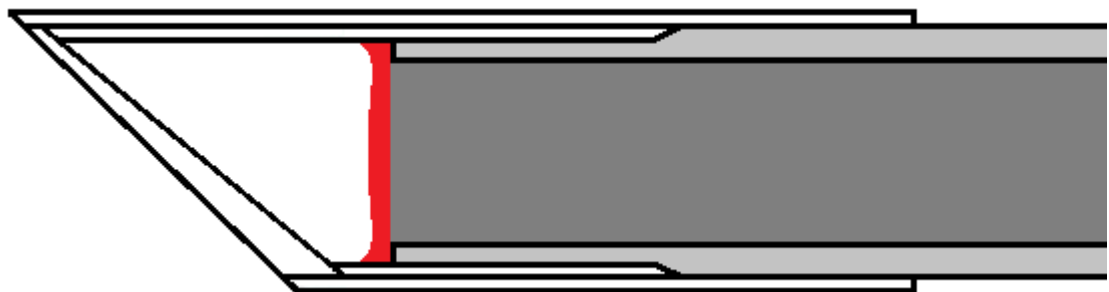


Figure 6. The location of the thrombosis in the cross section of explanted devices #4 and #5.

Figure 7 and Figure 8 shows the thrombus formed in explanted device #4 and #5 respectively, which occlude the entire lumen of the device.



Figure 7. The occlusive thrombus formed in explanted device #4.



Figure 8. The occlusive thrombus formed in explanted device #5.

The thrombus is located on the stopper surface and provides a catastrophic risk to the patient if the thrombus was dislodged. The level of thrombus formation in explanted device #4 and #5 suggests that thrombus formation initiated in the same location as device #3 and extended around the entire edge of the stopper and across the stopper surface.

All of the thrombi in the explanted devices were identified as red blood clots. Red blood clots are composed predominantly of red blood cells and a fibrin mesh and occur due to stagnation in the flow. The lack of any thrombus formation in one patient and the different degrees of thrombus formation in the rest of the patients suggests that there are physiological conditions that support or inhibit the growth of thrombus in the cavity of the device.

A number of explanted devices have revealed different degrees of thrombus formation within the lumen of the device. The contrasting patient outcomes after receiving the device under the same conditions suggest that physiological factors play a significant role towards thrombus formation in the devices. It is therefore important to understand the interaction between physiological factors and mechanical factors and their roles in thrombus formation.

1.2 HAEMOSTASIS AND THROMBOSIS

1.2.1 Thrombogenesis

Haemostasis maintains the blood in a fluid state and limits blood loss through the formation of a clot to repair injury to the vessel [10-12]. It is a protective physiological response of blood exposure to collagen and tissue factor components of the sub-endothelial layers of the vessel wall and ensures the integrity of the cardiovascular system through the balance of pro-coagulant and anti-coagulant forces [11]. The haemostatic response has three major steps in the formation of a blood clot [13-15]:

Vasoconstriction: Immediately following injury to the vessel wall, constriction of the damaged vessel occurs; resulting in slower blood flow in and around the damaged area.

Platelet Plug (primary haemostasis): The platelet plug forms the first layer of the clot and is the result of a series of three events; platelet adhesion, activation, and aggregation [10, 16-19]. Platelet adhesion occurs when endothelial damage exposes blood to collagen and von Willebrand Factor (vWF), which facilitate binding of platelets to the injured vessel wall. The interaction of platelets with the sub-endothelial layer activates the platelets, which release granules into the blood resulting in the activation of more nearby platelets. The activation of platelets results in a change of shape, allowing fibrinogen binding and platelet-platelet interactions, leading to platelet aggregation and the formation of a platelet plug.

Blood Coagulation (secondary haemostasis): The coagulation cascade comprises of three pathways that result in fibrin formation. These are the contact activation pathway (intrinsic), the tissue factor pathway (extrinsic), and the common pathway. The intrinsic and extrinsic pathways both lead to the activation of Factor X, and together with Factor V initiates the final common pathway. The extrinsic pathway occurs through the interaction of plasma factors (Factor VII) with exposed tissue factor in the sub-endothelial layer, which activates the factors and initiates the extrinsic pathway. Coagulation may also be initiated by the intrinsic pathway as a result of the activation of Factor XII by a charged surface or foreign material. The activation of Factor X through the extrinsic or intrinsic pathway leads to the activation of thrombin and subsequent activation of fibrin.

The fibrin mesh, as a result of the coagulation cascade, together with the platelet plug constitutes a blood clot. Originally it was thought that the intrinsic and extrinsic pathways both played an important role in the haemostatic process [20-22]. However, now it is believed the extrinsic pathway is the primary cause of fibrin formation in an injured vessel [11, 22-24]. The intrinsic pathway does not play a role in normal coagulation, but might be important for fibrin formation in pathological processes, such as arterial thrombosis [12].

1.2.2 Mechanical Factors

Haemostasis is the protective physiological response to the injury of a vessel wall through the formation of a blood clot; however, blood clots may form in the absence of injury if the appropriate conditions are presented. Thrombosis can be initiated through several different mechanisms known as Virchow's Triad. The triad was originally developed to illustrate the consequences of thromboembolism, but since then, factors including hypercoagulability, endothelial injury, and disturbed flow conditions have also been identified as the cause of thrombosis [25, 26]. The effect of the device on the flow conditions in the vascular system is of most relevance in device design and implantation. There are two factors relating to the extracorporeal access device that can cause disturbed flow conditions: the progression of peripheral vascular disease resulting in changes to the velocity wave, and the implantation of the device.

The healthy femoral artery exhibits a triphasic velocity wave, which exhibits two phases of positive flow separated by one phase of retrograde flow; however, the extensive nature of the peripheral arterial disease in patients receiving the treatment indicates that the femoral

artery would experience an unhealthy wave. The femoral and iliac arteries are common sites for severe occlusion as a result of peripheral vascular disease [3, 5, 9, 27], which can affect the flow rate in the femoral artery. Spronk et al. [28] investigated the relationship between an occlusion in the aorto-iliac artery and the velocity wave type in the femoral artery. The study identified four different wave types that can exist in the femoral artery, depending on the environment upstream. The four waves are the triphasic, biphasic, sharp monophasic, and blunt monophasic waves [29]. The type of wave in the femoral artery is a marker for the health of the vascular system and healthy femoral arteries exhibit a triphasic or biphasic velocity wave. The four physiological waves represent different stages of arterial disease development in the peripheral limb. The study found that a blunt monophasic velocity wave in the femoral artery was a result of a severe occlusion in the aorto-iliac artery and, despite being considered a healthy wave: a triphasic velocity wave did not eliminate the possibility of some form of occlusion. The patients all had extensive peripheral arterial disease, which would indicate that a monophasic wave is the most likely to be found in the femoral artery in this population group; however, the extent of the disease proximal to the femoral artery is unknown and any of these velocity waves may be present and could affect thrombus formation in the device. Thrombus formation depends on the flow conditions in the cavity and the different velocity waves provide the physiological conditions that could impact the risk of thrombosis in the cavity.

Medical devices introduce the risk of thromboembolism despite anticoagulant therapy [30]. They introduce foreign materials into the vascular system resulting in contact with blood and abnormal flow conditions; two factors that can lead to thrombus formation. The

abnormal flow conditions created by medical devices often provide a suitable environment for thrombus formation.

The structure and appearance of a thrombus depends largely upon the location and local flow conditions. Under normal circumstances the arterial vasculature provides high pressure and high flow conditions that are unfeasible for the formation of a fibrin thrombus; however, the presence of the extracorporeal access device on the femoral artery provides the low flow conditions suitable for a fibrin thrombus to form. Regions of recirculation and stagnation, characterised by low shear rates and long retention times, can trap cells of the blood, and the low shear rates can lead to platelet activation and the formation of a fibrin thrombus [30, 31]. Stagnation in the cavity presents a suitable environment for thrombus formation through the extended residence time of blood cells.

A number of studies [32-44] have recognised that recirculation regions and areas of stagnation can lead to potentially fatal thrombosis, and Rayz et al [45] found good agreement between slow recirculating flow and regions that later thrombosed. These studies focused on identifying regions of stagnation and thrombosis in medical devices including: aneurysm coils, heart valves, artificial blood pumps and ventricular assist devices.

Stagnation is defined by a volume of fluid that remains at a fixed location for an extended period of time, and Longest and Kleinstreuer [46] proposed that particle adhesion is proportional to local particle count, residence time and wall proximity. Friedrich and Reininger [47] investigated thrombin formation on an in vitro indwelling catheter and also

found that regions of thrombus formation always correlated with longest residence time. These studies suggest that slow recirculating flow causes extended residence time, which promotes fibrin thrombus formation [39]. It was determined that regions of recirculation, low fluid motion and trapped fluid contribute to thrombus formation and should be eliminated [32, 37, 41].

Regions of stagnation in medical devices provide mostly detrimental conditions in the vascular system; however, the combination of stagnation and a foreign material has seen beneficial uses. In the case of aneurysms, coils have been introduced to promote regions of stagnation and thrombus formation to avoid rupture of the sac [48-50]. In most cases though, such as mechanical heart valves, vascular assist devices, and stents, thrombus formation presents a catastrophic risk to the patient's life in the form of thromboembolism [51-58].

The presence of the extracorporeal access device creates a unique and unnatural cavity on the femoral artery that is susceptible to stagnation and therefore thrombosis. Disturbed flow conditions coupled with an abnormal geometry and foreign material highly increase the risk of these events. To assess the effect the device has on the flow in the femoral artery, and the flow in the device, it is important to understand the mechanical factors that result in thrombus formation. Hence, identifying the fluid mechanics properties that lead to regions of disturbed flow conditions is necessary to minimise or eliminate the risk of thrombosis.

1.3 MEASURING DISTURBED FLOW CONDITIONS

Disturbed flow conditions (secondary, recirculation, and stagnation) within the vascular system can lead to the development of thrombosis. A number of factors have been established to identify regions of disturbed flow including wall shear stress (WSS), shear strain rate (SSR), oscillatory shear index (OSI), and residence time (RT).

1.3.1 Wall Shear Stress

Texon et al [59] determined that vascular fluid dynamics played a key role in the development of atherosclerosis and Muller- Mohnsen [60] and Caro et al [61] found that low wall shear rates encouraged the formation of atherosclerosis and thrombosis.

Low and oscillating wall shear stresses are believed to play a key role in the formation of atherosclerotic plaque and thrombosis. Stagnation and recirculation are important for the formation of thrombus and these secondary flows are heavily associated with low and oscillating WSS. The combination of low and oscillating flow and abnormal geometry ensures aneurismal sacs are often at risk of developing thrombosis. Rayz et al [62] analysed pulsatile WSS distributions in a computational aneurysm and found low WSS was associated with regions of flow recirculation. The regions of thrombus formation corresponded to regions of low WSS in the computational model. Coils have been inserted into aneurysms in an attempt to promote stagnation and thrombosis to stabilise the sac [44]. Chopard et al [63] analysed the flow in aneurysms and proposed a low shear rate threshold as a key mechanism for thrombus formation.

WSS thresholds have previously been used to identify regions of recirculation and stagnation on the wall, which can lead to atherosclerosis or thrombosis. The WSS is suitable for vascular dysfunctions such as atherosclerosis, intimal thickening, or aneurysms where the wall reacts to abnormal flow conditions. The WSS is important for identifying regions prone to atherosclerosis and aneurismal formation, resulting in a significant change to the wall. It has been used to predict thrombosis, but is not representative of the entire volume of fluid at risk of thrombosis, just the elements along the wall. The WSS is related to the SSR close to the wall via the viscosity of the fluid. Unlike WSS, the SSR takes into account the shear forces due to the wall as well as the shear forces due to the surrounding fluid. The SSR is therefore a measure of the total deformation of the blood and hence a better indication of blood stagnation and potential thrombus formation.

1.3.2 Shear Strain Rate

The SSR threshold can be used to identify a volume, rather than a surface, of fluid at risk of stagnation. The literature [35, 64-66] suggests safe shear rates exist for artificial organs and implants to avoid thrombosis. The application of SSR thresholds rather than the WSS would also make it easier to compare cases with different viscosity models. Corbett et al [35] compared locations of thrombosis in Newtonian and non-Newtonian flow to determine WSS and SSR thresholds. The critical WSS values and corresponding SSR values in these regions resulted in similar SSR values, but considerably different WSS values. The SSR threshold can be used to determine regions of consistent low shear, but is insensitive to the direction of shear. As a result the SRR can identify a region of unidirectional low shear that

does not remain in a fixed location and will not stagnate. For this reason a technique must be used that identifies the potential for a theoretical particle to remain at a fixed location.

1.3.3 Oscillatory Shear Index

Ku et al [67] devised an index, OSI, that could be used to assess the oscillatory nature of flow, based on measurements of the WSS in the carotid bifurcation. Their results indicate that sections of the wall exposed to highly oscillatory flow correspond to regions of atherosclerosis, and sections with little to no oscillations are free of atherosclerosis. The OSI is a measure of the cyclic departure of the wall shear stress vector from its predominant axial alignment. The OSI was first measured in the carotid bifurcation with pulsatile flow in a uniform direction. The oscillating shear is a result of the variation in the flow and the complex geometry creating separation and recirculation. In the case of the carotid artery the term predominant axial alignment is clear as the flow has a uniform direction; however, in other instances such as an abnormal geometry or femoral bifurcation where the pulsatile flow has a reverse phase, the idea of predominant axial alignment is less clear. The equation for the OSI was later adapted by He and Ku [68] for more complex three-dimensional cases.

The OSI compares the average WSS vector against the average of the magnitude of the WSS. A value close to 0.5 indicates a high oscillatory nature in the flow and an OSI close to 0 indicates flow with no reverse flow (purely unidirectional). The OSI by itself is insensitive to the magnitude of the WSS and is often combined with a low WSS threshold to accurately identify regions at risk of atherosclerosis or thrombosis. A number of studies

[64-67, 69-77] have analysed the flow conditions at the carotid bifurcation, which lead to atherogenesis. The studies revealed that factors such as low WSS, low time averaged WSS (TAWSS), and high OSI can describe low velocity regions and disturbed flow, i.e. stagnated, secondary, and reversed flow.

1.3.4 Residence Time

Himburg et al [78] identified a limitation in the use of the OSI, in that regions of high OSI are insensitive to the magnitude of the shear forces. They established a calculation for the time a fluid particle resides at a given location based on the OSI and WSS. They determined that as individual markers for stagnation, sites of low shear rate may not have a high OSI and that sites of high OSI may not consistently experience slow flows. An equation was developed to determine the relative residence time (RT) based on the OSI and TAWSS, such that regions with low TAWSS and high OSI experience large RT. The residence time can also be shown to be inversely proportional to the magnitude of the time averaged shear stress vector. By calculating the residence time it is possible to determine regions along the wall where the fluid is practically stagnant and thrombus formation is possible. Lee et al [79] recommends the use of RT as a robust single metric of low and oscillatory shear; however, this formulation, like the OSI, is still insensitive to the magnitude of the shear stress. For this reason it is important to identify regions of flow that remain in a fixed location and experience low shear rates over the entire cycle.

Rayz et al [62] proposed that a high RT and low shear predicted the location of thrombus formation more accurately than either alone. The RT provides a measure for the time a fluid

element will reside in a given location. The calculation can be used to determine whether a fluid element will remain in the same location for the duration of an entire cycle. Any locations in which the fluid remains for the duration of at least one cycle is deemed to be stagnant and poses a risk for thrombosis. It is therefore necessary to use an indicator of shear in combination with an indicator of residence time to predict the location and size of potential thrombi.

The present study was conducted using computational fluid dynamics models to assess the risk of thrombus formation within the cavity and how it is affected by the velocity wave. Areas of stagnation provide an environment that promotes thrombus formation and a number of mechanical factors that predict these locations have been determined.

1.4 RATIONALE

It has been shown that mechanical indicators for stagnation and thrombus formation have been developed and validated against in vivo outcomes. The prediction of thrombosis has been limited to isolated cases and specific conditions to determine the efficacy of metrics such as RT. The implementation of RT as a practical tool to better understand clinical applications and optimise the prescription of medical devices has not been realised.

The different degrees of thrombus development in the explanted extracorporeal access devices under similar operating conditions suggests that physiological factors play a major role in the likelihood of thrombus formation in the device. The explanted devices reveal that the implantation of an extracorporeal access device relies heavily on the physiological

conditions of the recipient. The variety of outcomes in the explanted devices suggests that the range of physiological conditions exhibited by the patients were not taken into consideration for the implementation of the access device.

These outcomes were used as a platform to analyse the potential causes of altered blood flow conditions as a result of disease progression and the introduction of an extracorporeal access device. This thesis assists in understanding the effect of disease progression and investigates the impact of the velocity wave on the flow conditions in the device. It also examines the possibility to optimise the device by analysing the impact of various design parameters on blood flow conditions in particular; the angle of the device, the depth of the cavity, and the distance of the device from the femoral occlusion.

To the author's knowledge no investigation has been undertaken to determine the effect of a range of physiological factors on the risk of thrombus formation. This thesis examines a particular extracorporeal access device; however, the methods adapted are beneficial in a wider context. The outcomes of this investigation assist in understanding:

- The velocity wave dependence of thrombus formation, which is also of significant importance to other medical devices exposed to vascular flow such as stents, catheters, and balloons.
- The clinical relevance to patient prognostics when prescribing the device, taking into consideration the velocity wave exhibited by the patient.
- The role of device design factors on thrombus formation.

Numerous studies have been conducted to predict thrombus formation and are summarised in Table 2. However these studies have only investigated isolated waveforms in specific environments, and have not analysed the impact that differing waveforms (triphasic, biphasic, monophasic) have on the likelihood of thrombus formation. The thesis examined the role of physiological factors (velocity wave and vessel diameter) and geometrical factors on the likelihood of thrombus formation.

Table 2. Summary of studies predicting thrombus formation.

<i>Reference</i>	<i>Velocity Wave</i>	<i>Geometrical Application</i>	<i>Thrombosis Model</i>
Fraser, Zhang et al. 2010 [80]	Steady	Cannula	Low Shear
Chopard, Ouared et al. 2007 [81]	Steady	Cerebral aneurysm	Low Shear
Zhang, Zhan et al. 2008 [82]	Steady	Axial blood pump	Recirculation
Goubergrits, Affeld et al. 2001 [83]	Steady	Bypass graft	Low Shear
Corbett, Ajdari et al. 2010 [35]	Steady	Step wall transition	Low Shear
Chopard, Ouared et al. 2006 [84]	Steady	Aneurysm	Low Shear
Asztalos, Yamane et al. 2000 [32]	Steady	Blood pump	Stagnation
Yoganathan, Corcoran et al. 1979 [85]	Steady	Heart valve	Low Shear
Chopard, Ouared et al. 2007 [63]	Steady	Aneurysm	Low Shear
Tamagawa, Kaneda et al. 2009 [86]	Steady	Backward facing step	Low Shear
LIU, MA et al. 2010 [87]	Steady	Bifurcation	Low Shear
Goodman, Barlow et al. 2005 [88]	Steady	Step wall transition	Platelet deposition and aggregation
Filipovic, Kojic et al. 2008 [89]	Steady	Stenosis	Platelet deposition and aggregation
Bluestein, Niu et al. 1997 [90]	Steady	Stenosis	Platelet deposition and aggregation
Bedekar, Pant et al. 2005 [91]	Steady	Aneurysm	Platelet deposition and aggregation
Sorensen, Burgreen et al. 1999 [92]	Steady	Vessel	Platelet deposition and aggregation
Kamada, Tsubota et al. 2010 [93]	Steady	Vessel	Platelet deposition and aggregation
Burgreen, Antaki et al. 2001 [94]	Steady	Rotary blood pump	High WSS
Bernsdorf, Harrison et al. 2008 [95]	Steady	Step wall transition	Residence Time
Harrison, Smith et al. 2007 [96]	Steady	Step wall transition	Residence Time
Redaelli, Maisano et al. 2004 [97]	Half sine	Heart valve	Low Shear
Corbett, Ajdari et al. 2010 [34]	Half sine	Step wall transition	Low Shear
Worth Longest and Kleinstreuer 2003 [98]	Sinusoidal	Step wall transition	Platelet deposition and aggregation
Kunov, Steinman et al. 1996 [99]	Pulsatile	Stenosis	Particle Tracking
Hyun, Kleinstreuer et al. 2000 [100]	Physiological	Expansions	Low Shear
Rayz, Boussel et al. 2008 [45]	Patient	Aneurysm	Low Shear
Rayz, Boussel et al. 2010 [62]	Patient	Aneurysm	Residence Time

1.5 HYPOTHESIS AND AIMS

The present study was conducted using computational fluid dynamics models to assess the risk of thrombus formation within the cavity, by implementing different physiological factors and geometrical configurations of the device. The models were used to determine the physiological factors and device configurations that could lead to different degrees of thrombus formation in the devices. It is hypothesised that the presence of retrograde flow in the velocity wave decreases the risk of thrombus formation. It is also hypothesised that the angle of the device is the most important design factor in circumventing thrombus formation. Several aims were implemented to test these hypotheses:

Aim 1. To determine the effect of different pulsatile flow conditions on the risk of thrombus formation.

Aim 2. To determine the effect of the device design parameters on the risk of thrombosis in the extracorporeal access device including:

- Different attachment angles of the device to the femoral artery.
- Different depths of the cavity through the placement of the stopper in the inactive phase.
- Different attachment distances upstream of the femoral occlusion.

1.6 THESIS OUTLINE

Chapter 2 provides an introduction to the computational model and the physiological conditions used to simulate a diseased femoral artery with an extracorporeal access device. It summarises the computational techniques used to analyse the flow in the cavity of the device and predict thrombus formation. This chapter details the physiological and geometrical factors that were analysed to optimise the device function.

Chapter 3 presents the methods and results of the validation and verification of the computational model against published data.

Chapter 4 presents the results for the computational analysis of the physiological factors and the effect on thrombus formation in the cavity.

Chapter 5 presents the results for the computational analysis of the geometrical configurations and the effect on thrombus formation in the cavity.

Chapter 6 discusses the findings of this thesis and provides recommendations for future work.

Chapter 7 presents the overall conclusions from this thesis.

CHAPTER 2 - METHODS

This chapter outlines the computational approach used to determine the effect of physiological and geometrical conditions on the flow and risk of thrombosis in the extracorporeal access device. The aim of the thesis is to assess the effect of different physiological and geometrical conditions on the flow in the femoral artery and their impact on the risk of thrombosis. Computational fluid dynamics software was used to analyse the flow conditions within the cavity and to identify the location and size of stagnation within. Mechanical indicators, which have been established as accurate predictors of thrombosis, were used to analyse the flow in the cavity.

2.1 COMPUTATIONAL MODEL

The state of the vessel under investigation was a diseased femoral artery with a stenosis, suitable for the hyper perfusion treatment. To simulate the conditions in the femoral artery of a patient with the extracorporeal access device, it was necessary to understand the physiological velocity wave, the mechanical properties of the blood, the mechanical properties of the wall, and the implantation of the device.

2.1.1 Pathological Conditions

Arterial vessels have complex structures, which exhibit non-linear hyper or visco elastic and anisotropic characteristics [101]. Despite these properties, arterial vessels are often modelled as an elastic artery [101-103] or as non-deformable rigid vessels [104-107] under certain conditions. The effect of the wall on blood flow has been investigated

extensively and is dependent on the size and state of the vessel. It is well accepted that the compliance of the wall in large arteries has no discernible effect on the flow of the blood and Steinman et al [107] found that the vessel wall elasticity only slightly modifies the flow field. A comparison of rigid and moving wall scenarios by Lee and Xu [101] determined that flow behaviours were qualitatively similar with generally small quantitative differences.

Cardiovascular disease is one of a number of factors that causes stiffening of the arterial walls. The extensive nature of peripheral arterial disease in the patients, particularly in the femoral artery, affects the compliance of the vessel wall. The combination of the size of the vessel and its diseased state provides a reasonable basis to simulate the femoral artery as a rigid wall vessel in the computational model.

The behaviour of blood has been studied comprehensively and has been found to be dependent on the size of the vessel. In large arteries the blood has been shown to behave as a Newtonian fluid due to the high shear rates continually experienced by the blood. The blood in the cavity is subject to low shear rates and it is at this level that the blood behaves as a non-Newtonian fluid. There are several models for the non-Newtonian behaviour of blood (power law, Casson, Herschel-Bulkley, Quesada), all of which provide different behaviours and are subject to different limitations. Corbett et al [35] demonstrated that Newtonian and non-Newtonian models for blood predicted similar shear rate thresholds, below which blood would thrombose. A computational model that simulates blood with a Newtonian fluid was chosen to provide a platform for future comparison with a widely accepted model of the natural behaviour of blood.

2.1.2 Geometry

The hyper perfusion procedure used to treat peripheral arterial disease and prevent amputation of the lower limb is performed in the femoral artery. The computational model simulates a diseased common femoral artery with a severe stenotic occlusion. The model incorporates the presence of the device positioned upstream of the stenosis representing the severe peripheral arterial disease, which prompted the treatment. The stenosis, distal to the device, has a 75% area occlusion and was defined by the function;

$$r = \frac{D}{8} * (3 + \cos(\frac{\pi x}{D} + \pi)) , \quad -D \leq x \leq D \quad \langle 1 \rangle$$

where x is measured from the middle of the stenosis;

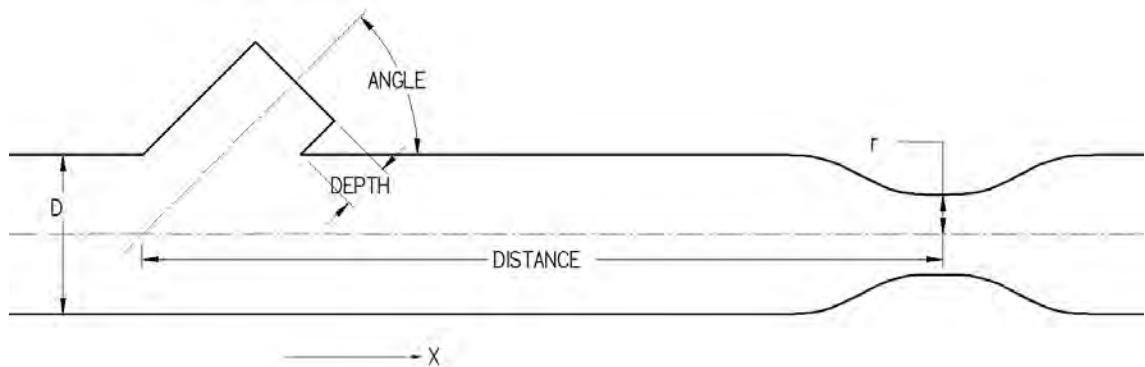


Figure 9. Geometry (cross section) of the computational model.

2.1.3 Boundary Conditions

The blood was represented as an incompressible Newtonian fluid with a density of 1050kg/m³ and viscosity of 0.004Pa.s. The geometry was assumed cylindrical with a rigid, non-slip, and impermeable wall. The length of the inlet segment, 43D, was designed to allow the flow to develop from the plug inlet flow before reaching the

device. The flow is allowed to stabilise from the post-stenotic disturbance before approaching the zero-gradient outlet segment, 45D downstream of the stenosis.

2.1.4 Validation

The transient equations of fluid flow were solved using ANSYS CFX commercial software. The governing equations were formulated for an incompressible, Newtonian fluid in a stenotic femoral artery with an extracorporeal access device attached. The velocity and pressure of the blood flow were calculated by solving the equations of continuity and Navier-Stokes. A refinement study was conducted for the computational model in Chapter 3. The conditions for the model simulation derived from the validation and verification were as follows: At each time step, convergence criteria of 1×10^{-5} were set for relative error associated with determination of velocity and pressure. A constant time step was employed, with 200 time steps per cardiac cycle and three cardiac cycles were required to achieve convergence for the transient analysis. The computational model was validated against the experimental results of Ahmed et al [108] in an analysis of the post-stenotic flow through an artery and the results are shown in Chapter 3.

2.1.5 Physiological Conditions

Stenosis of arterial vessels occurs mainly in medium muscular arteries such as the brachial and femoral artery [109]. The access device is implanted onto the femoral artery for the hyper-perfusion treatment; however the extensive nature of peripheral arterial disease in these patients suggests occlusions may be present upstream of the

femoral artery. Ouriel [3] and Gosling et al [27] describe the extreme nature of peripheral arterial disease and the existence of atherosclerosis in the aorto-iliac vessel.

Spronk et al [28] and O'Neill et al [29] investigated the relationship between an occlusion in the iliac artery and the velocity wave type in the femoral artery. The studies identified four different wave types that can exist in the femoral artery, depending on the environment upstream. They are the triphasic, biphasic, sharp monophasic, and blunt monophasic waves. The four physiological velocity waves resulting from different degrees of upstream occlusion are shown in Figure 10 and were used for the inlet boundary condition.

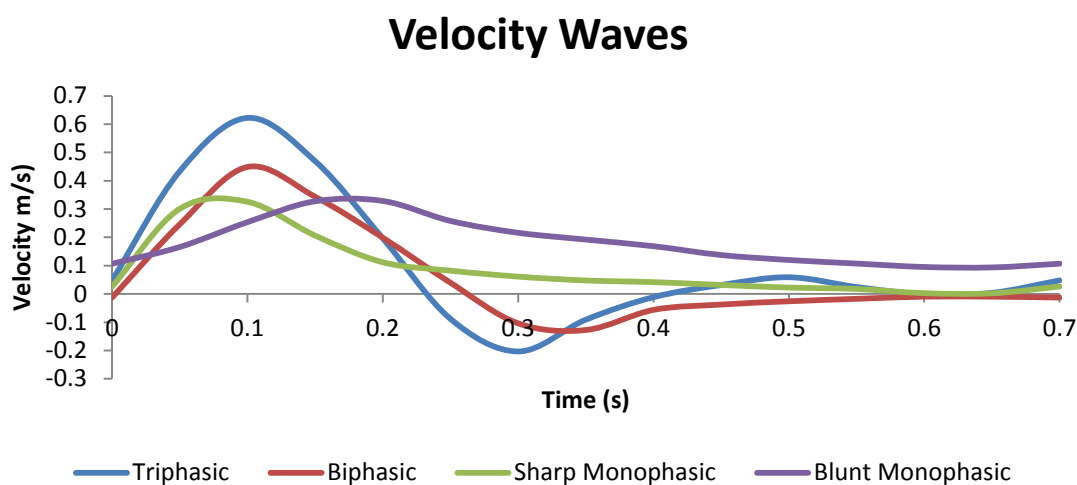


Figure 10. The healthy triphasic femoral velocity wave and three pathological waves.

2.2 MECHANICAL INDICATORS OF STAGNATION

The success of the device was characterised by the risk of thrombosis, which was determined using several established measures including wall shear stress, shear strain rate, oscillatory shear index, and residence time. The effects of the velocity profile on the flow conditions within the cavity of the extracorporeal access device were analysed

with a number of techniques. Vector plots were used to analyse the velocity field in the cavity of the device at specific time steps in the cardiac cycle. The velocity field was used to determine regions of low velocity at each time step and regions exposed to low velocity flow for the entire cycle. The vector plots provide a visualisation of the flow conditions that promote or inhibit stagnation; they highlight the effect of individual aspects of the physiological waves and the importance of retrograde flow to reduce stagnation.

The vector plots provide a qualitative assessment of the area of stagnation in the cavity, but are unable to provide a quantitative assessment. The SSR was used to identify regions of disturbed flow, particularly stagnation, recirculating, and reversed flow. The SSR measures the deformation on the fluid and can determine volumes of stagnation, which present a suitable environment for thrombus formation. This deformation is required to disaggregate blood cells to prevent thrombus formation and a SSR threshold of 10s^{-1} has been measured [35], below which thrombosis occurs. The SSR was used to measure the area of stagnation at each time step in the cycle and was used to identify the components of the velocity wave that promote or inhibit stagnation.

Similar to the vector plots, the SSR threshold was used to identify the individual aspects of the physiological waves that reduced the area of stagnation. The SSR was used in conjunction with the vector plots to provide an indication of the location and size of stagnation in the cavity.

The stagnation index (SI) was used to determine the percentage of the cycle the surface of the cavity was below the SSR threshold. The SI was used to determine the surface

area of the cavity that was below the SSR threshold for the entire cycle, $SI = 1$ (100%). The SI is a good indication of low shear rates, but does not indicate the direction of shear; a region with an SI of 1 may have uniform flow that avoids stagnation.

$$SI = \frac{T_{(SSR < 10s^{-1})}}{T} \quad \langle 2 \rangle$$

The OSI is a frequently used marker to determine areas where the flow remains in a fixed location for the duration of a cycle. The OSI is a measure of the cyclic departure of the WSS vector from its predominant axial alignment, and was developed by He and Ku [68]:

$$OSI = \frac{1}{2} * \left(1 - \frac{\left| \int_0^T \tau_w dt \right|}{\int_0^T |\tau_w| dt} \right) \quad \langle 3 \rangle$$

where τ_w is the total instantaneous WSS vector. A high OSI, though, does not correspond to low velocity flow and may also occur in a region exposed to large shear forces.

The SI and the OSI together provide a good indication of regions that will stagnate. The SI highlights fluid experiencing consistently low shear rates and the OSI highlights flow that remains fixed at a location. There is no threshold for high OSI though, and stagnation can still occur in extremely low flow regions with apparently uniform direction.

The RT was calculated for the surface of the cavity and has been reported as the best single marker for the prediction of stagnation and thrombus formation [62]. Himburg [78] developed the formula for RT based on the OSI and WSS:

$$RT \sim \frac{\mu}{T} [(1 - 2 * OSI) * \langle |\tau_w| \rangle]^{-1} \quad \langle 4 \rangle$$

where μ is the viscosity of the fluid, T is the duration of the cycle, and $\langle |\tau_w| \rangle$ is the time average magnitude of the WSS. RT can also be shown to be inversely proportional to the magnitude of the TAWSS vector:

$$RT \sim \frac{\mu}{T} [\langle \bar{\tau}_w \rangle]^{-1} \quad \langle 5 \rangle$$

A fluid volume was considered at risk of thrombosis if RT was greater than one, which indicates that the fluid remains at the location for the duration of the cardiac cycle. A high RT is a combination of the average WSS and the OSI, which together, would indicate regions of low velocity flow, which does not deviate from a fixed location. The average WSS does not account for large shear forces at individual time steps that may flush out the region of interest. The combination of RT and WSS has been shown to predict locations of thrombus formation better than either measure alone [62]. A similar method will be used for the calculation of RT, but the SSR will be used rather than the WSS. The surface of the device will be considered at risk of thrombus formation with the values of $RT > 1$ and $SSR < 10s^{-1}$ for the cardiac cycle. The surface area of the cavity can be represented as shown in Figure 11.

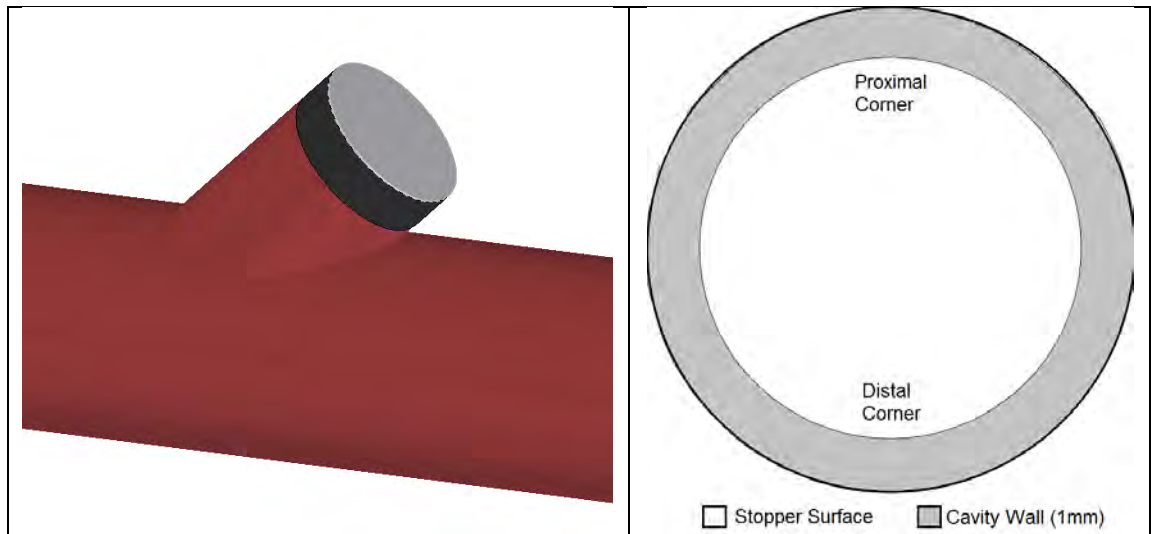


Figure 11. The surface of the cavity that will be analysed for stagnation, including the stopper surface (white) and 1mm of the cavity wall perpendicular to the stopper (black/grey).

The surface area of the cavity with $RT > 1$ and $SSR < 10s^{-1}$ was calculated to compare the risk of thrombus formation between the four velocity profiles and determine the effect of retrograde flow. These measures were used to understand the effect the flow profile has on the risk of thrombosis in the device in the original position. The measures were then used to determine the effect of the device position on the risk of thrombosis, and the optimal position for each flow profile.

2.3 GEOMETRICAL CONDITIONS

2.3.1 Diameter

It has been shown that there is a significant difference between the size of male and female femoral arteries [110, 111]. The diameter of the femoral artery is likely to be different for different patients, if not because of different physical attributes, then at least due to gender differences. The diameter of the vessel is expected to affect the flow into the cavity, which will in turn affect stagnation regions in the cavity. It is expected that the smaller vessel with the relatively larger opening into the cavity, will increase

the likelihood of flushing out the fluid in the cavity and preventing stagnation. The diameter of the vessel was examined at 8 and 10mm.

The extracorporeal access device was investigated under different geometrical configurations, relating to a variety of factors which may influence the success of the attachment to the vessel. The stopper used to close off access to the vessel while leaving the device attached is a flat surface perpendicular to the axis of the device. Due to the angle of the device and the anastomosis of the cylindrical vessel and cylindrical device, a unique cavity is created on the side of the vessel. The size of the cavity is dependent on three factors; the angle of the device, the depth of the stopper, and size of the vessel. These factors were used to determine the optimal position of the device for each physiological wave to reduce the risk of thrombus formation.

2.3.2 Angle

The angle of the device will play a significant role on the susceptibility of thrombus growth in the cavity. The angle of the device has the greatest effect on the shape of the cavity of all the factors. The shape of the cavity will determine the flow conditions within, and with the reverse component of the triphasic and biphasic velocity profiles, the orientation of the device plays a large role in the local fluid mechanics. The device will initially be examined at angles of 45, 90 and 135°.

2.3.3 Depth

The depth of the cavity is an uncertain factor in the attachment of the device to the vessel, due to factors such as vessel thickness and variability in surgical precision. The depth of the cavity is expected to provide a larger region of low velocity recirculation or

stagnation. The presence of the cavity will only cause problems for the natural flow of the femoral artery and as such it is expected that as the depth increases so too will the risk of thrombosis. The deeper the cavity is the less likely the blood will be washed out or even disturbed. The cavity will initially be examined with depths of 1, 3 and 5mm from the vessel wall on the nearest side.

2.3.4 Distance

The distance of the device from the stenosis is expected to play a role in the likelihood of a thrombus developing in the cavity. Due to the reverse flow component of the physiological wave in the femoral artery and the jetting of flow experienced through a stenosis, the location of the device relative to the stenosis may affect the flow conditions in the cavity. The device will initially be examined at distance of 5D, 10D, and 15D upstream from the stenosis.

2.4 EXPLANTED EXTRACORPOREAL ACCESS DEVICES

The explanted extracorporeal access devices presented different level of thrombus formation in the lumen of the device. The structure and appearance of a thrombus depends largely upon the location and local flow conditions. Arterial thrombi typically form at sites of endothelial injury and are exposed to high flow conditions. These conditions result in a thrombi with a composition dominated by platelet aggregates [112], which are identified as white clots. In contrast, venous thrombi are the result of flow stagnation and the composition is dominated by the fibrin mesh and red blood cells [17, 112], which are identified as red clots [12, 113]. The thrombi in the explanted

devices were identified as red, which confirms that stagnation is the cause of thrombus formation in these devices.

The explanted extracorporeal access devices were analysed to determine the relationship between physiological conditions and thrombus formation in the cavity. The extracorporeal access device was implanted under the same conditions for all the patients, which suggests that physiological conditions are responsible for the variation in the outcome of the devices. The explanted extracorporeal access device and patient characteristics were analysed to determine any factors that would promote or inhibit thrombus formation in the device. The physiological conditions that can affect the outcome of the device are the velocity wave and the diameter of the vessel.

The 8 combinations of the four physiological waves and two vessel diameters were analysed and compared to the explanted extracorporeal access devices to explain the different levels of thrombus formation. The different outcomes in the explanted extracorporeal access devices raise questions about the design and use of the device. Was the device optimised for the haemodynamic environment in the femoral artery or for the convenience of treatment? Were the physiological conditions of the patients (velocity wave, size of the vessel) taken into consideration? Is it reasonable to assume all patients exhibit a monophasic velocity wave? What velocity wave was the device designed for? The physiological and geometrical analysis of the extracorporeal access device was used to investigate these concerns and to provide an insight into the optimal device parameters for the physiological conditions.

CHAPTER 3 - VALIDATION AND VERIFICATION

Computational fluid dynamics was used to simulate the in vivo fluid flow to determine information about the flow field. The computational model must be validated and verified before it can be accepted as an accurate representation of the in vivo conditions. Validation and verification is a process for the quality assurance of the computational model. Validation assesses whether the model is an accurate representation of the physical reality and verification assesses whether the computational model is accurately solved.

A verification assessment investigates the process in which the computational model is solved. Computational models are solved using the Navier-Stokes equations, which must converge at each time step for the model to solve; each time step is divided into iterations, for which the equations are solved and the residuals calculated. The residuals must fall below a threshold value (usually several orders of magnitude) before the solution for the time step is considered to have converged. Convergence criteria were tested to ensure the accuracy and efficiency of the computational model.

A grid refinement study is required to ensure the computational solver provides a suitable level of accuracy. A refinement study of the mesh and validation of the turbulence model was necessary to ensure accuracy and efficiency of the simulation.

The resulting model could then be used to analyse the effect of the device position and velocity profile on the flow in the device cavity.

A grid refinement study analyses the change in the flow field, as a result of increasing the detail of the computational model through; the number of elements, the time step, and the residual target. The residual target must be set at an appropriate level to ensure the accuracy of the flow field. The time step is dependent on the mesh size, as a suitable value for the time step must be chosen such that the flow field is accurately calculated. The mesh size, residual target, and time step are tested individually and reduced until an increase in detail yields very little change in the result.

The computational model simulates the conditions of the in vivo situation including the geometry, flow conditions, turbulence model, and fluid properties. These properties are a representation of the in vivo conditions and the model will be validated if the flow conditions in the model are in agreement with either the in vivo flow or simulated in vitro flow. The flow conditions can be compared by using a key aspect of the flow field at an important location such as the velocity profile or the recirculation length under disturbed flow conditions.

Validation against published data was conducted to ensure acceptable conditions were used in the computational model to simulate the in vivo flow. Ahmed and Giddens [108] examined pulsatile flow through a stenosed vessel both computationally and experimentally and the results were used to validate the computational model. Once validated against the published data, it was acceptable to use similar conditions to analyse the flow through the stenosed femoral artery with the device attached upstream.

The geometry for the stenotic femoral artery is based on the experimental study by Ahmed and Giddens [108, 114], which was replicated in a computational model by Ryval et al [115]. To validate the model the geometry must be an accurate representation of a diseased femoral artery and the characteristics of the blood flow must match those measured in the femoral artery. These properties were discussed in Chapter 2 and the system was modelled as a rigid walled diseased femoral artery with Newtonian blood and a physiological velocity wave. The boundary conditions of the model were discussed in Chapter 2 and correspond to similar conditions in the experimental setup of Ahmed and Giddens [108, 114] and the computational setup of Ryval et al [115]. The model incorporates a rigid wall vessel with an incompressible Newtonian fluid to replicate blood.

3.1 VERIFICATION

ANSYS CFX was used to solve the computational model. The two-equation models offer sufficient levels of accuracy, complexity and robustness. All $k-\omega$ models provide automatic near wall treatment of the boundary condition; because of this the SST model, an extension of the $k-\omega$ model was chosen, as it provides a better resolution of near wall effects than the standard model. The SST turbulence model was designed to give a highly accurate prediction of the onset of flow separation, which occurs downstream of the stenosis and during flow reversal, and is an important consideration for the situation.

A very fine computational mesh (3,900,000 hexahedral elements) was designed, taking into consideration the requirements for near wall conditions and the degree of accuracy

required for the final model with the device attached. Ryval et al [115] implemented a much coarser mesh and used a residual target of 1×10^{-3} , but due to the size of this mesh the initial residual was chosen as 1×10^{-5} .

The flow through the stenosis causes recirculation immediately downstream of the occlusion. The velocity profile at the throat of the stenosis and the reattachment downstream of the stenosis provide the ideal markers for the refinement study. The reattachment length can be determined by measuring the WSS around the stenosis. The recirculation region is marked by negative WSS and reverse flow in the velocity profile. The flow through the stenosis causes a drastic increase in the WSS at the throat of the stenosis, which then drops quickly in the recirculation region. The size of the reattachment point depends on the Reynolds number of the steady flow and provides a marker to assess the mesh size, residual targets and time step. Convergence of the criteria is achieved when the change in value of the recirculation length and velocity profile is less than 5% for the mesh size and 1% for the residual target and time step.

3.1.1 Mesh Size

The mesh size is an important characteristic of the computational model. The near wall conditions require a sufficient number of grid nodes within the boundary layer to accurately calculate the flow. The size of the elements near the wall are particularly small, however a model comprised of volumes that small would be computationally expensive. The size of the volumes grows toward the centre of the model, in the core of the vessel, where the velocity gradients are lower. The growth of adjacent volumes must be controlled and maintain a similar shape otherwise the accuracy of the model will suffer. The size of the mesh was investigated at different levels of; 3.9×10^6 elements

(Fine), 1.1×10^6 elements (Medium), and 2.4×10^5 elements (Coarse). The mesh size was determined by doubling the edge lengths on the face of the elements.

Figure 12 compares the velocity profile at the throat of the stenosis for the three mesh sizes using laminar Reynolds flow of 500. It shows very little variation in the velocity as the mesh is refined. The data in Table 3 compares the reattachment length of the flow downstream of the stenosis for the three mesh sizes using laminar Reynolds flow of 500. The percent change of 1.9% in the reattachment length from 1.1×10^6 elements to 3.9×10^6 elements suggests that these meshes are sufficient to ensure the flow field is accurately calculated.

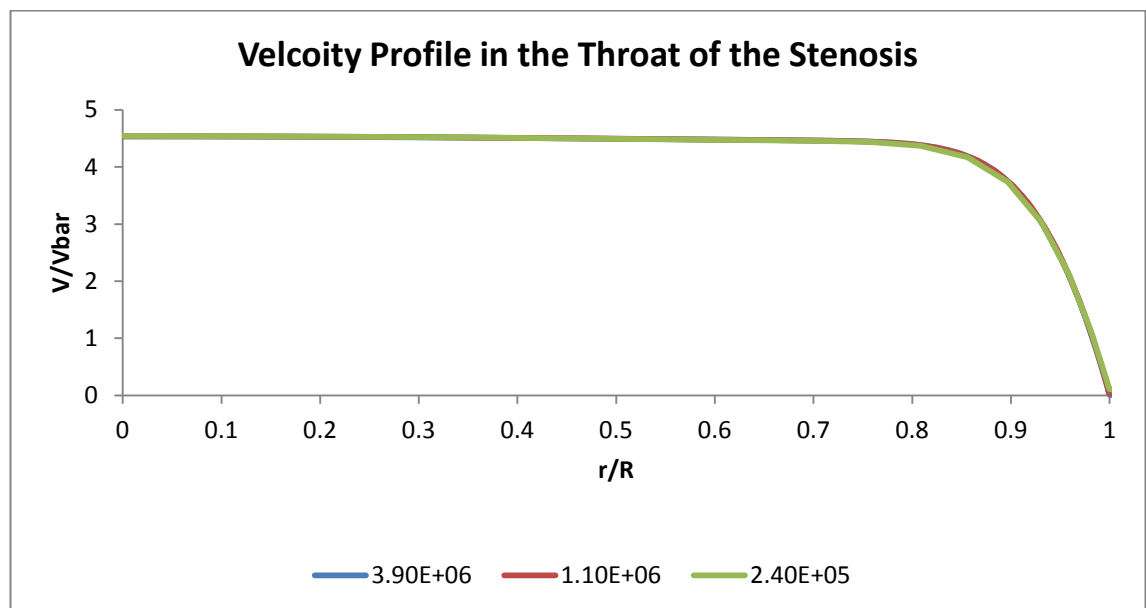


Figure 12. Comparison of the velocity profile at the throat of the stenosis for the three mesh sizes.

Table 3. Comparison of the reattachment length downstream of the stenosis for the three mesh sizes.

Number of Elements	Reattachment Length, L/D	% Change
240,000 (Coarse)	11.8	
1,100,000 (Medium)	10.3	12.5%
3,900,000 (Fine)	10.1	1.9%

3.1.2 Residual Target

The residual target controls the accuracy of the flow in the computational model. It is the most important measure of convergence as it relates directly to whether the equations have been solved. The smaller the residual target is the more accurate the equations are solved in each iteration; however, the accuracy of the model affects the time it takes to solve each iteration. The accuracy of the model must be weighed against the time to solve the model. As the residual is minimised the value of the two markers is expected to reach an asymptotic value. The residual target was analysed at 1×10^{-3} , 1×10^{-4} , 1×10^{-5} , and 1×10^{-6} . The velocity profiles at the throat as well as the reattachment point downstream of the stenosis were used to compare the accuracy of the flow and to determine convergence.

Figure 13 compares the velocity profile at the throat of the stenosis for the four residual targets at $Re = 500$. There is very little variation in the velocity as the residual target is reduced.

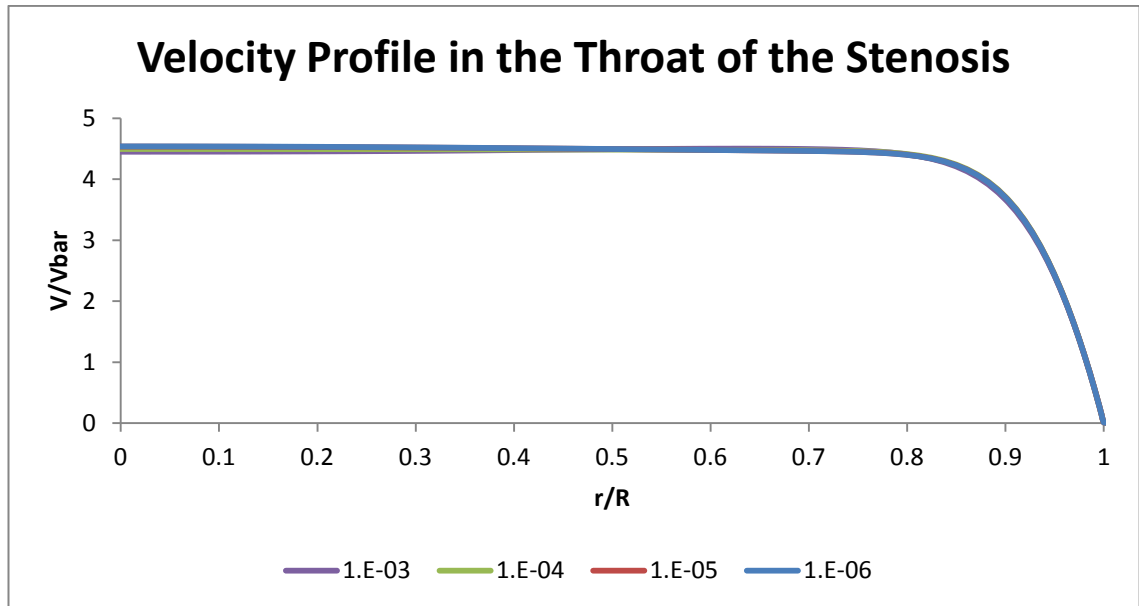


Figure 13. Comparison of the velocity profile at the throat of the stenosis for the four residual targets.

The data in Table 4 compares the reattachment length of the flow downstream of the stenosis for the four residual targets at Reynolds flow of 500. The percent change of 1.0% in the reattachment length from 1×10^5 to 1×10^6 suggests that these values are sufficient to ensure the flow field is accurately calculated.

Table 4. Comparison of the reattachment length downstream of the stenosis for the four residual targets.

Residual Target	Reattachment Length, L/D	% Change
1e-3	3.1	
1e-4	9.3	66.0%
1e-5	10.1	8.7%
1e-6	10.2	1.0%

3.2 VALIDATION

Ryval et al [115] used the reattachment length and velocity profiles of flow through a stenosis to validate the computational model against Ahmed and Giddens [114]. The steady flow was analysed between Reynolds Numbers of 500 and 2000 and was used to establish an appropriate turbulence model for the computational model.

3.2.1 Steady Flow Comparison

The experimental results of Ahmed and Giddens recorded the recirculation length at Reynolds numbers of 500, 1000, and 2000. The flow at these three Reynolds numbers were analysed for validation of the computational model against the computational model of Ryval et al and the experimental results of Ahmed and Giddens and the results are shown in Figure 14.

The reattachment length for steady flow at Reynolds flow of 500 was calculated using a laminar computational model. The result was compared to the results of Ryval et al and found good agreement with a reattachment length of 11. The reattachment length was also calculated at Reynolds numbers of 500, 1000 and 2000 using a SST turbulence model and compared to the experimental results of Ahmed and Giddens and the computational results of Ryval et al. The results show good agreement with the computational model of Ryval et al and the experimental results, except for the experimental result at Reynolds 1000.

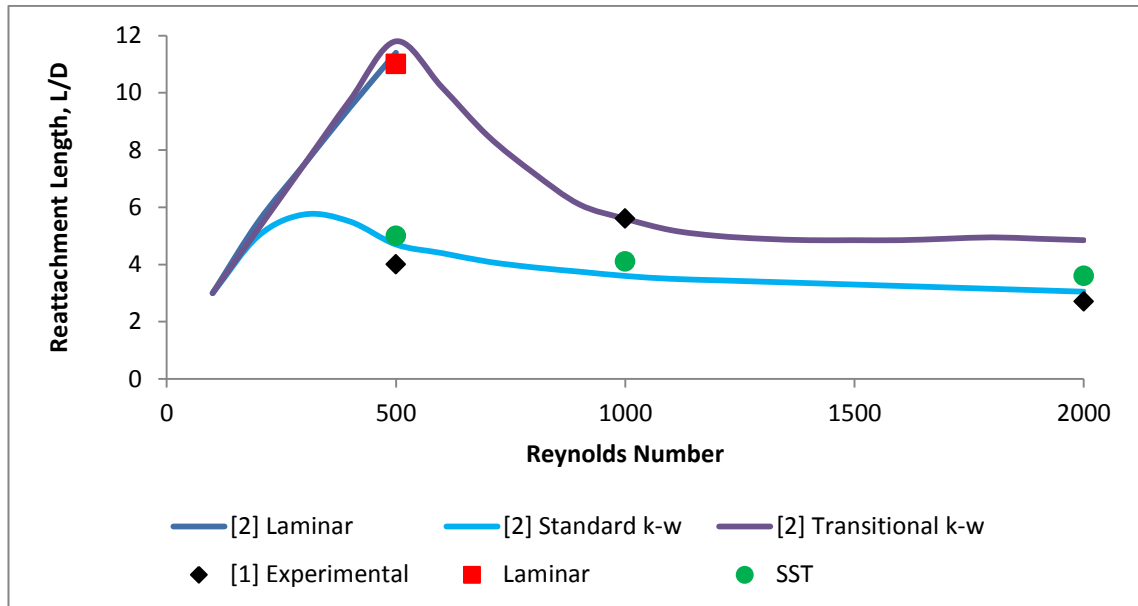


Figure 14. Comparison of the reattachment length between published data and the computational results (SST).

The velocity profile at the throat of the stenosis, non-dimensionalised by the upstream average velocity across the tube, was plotted against the dimensionless radius at Reynolds numbers of 500 (Figure 15) and 1000 (Figure 16).

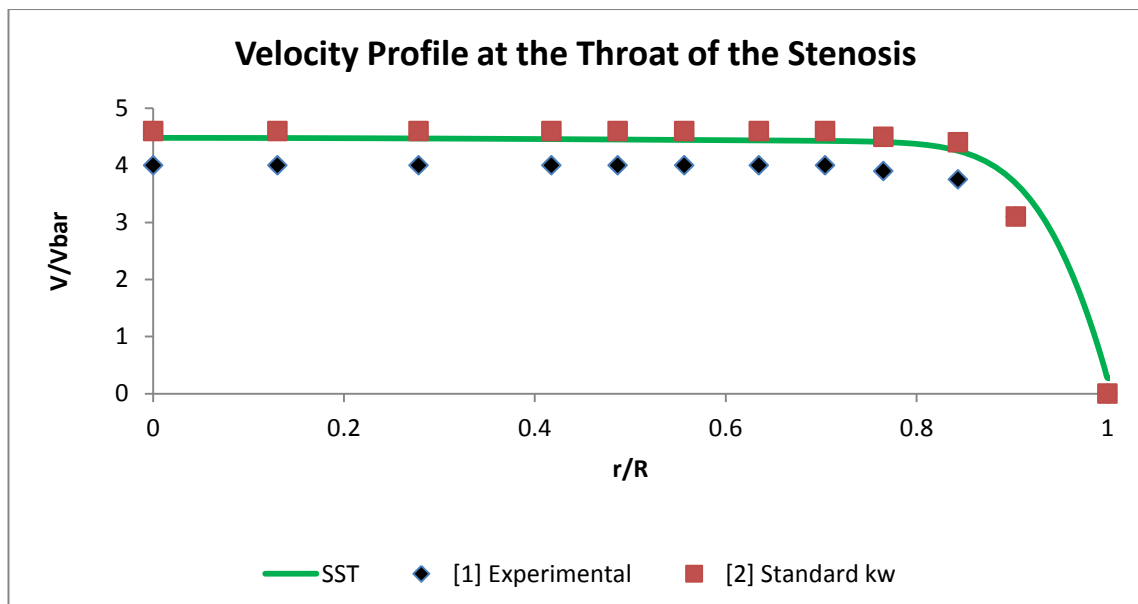


Figure 15. Comparison of the velocity profile at the throat of the stenosis between the published data and computational results for flow at $Re = 500$.

All of the results from the SST model under steady flow analysis measure comparable results to the $k-\omega$ model used by Ryval et al and the experimental results of Ahmed and Giddens.

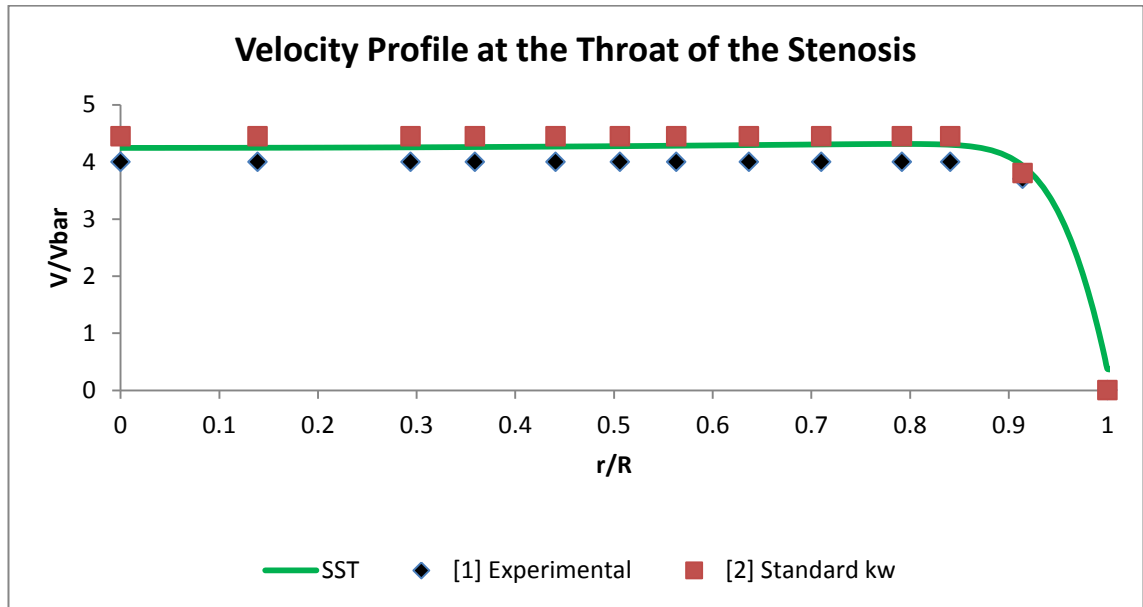


Figure 16. Comparison of the velocity profile at the throat of the stenosis between the published data and computational results for flow at $Re = 1000$.

3.2.2 Unsteady Flow Comparison

The computational model was also analysed under pulsatile velocity conditions to ensure validity for the physiological velocity waves. Figure 17 shows the developed velocities upstream of the occlusion for both Ahmed and Giddens [108] and the SST model as grey and black lines respectively. The maximum and minimum Reynolds Numbers were 1000 and 200, based on the upstream centreline velocity.

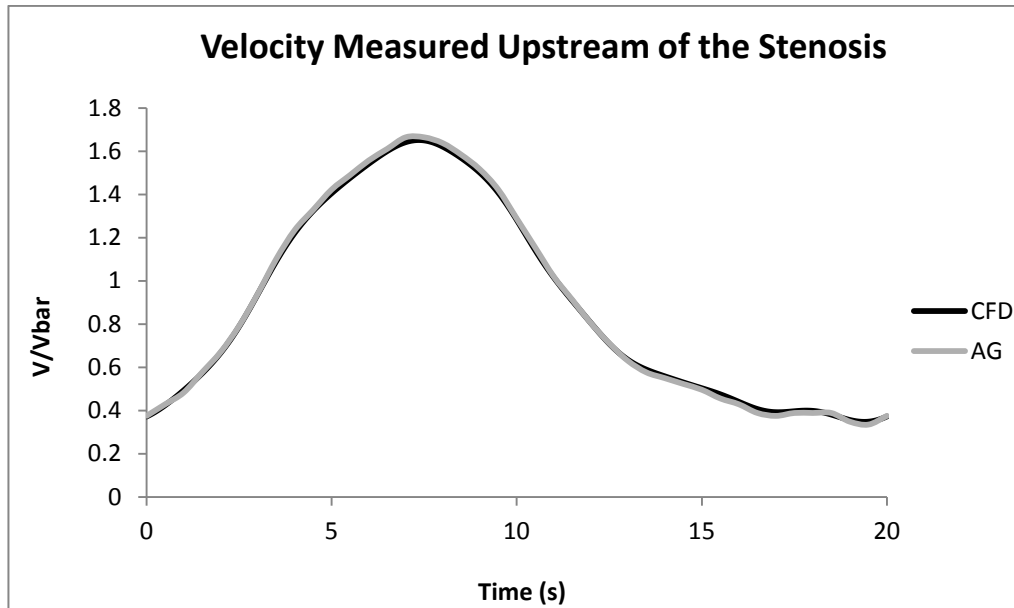


Figure 17. The velocity profile for the pulsatile model, measured upstream of the stenosis.

3.2.2.1 Temporal/Time Step

The time step associated with the mesh size is another important factor for an accurate model. There is a strong interaction between the modelling errors and the time and space resolution of the grid. If the time step is too large then the effect of a characteristic of the flow (e.g. velocity, pressure) may not be accurately calculated at the element border. If the time step is too large the change in the characteristic may occur over two elements rather than one and inaccurately determine the flow characteristics for the mesh size and geometry. The temporal resolution was investigated for time steps of 2, 1, 0.5, 0.25 seconds.

Figure 18 shows the velocity profile in the throat of the stenosis for the four time steps. The results show little variation in the in the results as the time step is lowered.

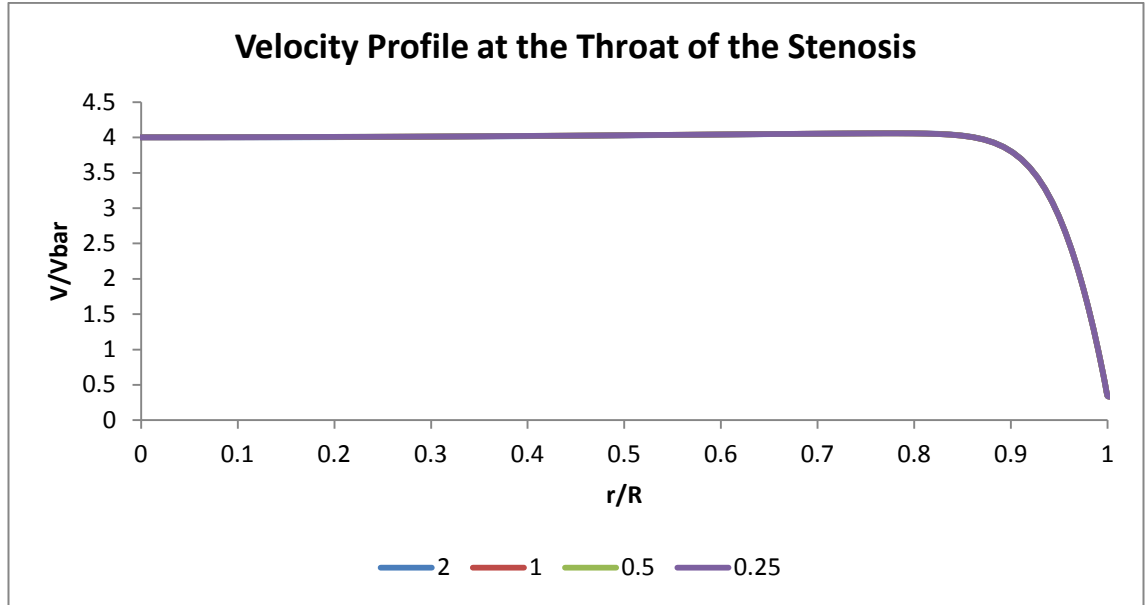


Figure 18. Comparison of the velocity profile, at peak flow, at the throat of the stenosis for the four time steps.

Table 5 shows the reattachment length downstream of the stenosis for the four time steps. The percent change of 0.2% in the reattachment length from 0.5s to 0.25s suggests that these values are sufficient to ensure the flow field is accurately calculated. The reattachment point at the peak flow in the pulsatile cycle is approximately 5.2 diameters downstream of the stenosis compared to Ahmed and Giddens who reported a value of 5-6 diameters downstream of the stenosis.

Table 5. Comparison of the reattachment length downstream of the stenosis for the four time steps.

Time Step	Reattachment Length, L/D	% Change
2	5.36	
1	5.27	1.586%
0.5	5.19	1.574%
0.25	5.18	0.212%

Figure 19 compares the centreline axial velocity, non-dimensionalised by the average of the maximum and minimum upstream velocity, downstream of the stenosis throat between the computational model and published data. Figure 20 compares the velocity

profile in the throat of the stenosis between the computational model and published data at the peak flow in the cycle.

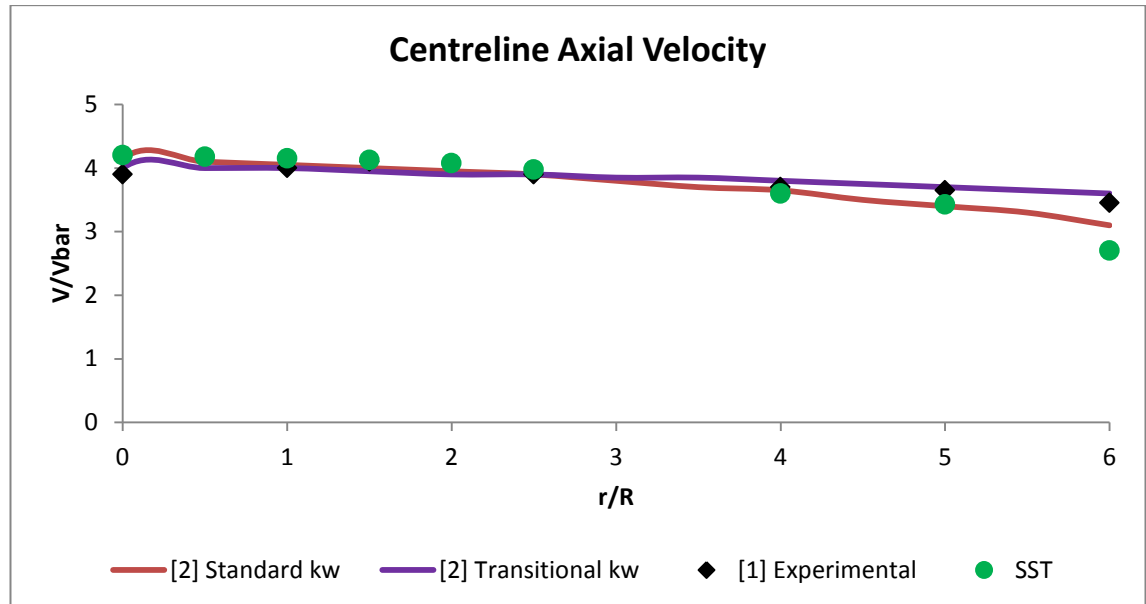


Figure 19. Comparison of the centreline axial velocity, at peak flow, downstream of the stenosis between the published data and computational results.

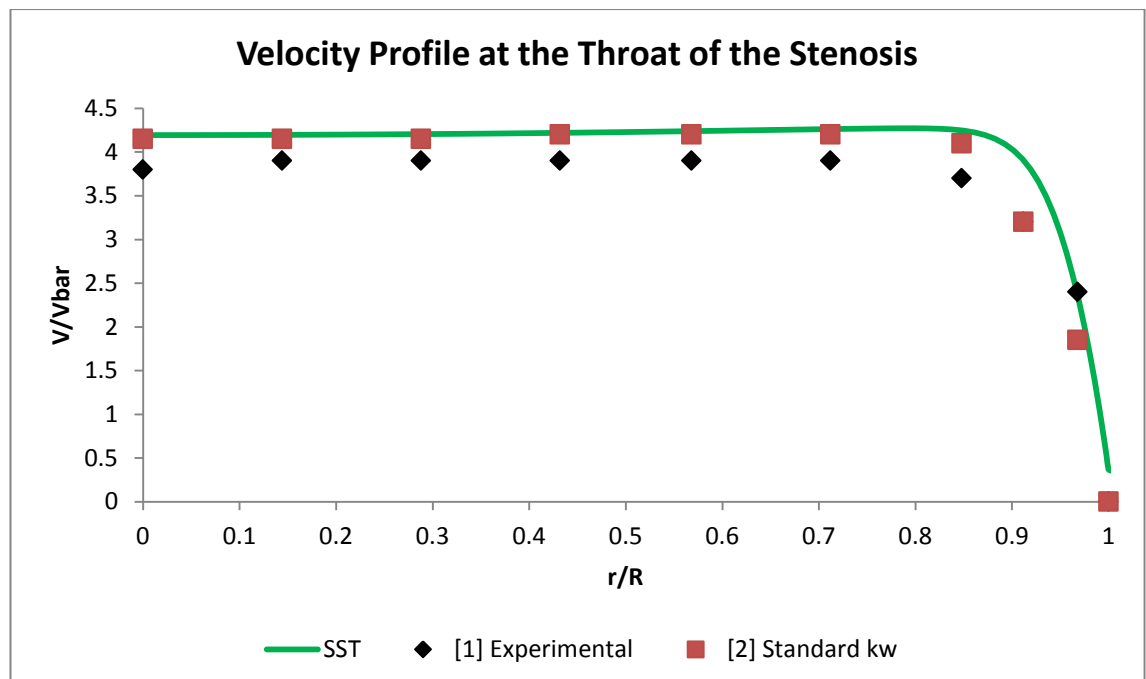


Figure 20. Comparison of the velocity profile at the throat of the stenosis between the published data and the computational results.

The results in Figure 20 show good agreement with the centreline axial velocity results published by Ryval et al, and Ahmed and Giddens. The shape and magnitude of the velocity profile also compares well with those recorded by Ryval et al, and Ahmed and Giddens. The results show that the model provides a good simulation of the flow through a stenosis and that the SST model resolves the boundary layer with sufficient accuracy to analyse stagnation in the cavity.

3.2.3 Blunt Monophasic Velocity Wave

The size of the computational model was scaled for the femoral artery and the blunt monophasic velocity wave was used to determine an appropriate time step to accurately measure the flow. Figure 21 compares the velocity profile in the throat of the stenosis for the four time steps of 0.05s, 0.025s, 0.01s, and 0.005s. Table 6 compares the reattachment length of the flow downstream of the stenosis for the four time steps

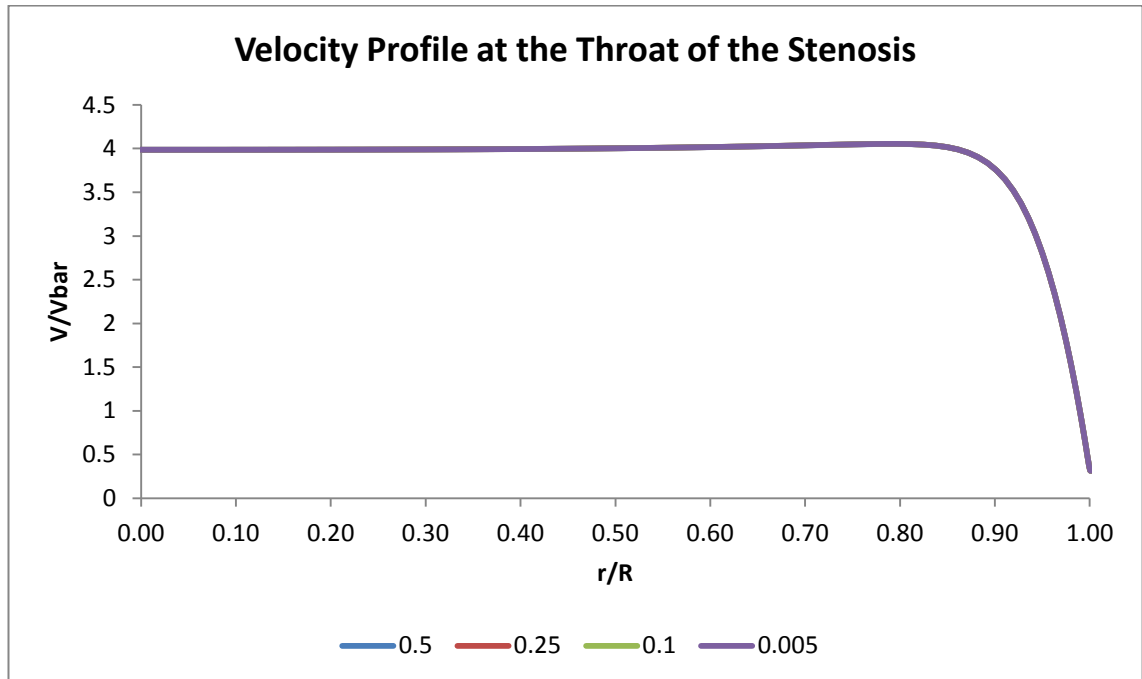


Figure 21. Comparison of the velocity profile at the throat of the stenosis for blunt monophasic velocity wave at four time steps.

The results in Table 6 show little variation in the velocity at the throat as the time step is shortened. The percentage change of 0.19% in the reattachment length from 0.01s to 0.005s suggests that these values are sufficient to ensure the flow field is accurately calculated.

Table 6. Comparison of the reattachment length downstream of the stenosis for the blunt monophasic velocity wave at four time steps.

Time Step	Reattachment Length, L/D	% Change
0.05	5.15	
0.025	5.28	2.52%
0.01	5.3	0.38%
0.005	5.31	0.19%

CHAPTER 4 - RESULTS

PHYSIOLOGICAL CONDITIONS

4.1 PHYSIOLOGICAL VELOCITY WAVES

The effect of the velocity wave on the flow conditions within the cavity of the extracorporeal access device was analysed with a number of techniques: including vector plots, SSR, and WSS. Vector plots were used to understand the flow conditions in the cavity that differentiate the four physiological velocity waves and determine regions of stagnant blood. The vector plots provide a visualisation of the flow conditions that lead to stagnation at each time step and the overall cycle. A SSR threshold of 10s^{-1} was used to determine the size and location of stagnation on the surface of the cavity at discrete time steps in the cycle. A location that experiences low shear rates for the entire cycle has a high risk of thrombus formation. The SI was used to determine the percentage of the cycle the surface of the cavity was below the SSR threshold. RT was calculated for the surface of the cavity and identifies locations that experience low and oscillating WSS. The combination of RT and SSR was used to determine the area of stagnation and risk of thrombus formation.

4.1.1 Blunt Monophasic Velocity Wave

The blunt monophasic velocity wave was the most likely to be measured in the femoral artery of patients with extensive peripheral arterial disease. The velocity wave has

continuous forward flow with slow acceleration and deceleration. Vector plots were used to describe the velocity field in the cavity at points of interest throughout the cycle. The vector plots were used to analyse the behaviour of the blood near the surface of the cavity. Regions of low velocity are depicted by dark blue vectors and a region with consistently low velocity throughout the cycle describes the location of stagnant blood. The velocity of the fluid in the cavity was analysed with particular interest in the surface and corners of the cavity.

Figure 22 shows the blunt monophasic velocity field in the cavity at time steps that correspond with the smallest regions of low velocity flow in the cavity.

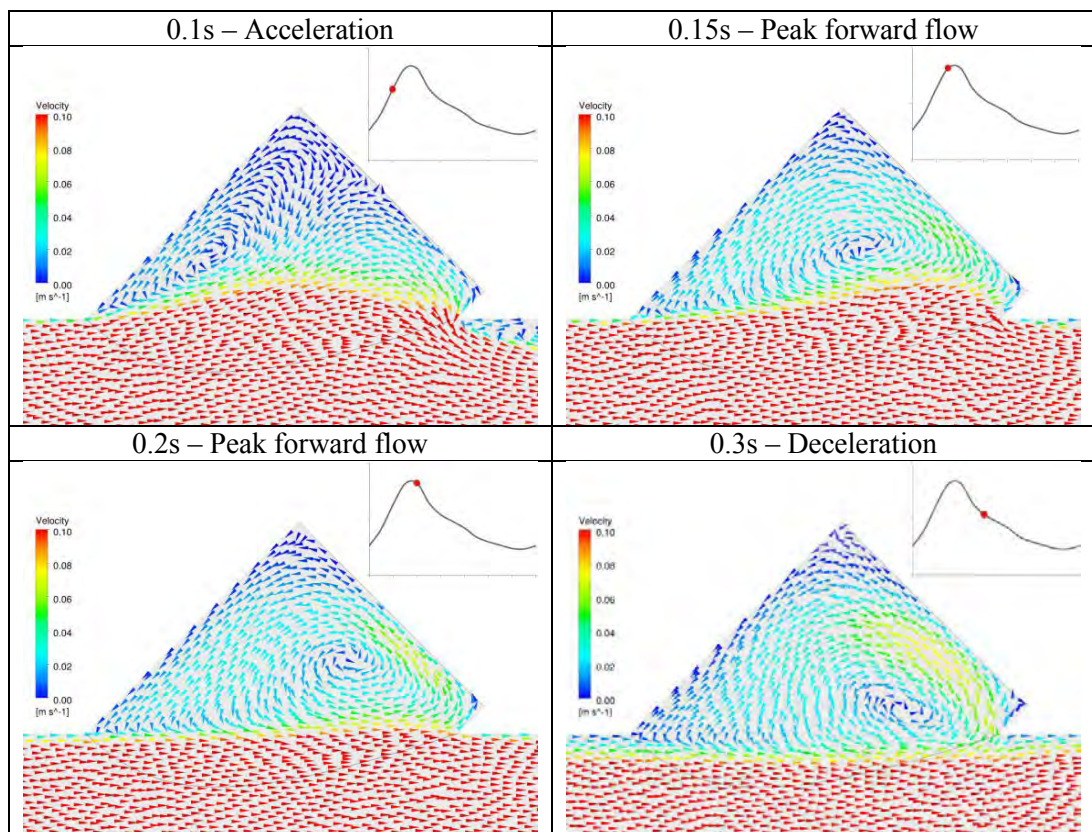


Figure 22. A cross section view of the velocity field in the cavity for the blunt monophasic velocity wave – as defined in Chapter 2.

The smallest regions of low velocity flow occur during the peak flow of the cycle, between 0.1s and 0.3s. The time steps in the tail of the wave (0.3-0.7s) exhibited low velocities throughout the cavity, which identifies stagnation. The peak flow (0.15-0.2s) creates the highest velocities in the cavity and minimises low velocity regions in the distal corner, but leaves the proximal corner essentially untouched. The peak flow (0.15s) results in the largest washout on the surface of the cavity; however, a large section of the proximal corner experiences low velocity flow throughout the cycle.

The shear strain rate was used to quantify the effect of individual aspects of the physiological velocity wave on the stagnation measured in the cavity. The corner between the surface of the stopper and the wall of the device provides the greatest opportunity for stagnation in the cavity. The surface area below the SSR threshold value was calculated at each time step of the cycle for the surface of the stopper and 1mm of the adjacent wall. Figure 23 compares the blunt monophasic velocity wave and the surface area of the cavity below the SSR threshold at each time step in the cycle. As expected from the vector plots, the low velocity time steps (0.3-0.7s) correspond to the largest areas of stagnation in the cavity and the peak flow (0.15-0.2s) creates the greatest reduction in stagnation near the stopper surface.

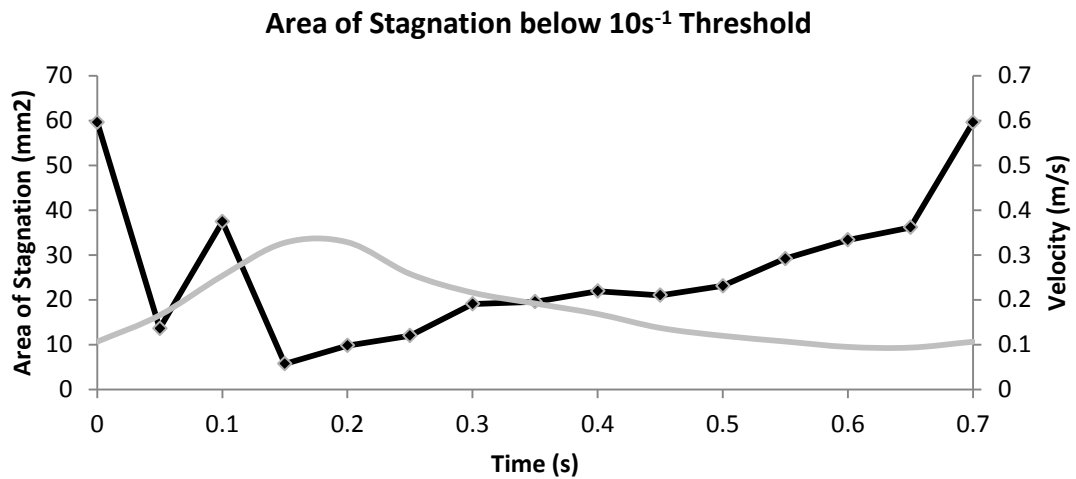


Figure 23. The area of stagnation, measured using the SSR threshold, on the surface of the cavity at each time step for the blunt monophasic velocity wave.

Figure 23 shows a trend between the velocity in the main vessel and the area of stagnation in the cavity. The Spearman ranked correlation coefficient and R^2 value was used to determine a relationship between the area of stagnation and the physiological velocity wave. A coefficient of -0.86 (0.6) suggests a significant relationship between femoral arterial velocity and area of stagnation in the cavity. The negative coefficient suggests that as the velocity increases the area of stagnation decreases.

Figure 24 and Figure 25 compare the locations below the SSR threshold for each time step and throughout the cycle. The plots are separated into phases to determine the effect of each phase on the stagnation in the cavity. Figure 24 shows the area of stagnation during the faster flow in the blunt monophasic velocity wave. The plots show good agreement with the results from the vector plots. The low velocity and low shear regions exist in the proximal corner of the device with a considerably smaller region of stagnation in the distal corner.

The blunt monophasic velocity wave has much slower acceleration and deceleration than the other velocity waves and is continuously forward flow. These conditions isolate the flow in the cavity for most of the cycle and create a vortex closer to the distal corner resulting in larger low velocity regions in the proximal corner. The peak flow at 0.15-0.2s creates the smallest regions of stagnation in the cavity, as evident in the vector plots and Figure 16.

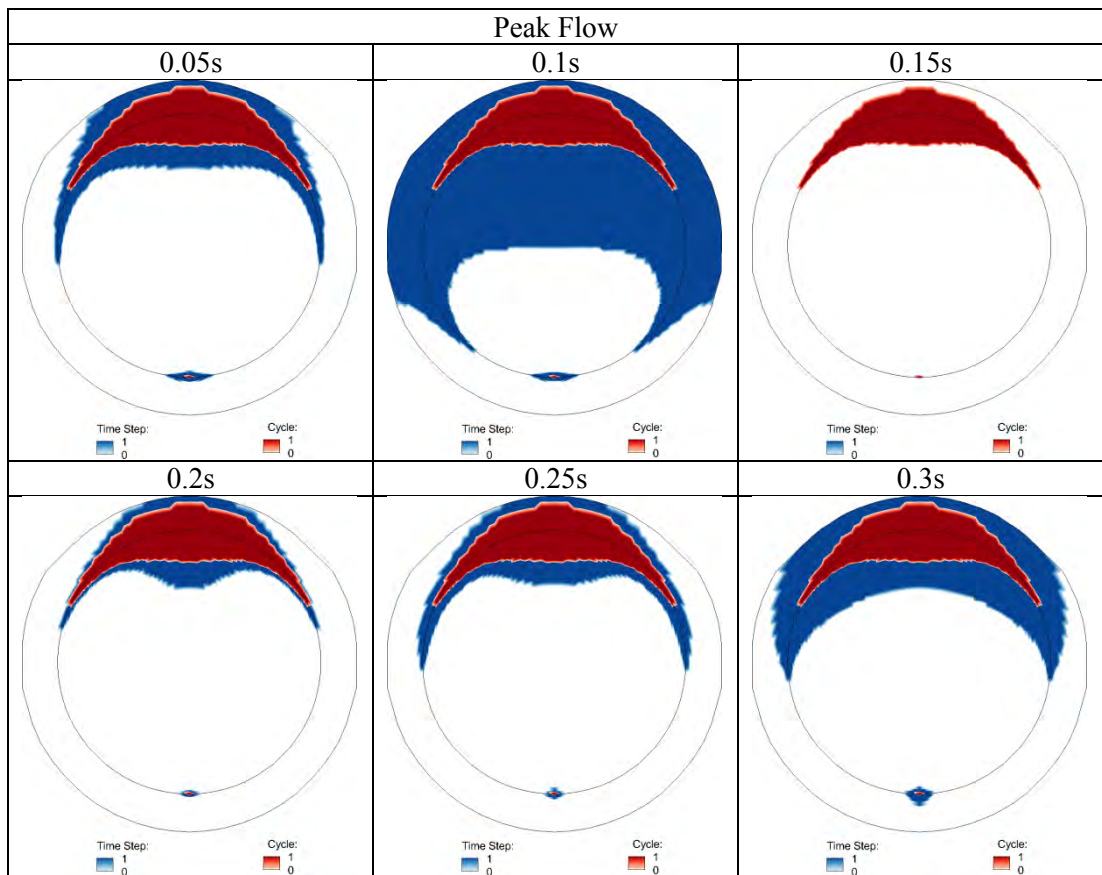


Figure 24. The location of the area of stagnation, $SSR < 10s^{-1}$, on the surface of the stopper at discrete time steps during the peak flow of the blunt monophasic velocity wave (Red) and for the entire cycle, $SI=1$ (Blue).

Figure 25 shows the area of stagnation in the cavity during the time steps at the end of the blunt monophasic cycle. The plots reveal that as the velocity decreases the area of

stagnation on the surface of the cavity increases and covers most of the surface by the end of the cycle.

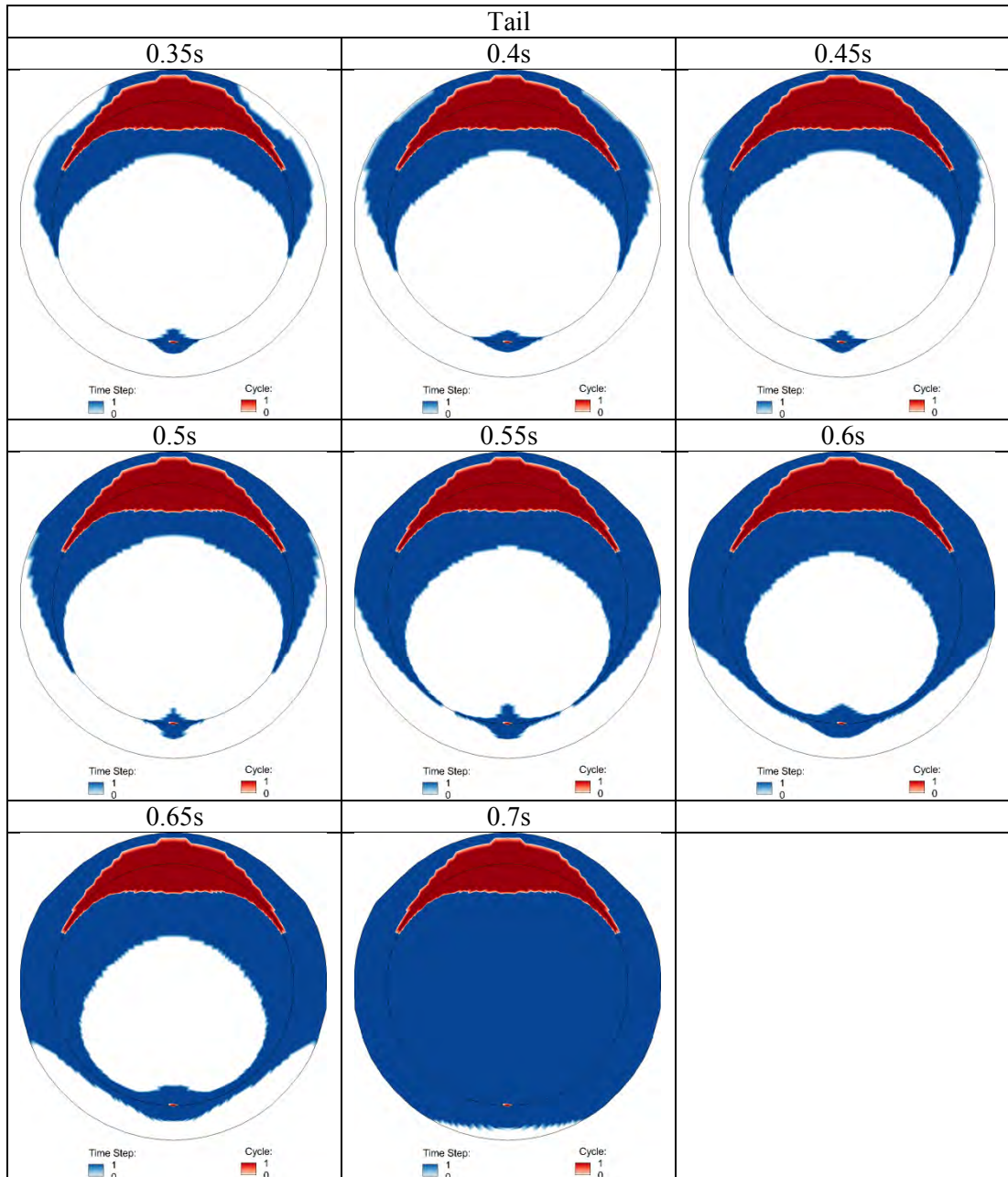


Figure 25. The location of the area of stagnation, $SSR < 10s^{-1}$, on the surface of the stopper at discrete time steps at the end of the blunt monophasic velocity wave (Red) and for the entire cycle, $SI=1$ (Blue).

The SI was used to determine the percentage of the cycle the surface of the cavity was below the threshold value. An SI of 1 (100%) indicates an area of the surface below the

SSR threshold for the entire cycle and suggests stagnation. The OSI is a measure of the cyclic departure of the WSS vector from its predominant axial alignment. A high OSI indicates a location on the surface where the fluid remains for the duration of the cycle. The SI and the OSI are shown below in Figure 26. The area of stagnation for the cycle calculated from the SI is 5.74mm².

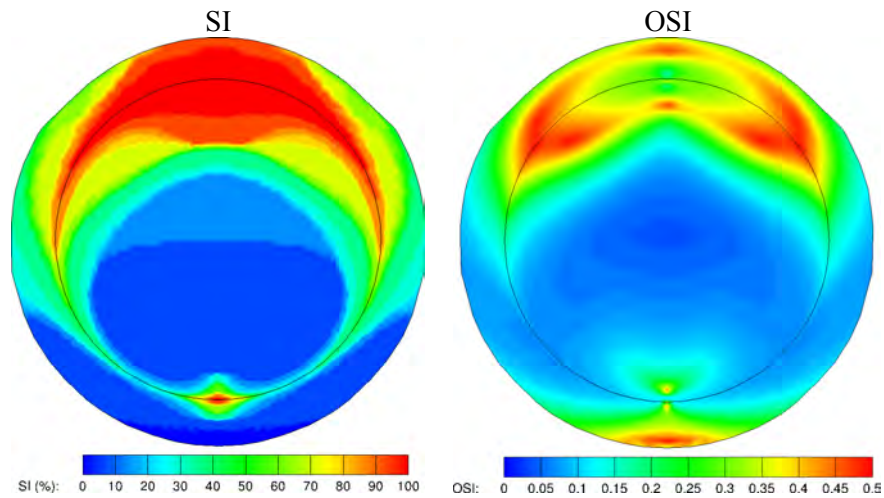
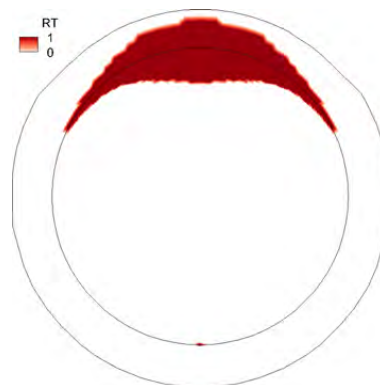


Figure 26. The SI and OSI on the surface of the cavity for the blunt monophasic velocity wave.

The SI shows the area of stagnation is predominantly on the proximal corner of the cavity. The OSI also shows high values around the proximal corner, but only moderate values in the deepest part of the proximal corner. The SI and OSI alone are not the best markers for stagnation; the low shear flow in the SI may be unidirectional and not stagnant (sides of the stopper surface), high OSI values may be subject to high shear rates (as shown near the distal corner), and low OSI values may unidirectional low shear stagnation (proximal corner).

RT combines the oscillatory nature of flow in the OSI with the low shear values of the average WSS to determine regions of stagnation on the surface of the cavity. The RT in combination with the SI is able to determine flow that remains in a fixed location and is

exposed to low shear rates for the duration of the cycle. The area of stagnation, calculated from the RT ($RT > 1$) is shown in Figure 27. The area of stagnation is located primarily on the proximal corner, as expected from the vector plots, SSR, and SI. The area covers a substantial area, 5.74mm², of the stopper surface and wall of the cavity near the proximal corner.



Area of Stagnation – 5.74mm²

Figure 27. The location of the area of stagnation calculated from the RT ($RT > 1$) and the SSR threshold for the blunt monophasic velocity wave.

4.1.2 Sharp Monophasic Velocity Wave

The sharp monophasic is the second wave that is most likely to be measured in the femoral artery of patients with extensive peripheral arterial disease. The sharp monophasic wave has a sharp peak at the start of the wave and then tapers towards zero flow at the end of the cycle. Figure 28 shows the sharp monophasic velocity field in the cavity at time steps that correspond with the smallest regions of low velocity flow in the cavity. The smallest regions of low velocity flow occur during the peak flow of the cycle, between 0.05s and 0.2s. The low velocity time steps (0.3-0.7s) result in low velocities throughout the cavity. The peak flow (0.05-0.1s) creates the highest velocities

in the cavity and minimises the low velocity regions in the distal corner. The peak flow at 0.1s also results in the largest washout in the proximal corner, and the entire cavity.

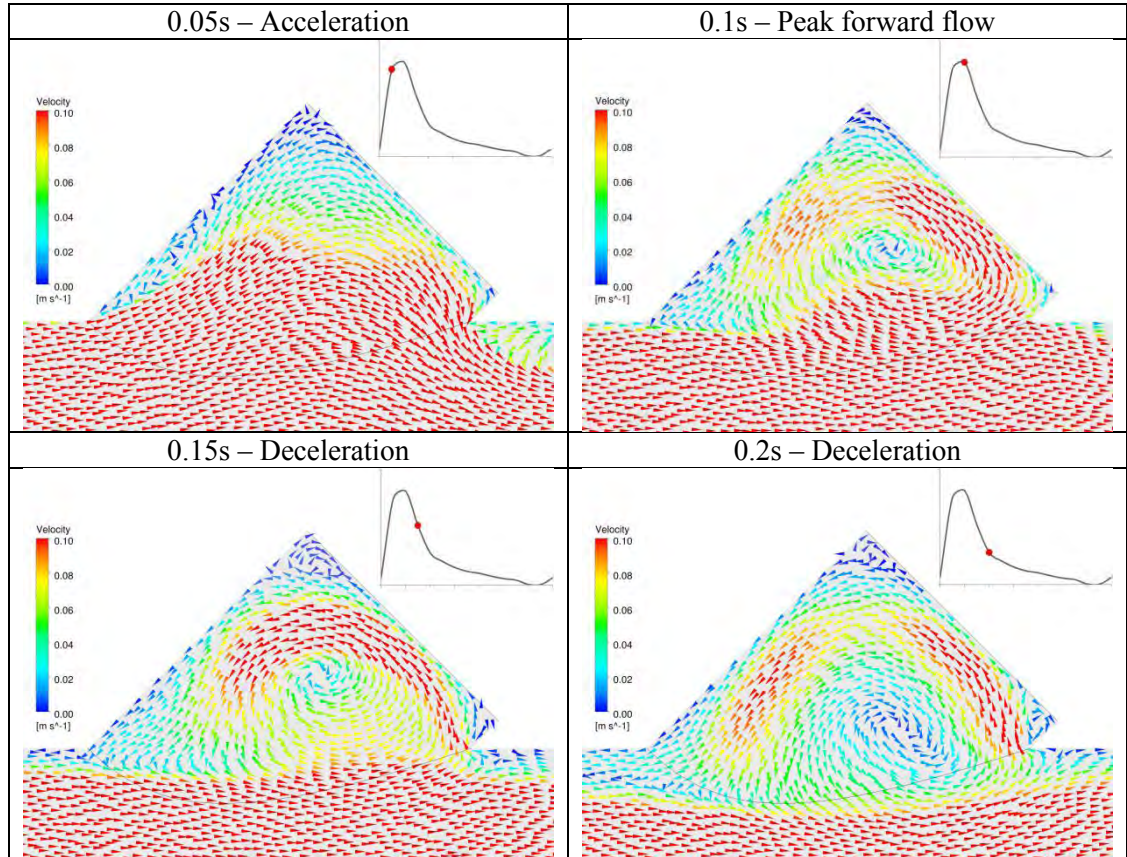


Figure 28. The velocity field in the cavity for the sharp monophasic velocity wave – as defined in Chapter 2.

Figure 29 compares the sharp monophasic velocity wave and the surface area of the cavity below the SSR threshold at each time step in the cycle. As expected the low velocity time steps (0.3-0.7s) correspond to the largest areas of stagnation in the cavity. The graph confirms that the flow conditions at peak flow (0.1s) constitute the greatest impact on stagnation in the cavity. Similar to the blunt monophasic velocity wave Figure 29 indicates a trend between the velocity wave and the area of stagnation in the cavity. The Spearman ranked correlation coefficient for the sharp monophasic velocity

wave was -0.89 (0.6), which suggests that as the femoral arterial velocity increases the area of stagnation in the cavity decreases.

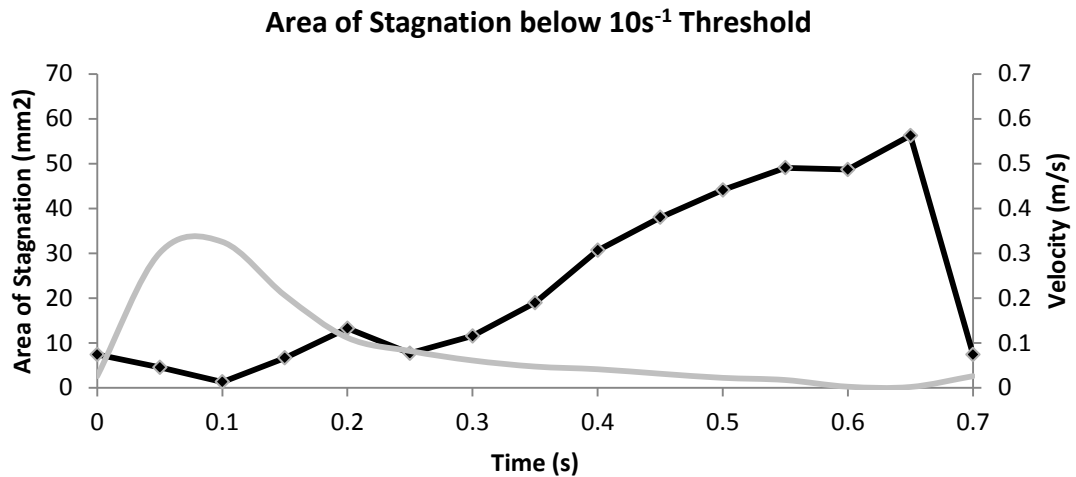


Figure 29. The area of stagnation, measured using the SSR threshold, on the surface of the cavity at each time step for the sharp monophasic velocity wave.

Figure 30 and Figure 31 compares the locations in the cavity below the SSR threshold for each time step and throughout the cycle. The plots are separated into phases to determine the effect of each phase on the stagnation in the cavity. Figure 30 shows the area of stagnation during the faster flow in the sharp monophasic velocity wave. The plots show good agreement with the results from the vector plots. The low velocity and low shear regions exist in the proximal corner of the device with a very small region of stagnation in the distal corner. The fast acceleration and peak flow at the start of the wave reduce the stagnation in the cavity to primarily the proximal corner. The peak flow at 0.1s creates the smallest area of stagnation in the cavity, as evident in Figure 28 and Figure 30.

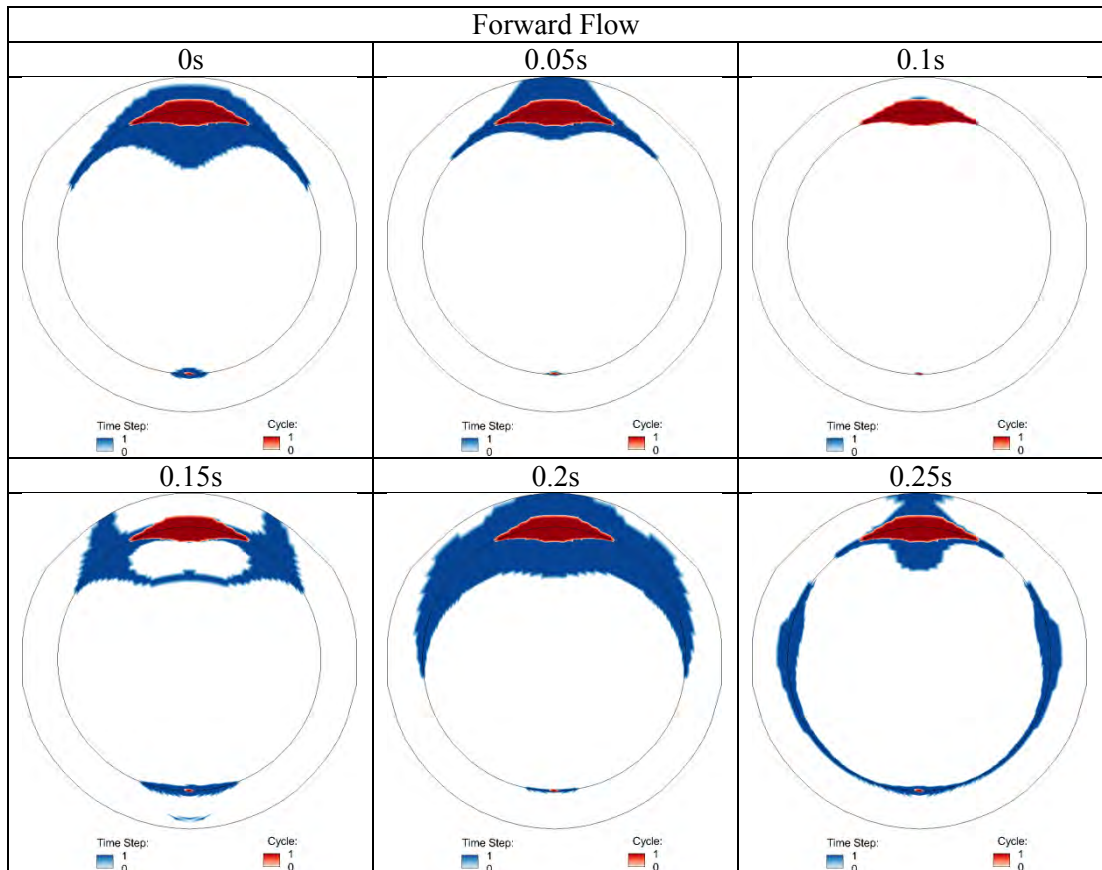


Figure 30. The location of the area of stagnation, $SSR < 10s^{-1}$, on the surface of the stopper at discrete time steps during the fastest flow of the sharp monophasic velocity wave (Red) and for the entire cycle, $SI=1$ (Blue).

Figure 31 shows the area of stagnation on the surface of the cavity during the time steps at the end of the sharp monophasic cycle. As the velocity decreases the area of stagnation expands along the entire corner of the cavity, before covering the wall of the cavity and eventually the stopper surface.

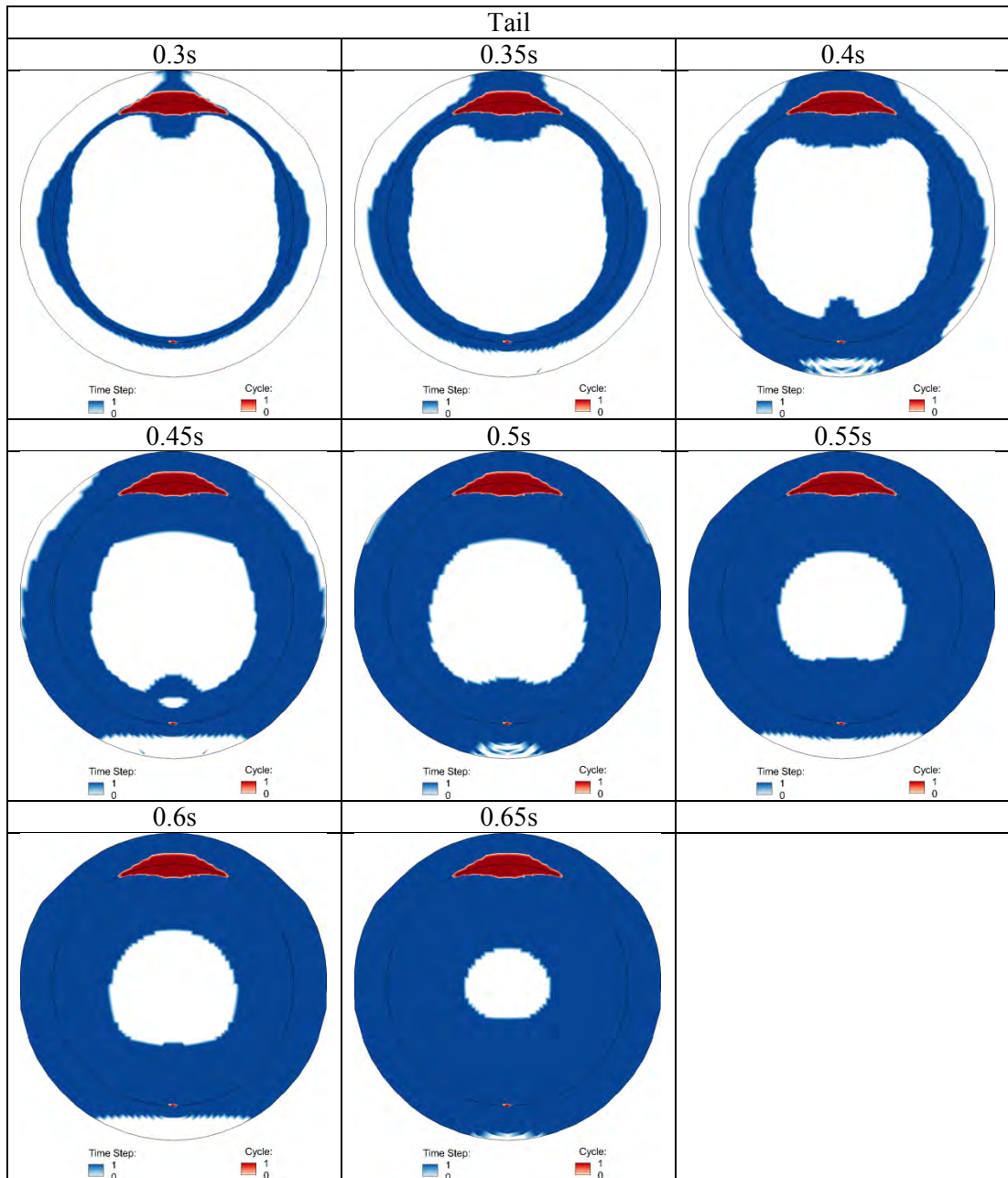


Figure 31. The location of the area of stagnation, $SSR < 10s^{-1}$, on the surface of the stopper at discrete time steps at the end of the sharp monophasic velocity wave (Red) and for the entire cycle, $SI=1$ (Blue).

Figure 32 shows the SI and the OSI on the surface of the cavity; the area of stagnation for the cycle is $1.29mm^2$.

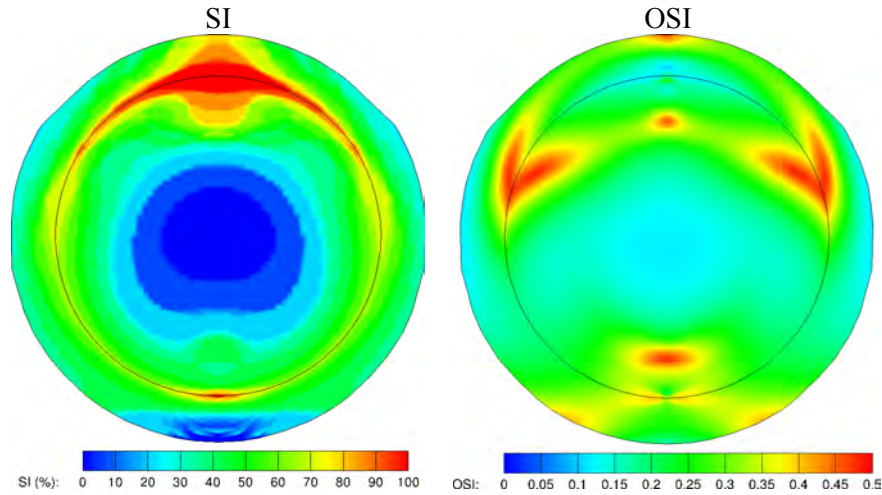
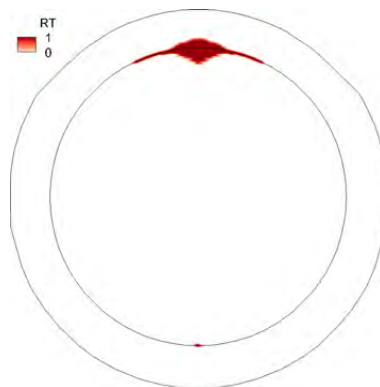


Figure 32. The SI and OSI on the surface of the cavity for the sharp monophasic velocity wave.

The area of stagnation is predominantly on the proximal corner of the cavity, as was the case with the blunt monophasic case. The OSI on the other hand shows low oscillatory behaviour in the proximal corner and high oscillations in regions of moderate SI. The low OSI in regions of high SI suggests that the flow has the potential to wash out of the corner and not stagnate.

The area of stagnation, calculated from the RT is shown in Figure 33. The area of stagnation is located primarily on the proximal corner, but is considerably smaller, 0.61mm², than the blunt monophasic case.



Area of Stagnation – 0.61mm²

Figure 33. The location of the area of stagnation calculated from the RT (RT>1) and the SSR threshold for the sharp monophasic velocity wave.

4.1.3 Biphasic Velocity Wave

Figure 34 shows the biphasic velocity field in the cavity at time steps that correspond with the smallest regions of low velocity flow in the cavity.

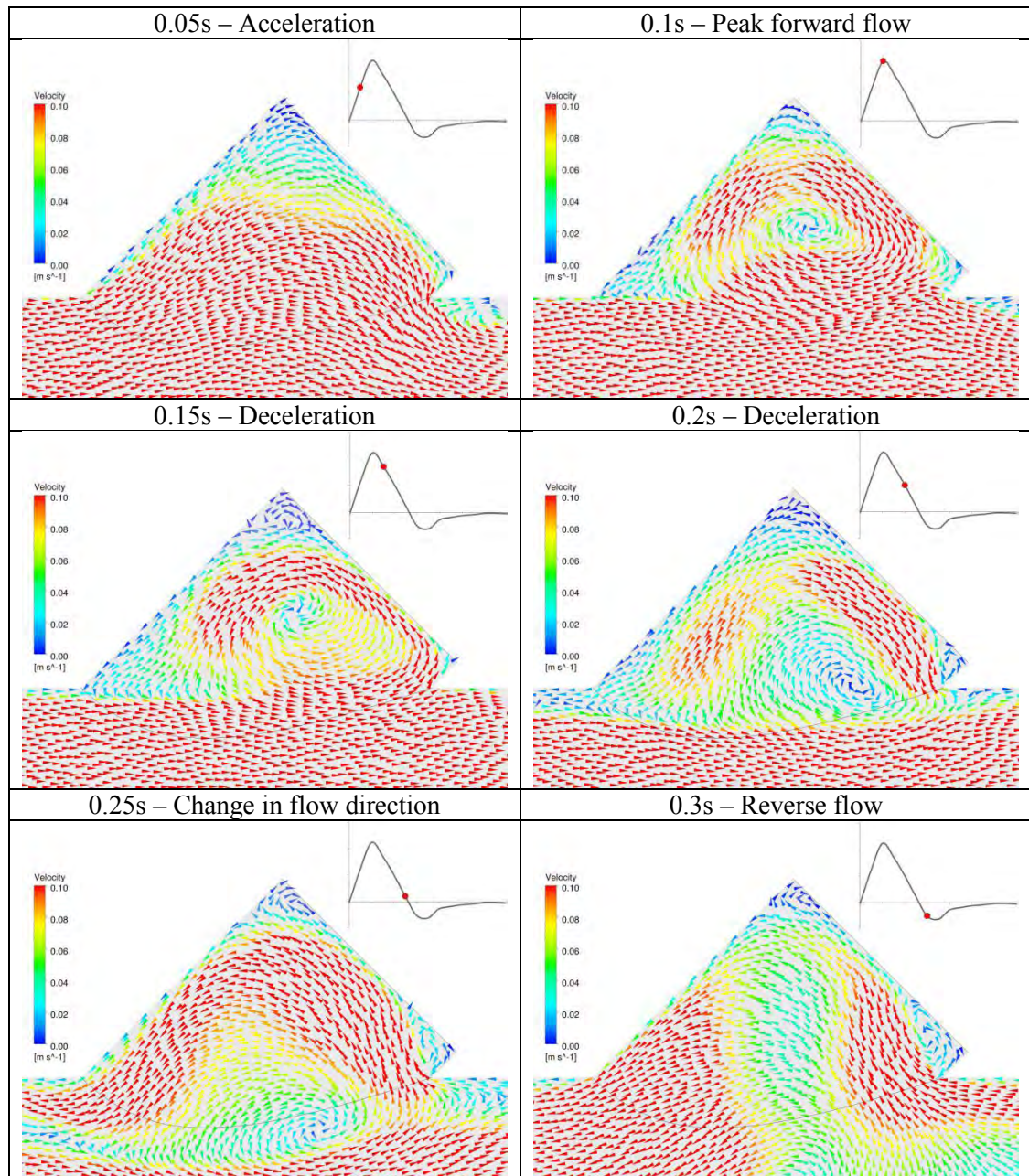


Figure 34. The velocity field in the cavity for the biphasic velocity wave - as defined in Chapter 2.

The vector plots reveal that the flow conditions between peak flow (0.1s) and reverse flow (0.3s) cause the greatest disturbances to the blood within the cavity. The low

velocity time steps (0.4-0.7s) result in low velocities throughout the cavity. The faster flow at the start of the cycle (0.05, 0.1 and 0.15s) generates high velocity flow in the distal corner of the cavity, but leaves a small region of low velocity flow in the proximal corner. The decelerating flow and reverse flow (0.2, 0.25, and 0.3s) moves the high velocity regions away from the distal corner and closer to the proximal corner. The peak flow (0.1s) results in the largest washout in the distal end of the cavity and the change in flow direction at 0.25s results in the greatest reduction in stagnation in the proximal corner of the cavity. Figure 35 compares the biphasic velocity wave and the surface area of the cavity below the SSR threshold at each time step in the cycle.

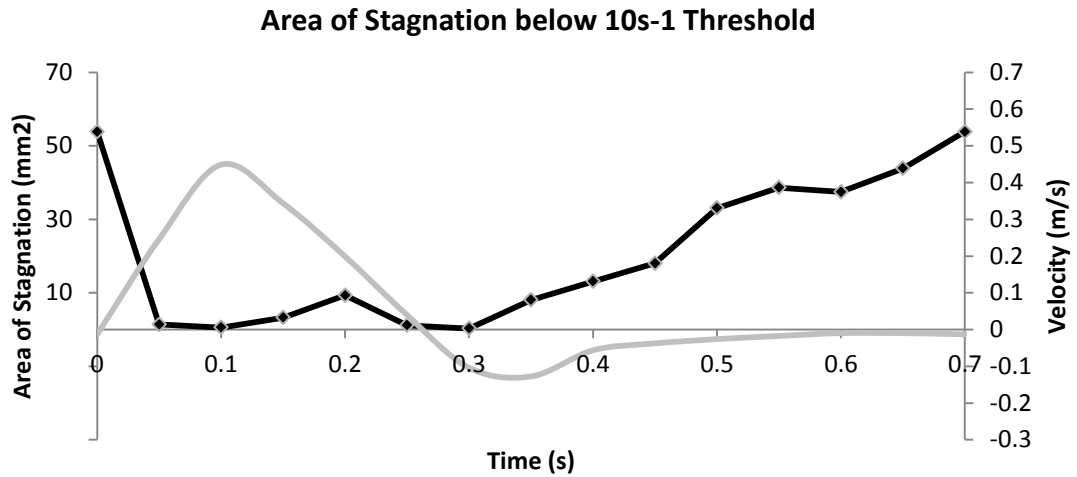


Figure 35. The area of stagnation, measured using the SSR threshold, on the surface of the cavity at each time step for the biphasic velocity wave.

As expected the low velocity time steps (0.4-0.7s) correspond to the largest areas of stagnation in the cavity. Figure 35 confirms that the flow conditions between peak flow (0.1s) and reverse flow (0.3s) constitute the greatest impact on stagnation in the cavity, with the smallest area of stagnation occurring at peak flow (0.1s) and flow reversal (0.3s). The Spearman ranked correlation coefficient for the biphasic velocity wave was -

0.82 (0.6), which suggests that as the femoral arterial velocity increases the area of stagnation in the cavity decreases.

Figure 36, Figure 37, Figure 38, and Figure 39 compares the locations below the SSR threshold for each time step and throughout the cycle. Figure 36 shows the area of stagnation during the forward flow in the cycle. The plots show good agreement with the results from the vector plots. The acceleration, peak flow, and deceleration all reduce the area of stagnation on the distal corner, but are incapable of washing out the proximal corner. The peak flow creates the smallest area of stagnation in the forward phase.

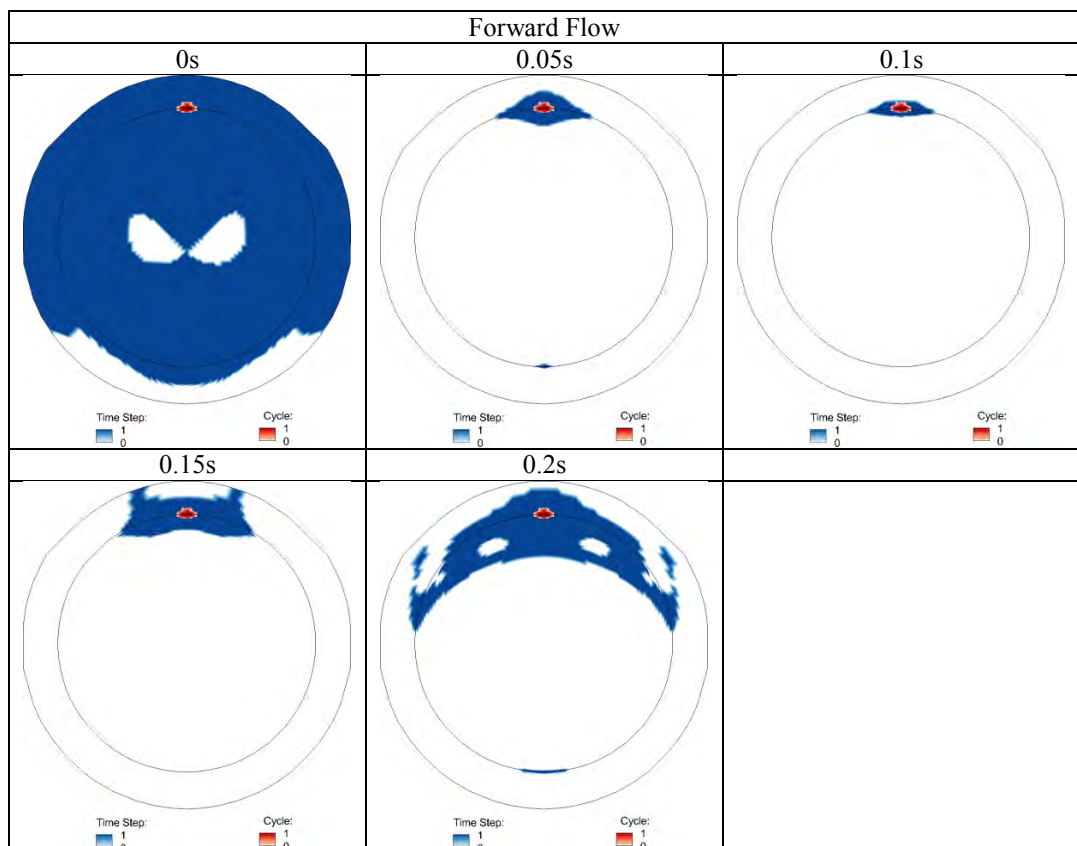


Figure 36. The location of the area of stagnation, $SSR < 10s^{-1}$, on the surface of the stopper at discrete time steps during the forward flow of the biphasic velocity wave (Red) and for the entire cycle, $SI=1$ (Blue).

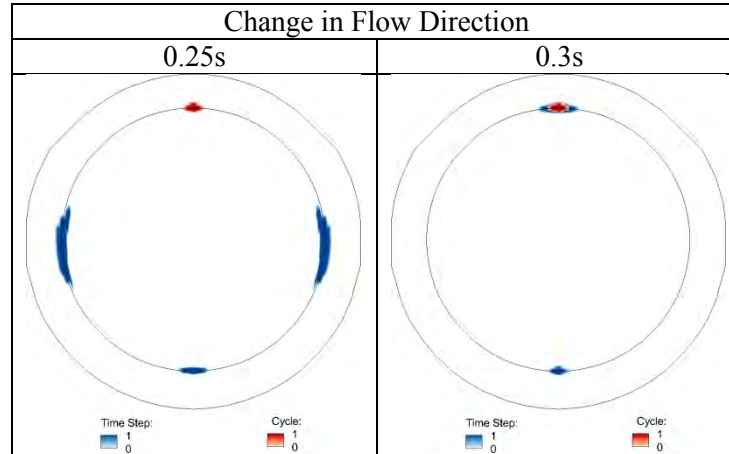


Figure 37. The location of the area of stagnation, $SSR < 10s^{-1}$, on the surface of the stopper at discrete time steps during the change in direction of flow of the biphasic velocity wave (Red) and for the entire cycle, $SI=1$ (Blue).

Figure 37 shows the area of stagnation during the change in flow direction in the biphasic wave. The flow at 0.3s creates the smallest area of stagnation throughout the entire cycle; however it is the flow at 0.25s that minimises the area of stagnation in the proximal corner.

Figure 38 and Figure 39 show the area of stagnation in the cavity during the reverse flow and at the end of the biphasic cycle, respectively. The reverse flow, Figure 38, is successful at flushing out the sides of the cavity, but fails to flush out the fluid in either of the corners. The flow at the end of the cycle expands the area of stagnation along the corner of the cavity before encompassing the wall and surface of the stopper.

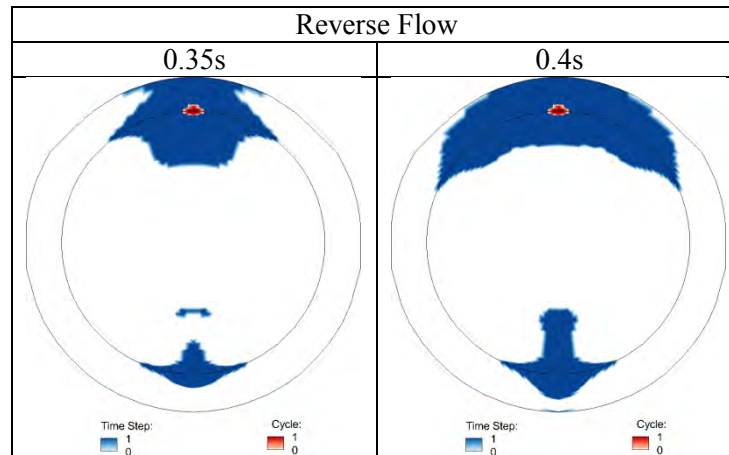


Figure 38. The location of the area of stagnation, $SSR < 10s^{-1}$, on the surface of the stopper at discrete time steps during the reverse flow of the biphasic velocity wave (Red) and for the entire cycle, $SI=1$ (Blue).

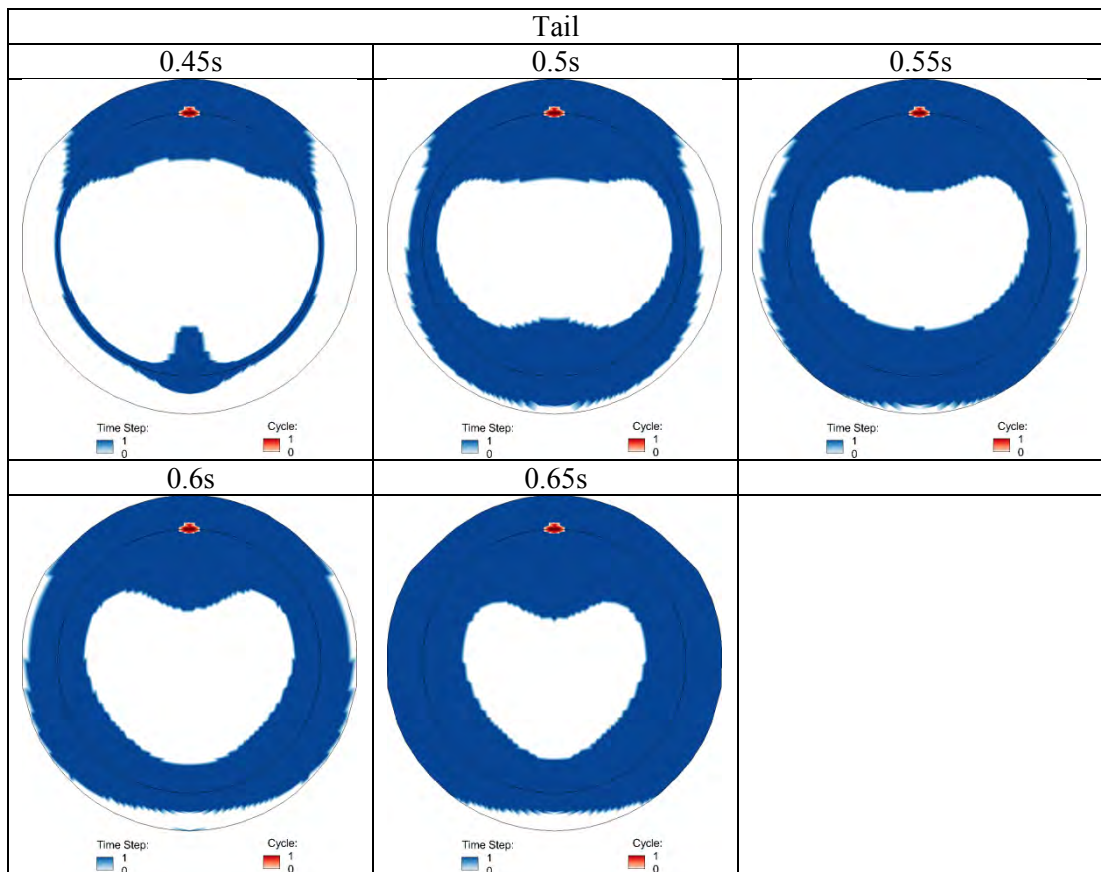


Figure 39. The location of the area of stagnation, $SSR < 10s^{-1}$, on the surface of the stopper at discrete time steps during the flow at the end of the biphasic velocity wave (Red) and for the entire cycle, $SI=1$ (Blue).

Figure 40 shows the SI and the OSI on the surface of the cavity; the area of stagnation for the cycle is $0.07mm^2$.

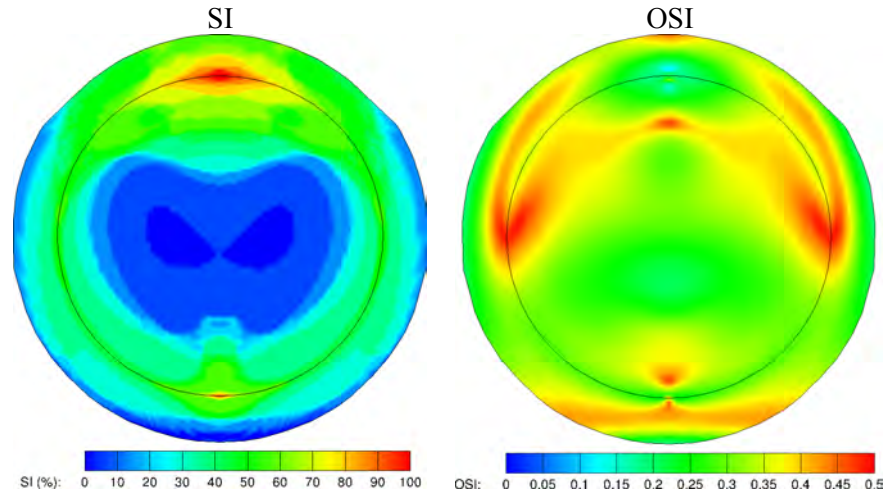
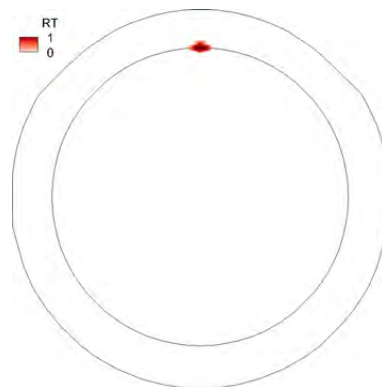


Figure 40. The SI and OSI on the surface of the cavity for the biphasic velocity wave.

The area of stagnation is located entirely in the proximal corner of the cavity and the small area of stagnation in the distal corner was removed. Similar to the sharp monophasic case the OSI shows low oscillatory behaviour in the proximal corner and high oscillations in regions of moderate SI. The low OSI in regions of high SI suggests that the flow has the potential to wash out of the corner and not stagnate.

The area of stagnation, calculated from the RT is shown in Figure 41. The area of stagnation is located primarily on the proximal corner and is smaller, 0.07mm², than both of the monophasic cases.



Area of Stagnation - 0.07mm²

Figure 41. The location of the area of stagnation determined from the RT (RT>1) and the SSR threshold for the biphasic velocity wave.

4.1.4 Triphasic Velocity Wave

Figure 42 shows the triphasic velocity field in the cavity at time steps that correspond with the smallest regions of low velocity flow in the cavity.

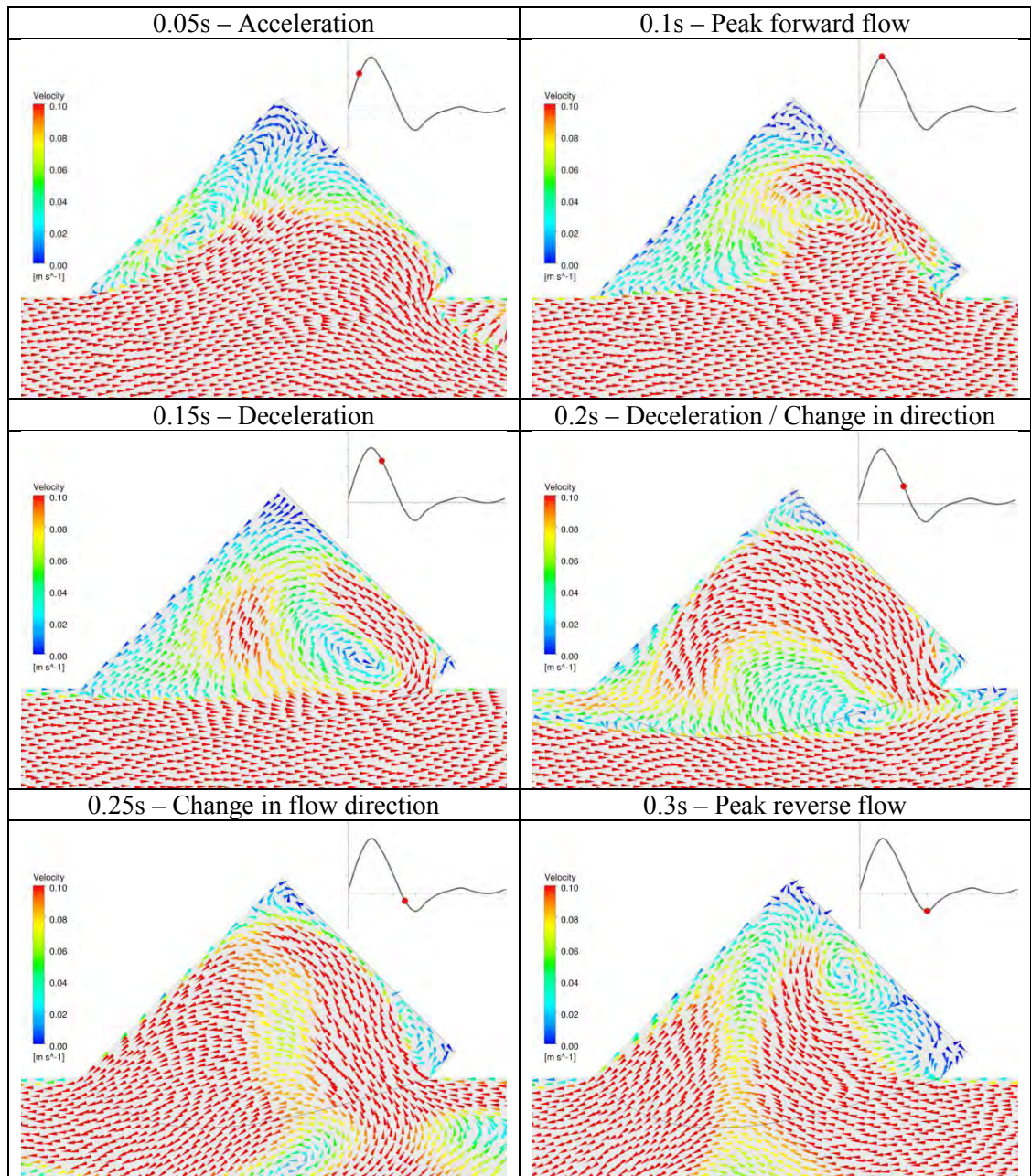


Figure 42. The velocity field in the cavity during the forward flow in triphasic velocity wave – as defined in Chapter 2.

The vector plots reveal that the flow conditions between peak flow (0.1s) and reverse flow (0.3s) cause the greatest disturbances to the blood within the cavity. The low velocity time steps (0.4-0.7s) result in low velocities throughout the cavity. The faster flow at the start of the cycle (0.05, 0.1 and 0.15s) generates high velocity flow in the distal corner of the cavity, but leaves a small region of low velocity flow in the proximal corner. The decelerating flow and reverse flow (0.2, 0.25, and 0.3s) moves the high velocity regions away from the distal corner and closer to the proximal corner. The peak flow (0.1s) results in the largest washout in the distal end of the cavity and the change in flow direction at 0.25s results in the greatest reduction in stagnation in the proximal corner of the cavity.

The area of stagnation for the velocity wave was calculated for the surface area below the threshold for the entire cycle. Figure 43 compares the triphasic velocity wave and the surface area of the cavity below the SSR threshold at each time step in the cycle.

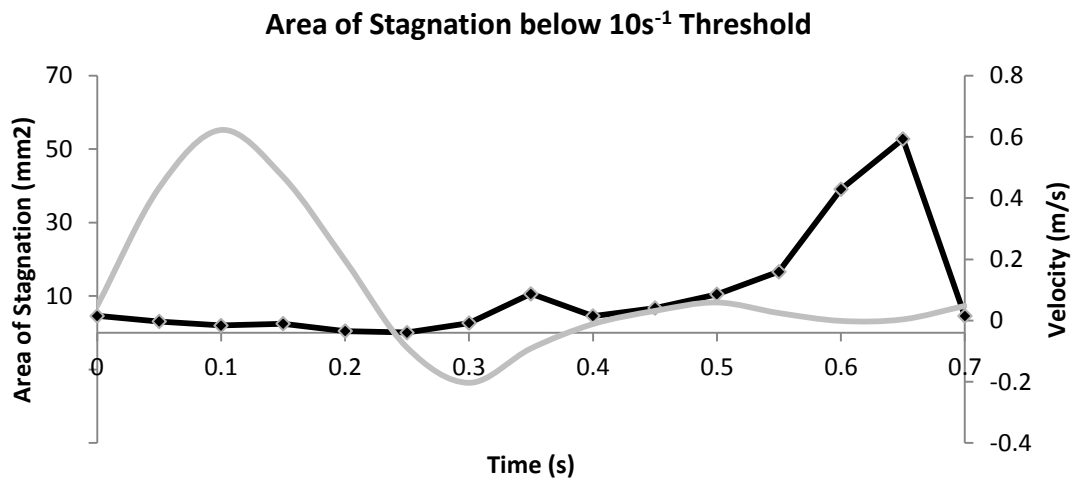


Figure 43. The area of stagnation, measured using the SSR threshold, on the surface of the cavity at each time step for the triphasic velocity wave.

As expected the low velocity time steps (0.35-0.7s) correspond to the largest areas of stagnation in the cavity. The graph also confirms that the flow conditions between peak flow (0.1s) and peak reverse flow (0.3s) constitute the greatest impact on stagnation in the cavity, with the smallest area of stagnation occurring as the flow changes directions (0.25s). The Spearman ranked correlation coefficient for the sharp monophasic velocity wave was -0.75 (0.6), which suggests that as the femoral arterial velocity increases the area of stagnation in the cavity decreases.

The location of stagnation at each time step of the cycle is shown in Figure 44, Figure 45, Figure 46, and Figure 47. The plots compare the locations below the SSR threshold for each time step and throughout the cycle. The plots are separated into phases to determine the effect of each phase on the stagnation in the cavity. Figure 44 shows the area of stagnation during the forward flow phase of the triphasic velocity wave. The plots show agreement with the results from the vector plots. The low velocity and low shear regions exist in the proximal corner of the device with stagnation in the distal corner removed at 0.15s.

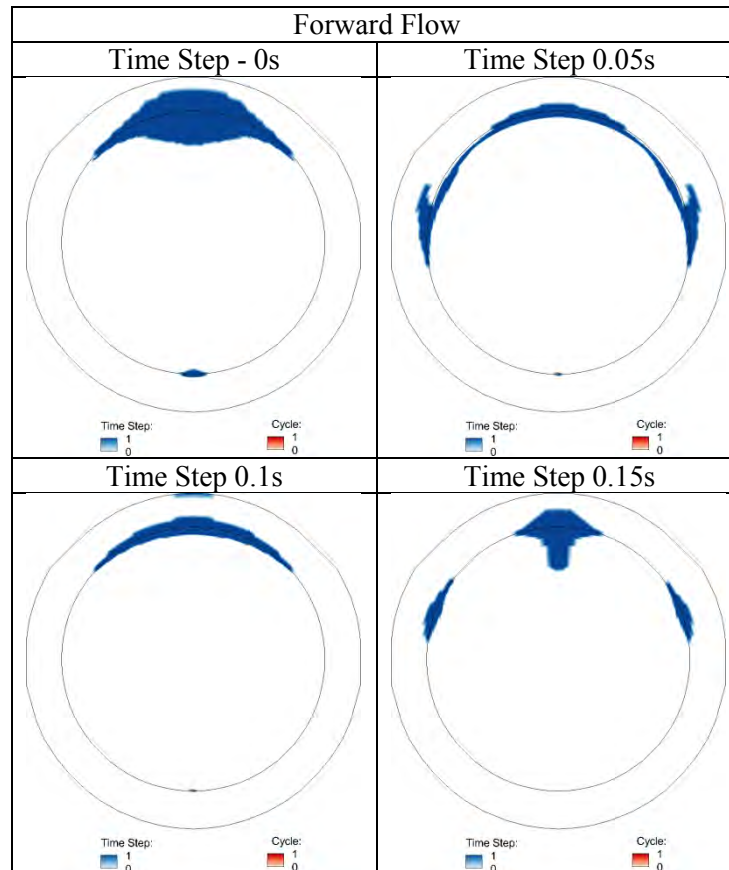


Figure 44. The location of the area of stagnation, $SSR < 10s^{-1}$, on the surface of the stopper at discrete time steps during the forward flow of the triphasic velocity wave (Red) and for the entire cycle, SI=1 (Blue).

Figure 45 shows the area of stagnation during the change between forward and reverse flow of the triphasic velocity wave. The change in flow occurs from 0.2-0.35s with the flow reversal occurring at the walls at 0.2s and penetrating the flow in the cavity before the core flow reverses at 0.25s. The flow reversal at the walls at 0.2s disturbs the flow in the cavity causing reduced areas of stagnation in both corners. The core flow reversal at 0.25s causes stronger flow within the whole cavity and the smallest area of stagnation in the cavity for the entire cycle.

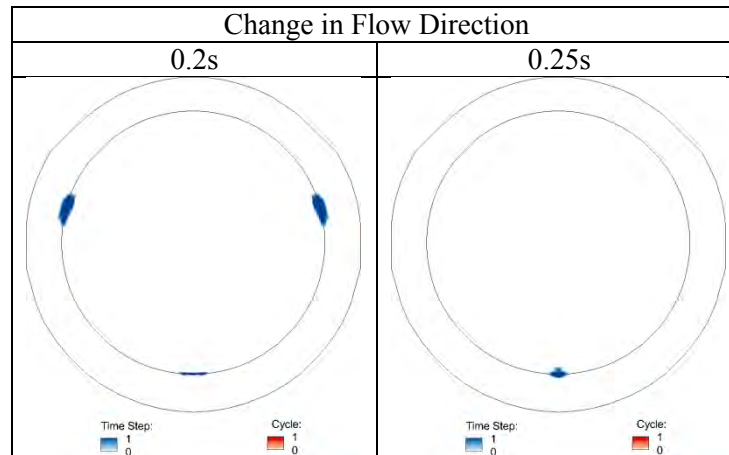


Figure 45. The location of the area of stagnation, $SSR < 10s^{-1}$, on the surface of the stopper at discrete time steps during the change in flow direction flow of the triphasic velocity wave (Red) and for the entire cycle, $SI=1$ (Blue).

Figure 46 shows the area of stagnation during the reverse flow phase of the triphasic velocity wave. The reverse flow (0.3-0.35s) is successful at creating flow with high shear rates in the lateral section of the surface but leaves considerable areas of stagnation in both of the corners.

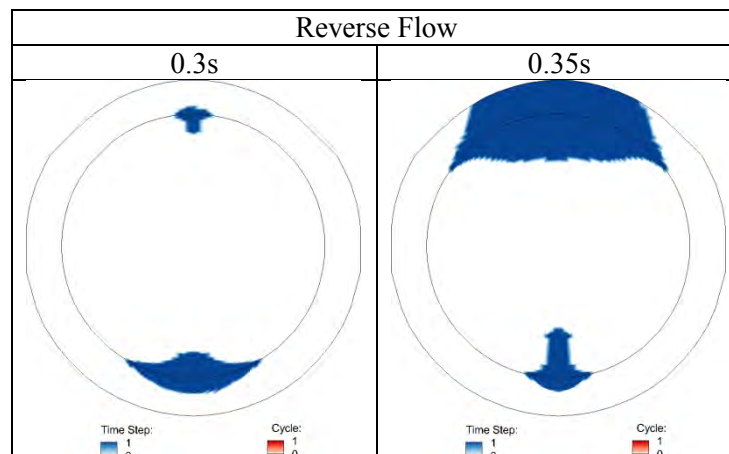


Figure 46. The location of the area of stagnation, $SSR < 10s^{-1}$, on the surface of the stopper at discrete time steps during the reverse flow of the triphasic velocity wave (Red) and for the entire cycle, $SI=1$ (Blue).

As evident in the vector plots the time steps from 0.4-0.7s create low velocity and low shear regions near the surface of the stopper. The plots in Figure 47 show a consistent

area of stagnation in the corner where the stopper and wall meet and along most of the surface in the time steps at the end of the cycle

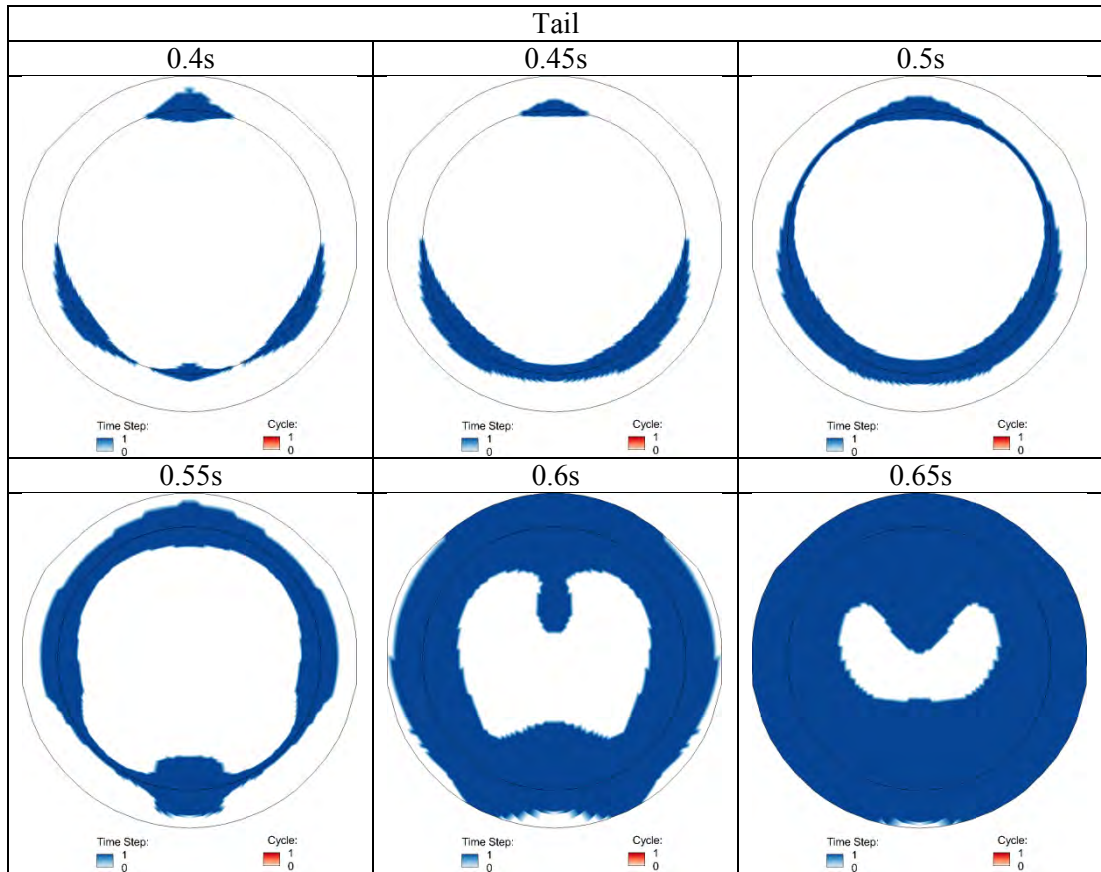


Figure 47. The location of the area of stagnation, $SSR < 10s^{-1}$, on the surface of the stopper at discrete time steps during the flow at the end of the triphasic velocity wave (Red) and for the entire cycle, $SI=1$ (Blue).

Figure 48 shows the SI and the OSI on the surface of the cavity; the area of stagnation for the cycle is $0mm^2$. The high SI is located in regions of moderate OSI an high OSI in regions of moderate SI

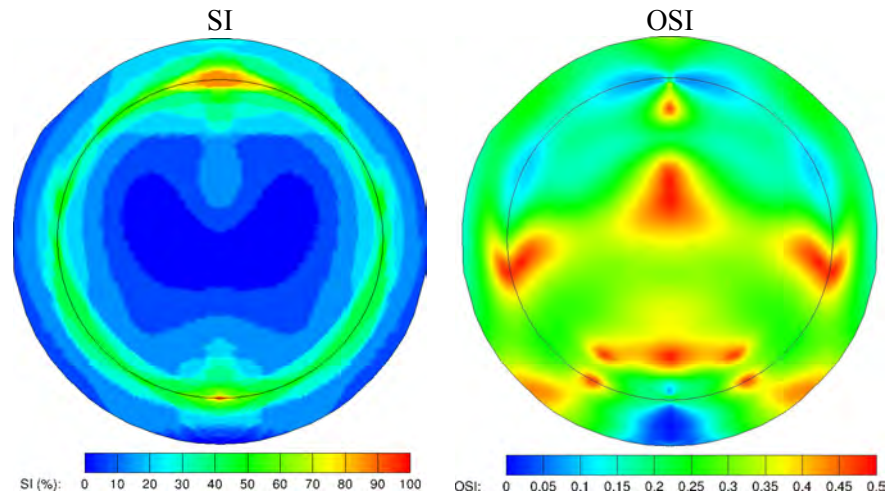
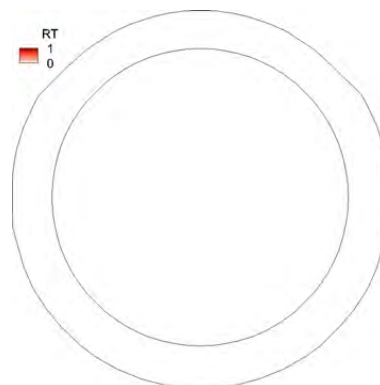


Figure 48. The SI on the surface of the cavity for the triphasic velocity wave.

The RT identifies no area of stagnation on the stopper surface for the triphasic velocity wave, as shown in Figure 49.



Area of Stagnation - 0mm²

Figure 49. The location of the area of stagnation determined from the RT ($RT > 1$) and the SSR threshold for the triphasic velocity wave.

The four RT plots provide an indication of fluid that remains trapped in the same location for at least one cardiac cycle, but not the magnitude of the RT. The distribution of the RT magnitude is shown in Figure 50. The distribution shows the magnitude of the RT experienced in each of the four velocity waves.

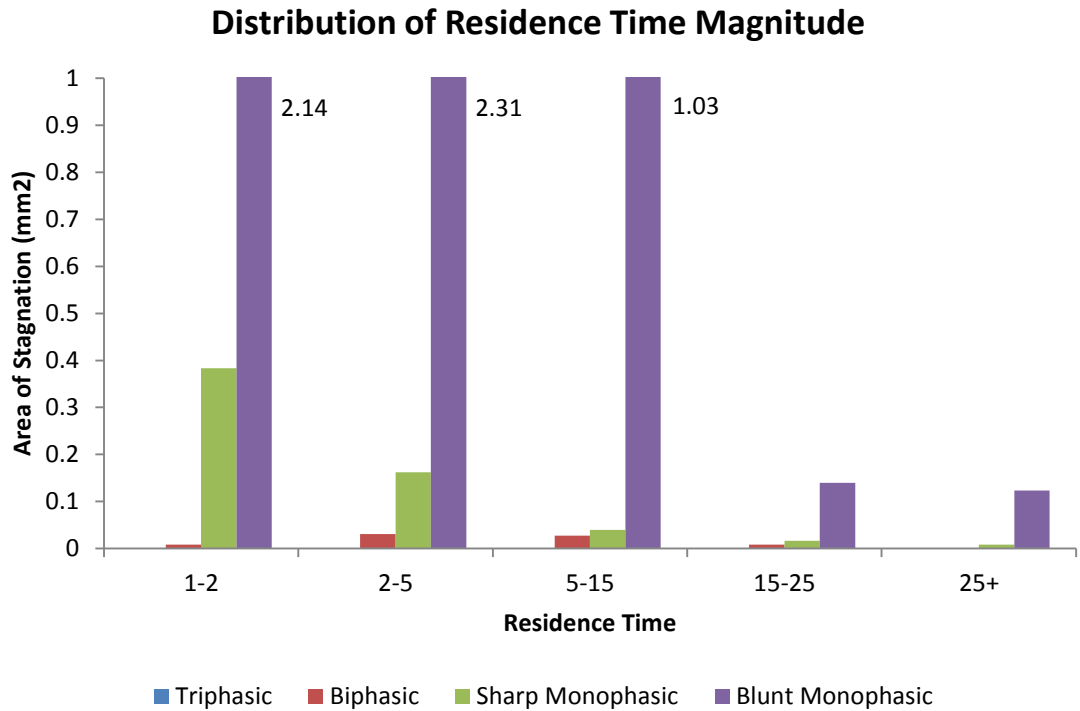


Figure 50. The distribution of the RT magnitude for the four physiological velocity waves.

Figure 50 shows an increase in the area of stagnation between the velocity waves for each magnitude range. The area decreases in all of the waves as the magnitude of the RT increases. The monophasic cases are the only waves with a RT greater than 25, which confirms the increased likelihood for these two cases to exhibit thrombus formation.

4.2 VESSEL SIZE

The vessel size is the second physiological condition that may affect the success of the device. It has been shown that males and females express similar flow rates in the femoral artery despite the significant difference in the diameter of the vessel. The smaller vessel exhibits higher velocities and a larger relative opening into the cavity for the flow to penetrate. The explanted devices were implanted into both males and females and as such the outcome of the device may depend on the size of the femoral

artery. The flow conditions were initially analysed in the femoral artery with a diameter of 10mm and were then analysed with a diameter of 8mm.

4.2.1 Blunt Monophasic Velocity Wave

Figure 51 compares the area of stagnation, calculated from the SSR, at each time step for the 8mm and 10mm vessel diameters with the blunt monophasic velocity wave.

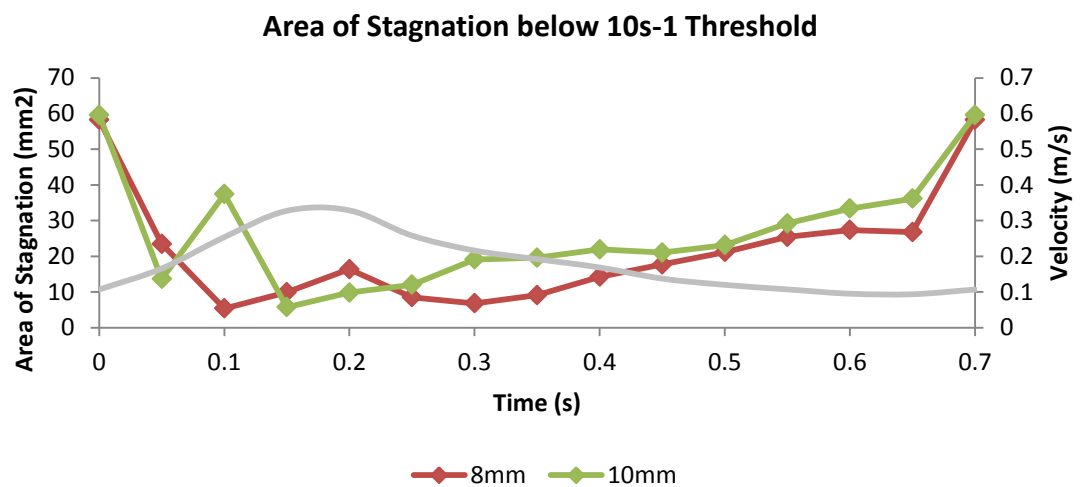


Figure 51. The area of stagnation, measured using the SSR threshold, on the surface of the cavity at each time step for the blunt monophasic velocity profile in the 8mm vessel.

The smaller diameter experience smaller areas of stagnation throughout the cycle. The smallest areas of stagnation occur during the peak forward flow at 0.15s for the 10mm vessel and at 0.1s for the 8mm vessel. Vector plots of the flow in the cavity were analysed at time steps of 0.1s, 0.15s and 0.3s and are shown in Figure 52.

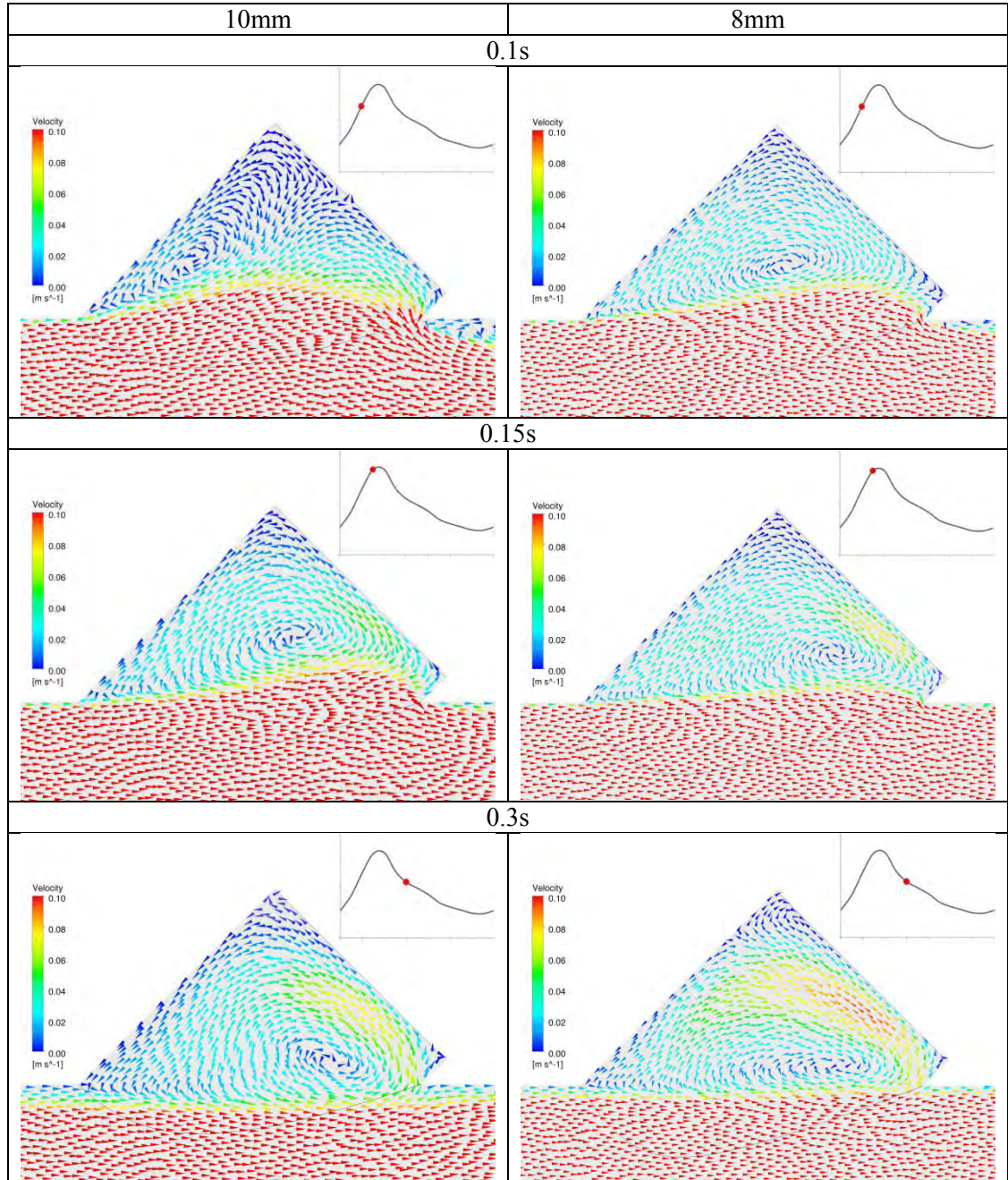


Figure 52. Comparison of the blunt monophasic velocity field for the 8mm and 10mm cases at 0.1, 0.15, and 0.2s.

The vector plots show an increase in velocity of the flow in the cavity for the smaller vessel. The increased velocity pushes the vortex closer to the distal corner at 0.15s; however, the higher velocity also results in smaller low velocity regions at 0.1s and 0.3s. The smaller diameter results in a larger fluid velocity in the cavity for all of the time steps. The higher velocities increase the chance of removing more stagnation in the

cavity. Though the proximal corner of the cavity still experiences low velocity flow for the duration of the cycle. Figure 53 compares the locations below the SSR threshold for the three time steps and throughout the cycle. The plots reveal a much smaller area of stagnation in the 8mm vessel at 0.1s and 0.3s compared to the 10mm vessel.

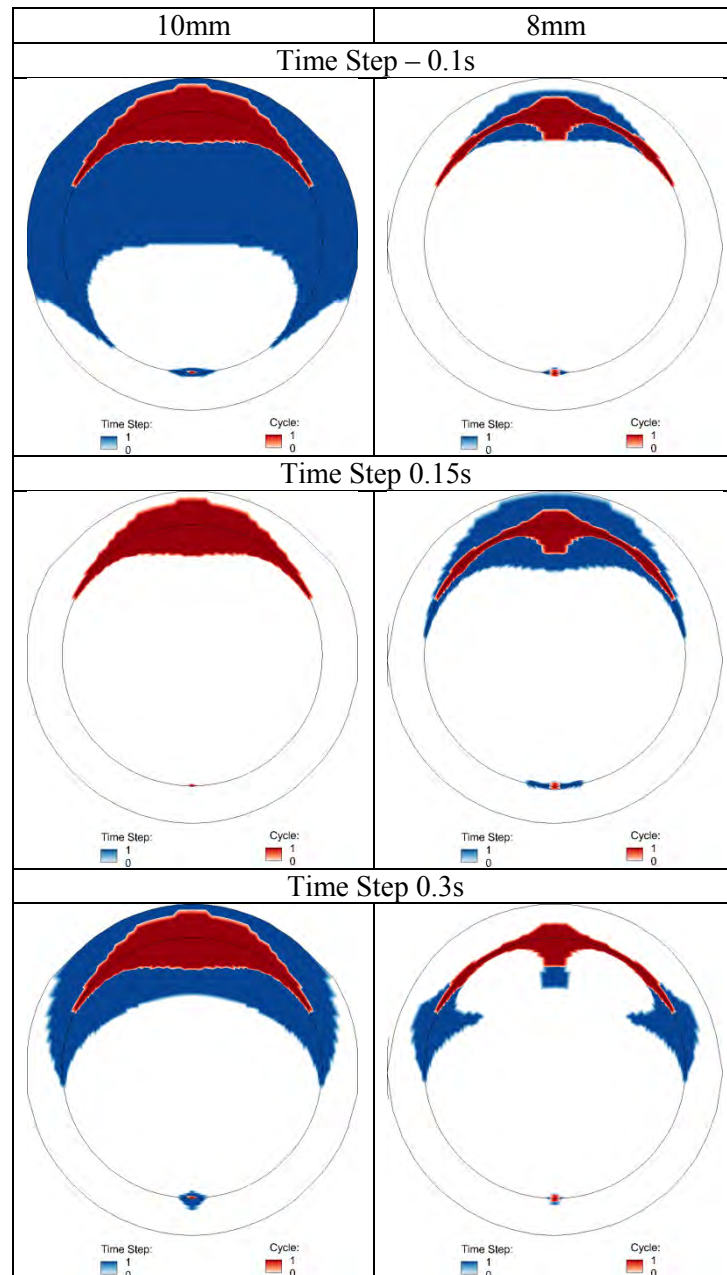


Figure 53. Comparison of the area of stagnation, $SSR < 10s^{-1}$, on the stopper surface between the 10mm and 8mm diameter vessels for the blunt monophasic wave (Red) and for the entire cycle, $SI=1$ (Blue).

The SI and RT on the surface of the cavity are shown in Figure 54. It shows a reduction in the area of stagnation calculated from both the SI and the RT, but similar stagnation index across the surface.

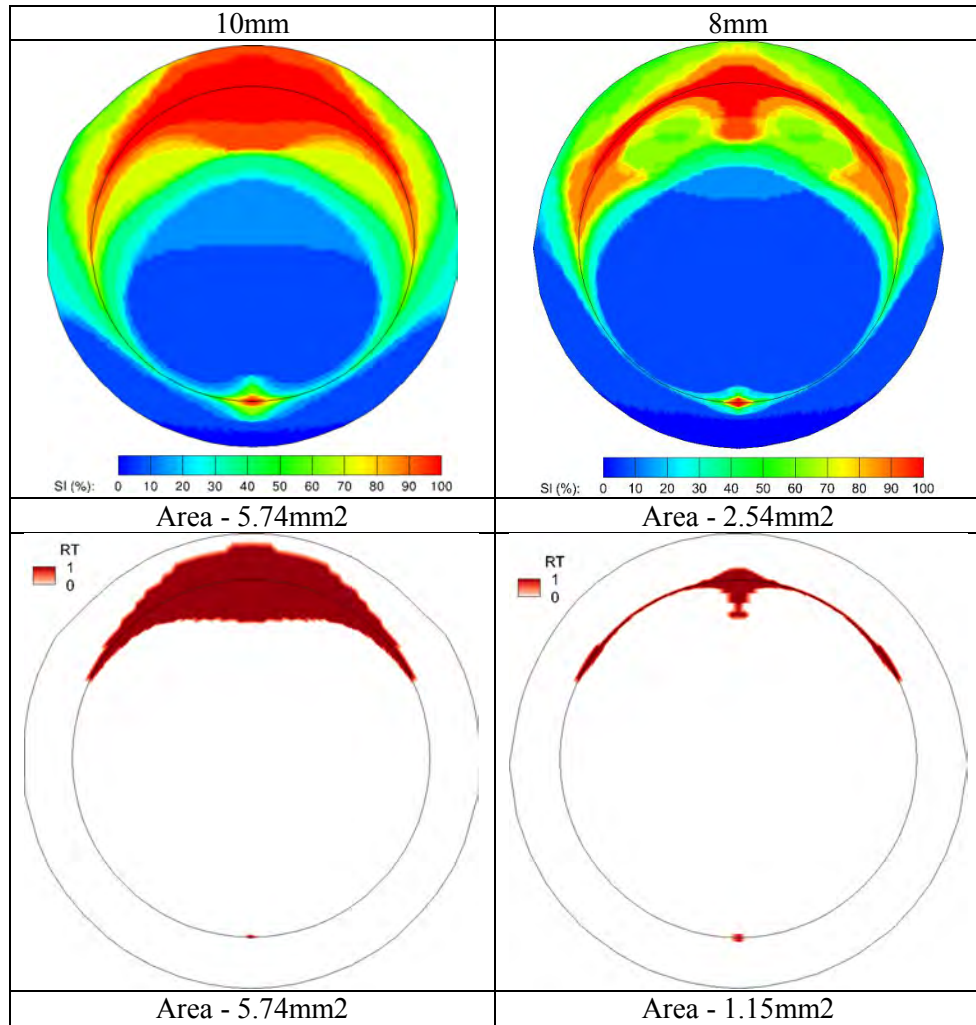


Figure 54. Comparison of the SI and RT (RT>1) between the 10mm and 8mm diameter vessels for the blunt monophasic wave.

4.2.2 Sharp Monophasic Velocity Wave

The graph in Figure 55 compares the area of stagnation, calculated from the SSR, at each time step for the 8mm and 10mm vessel diameters with the sharp monophasic velocity wave.

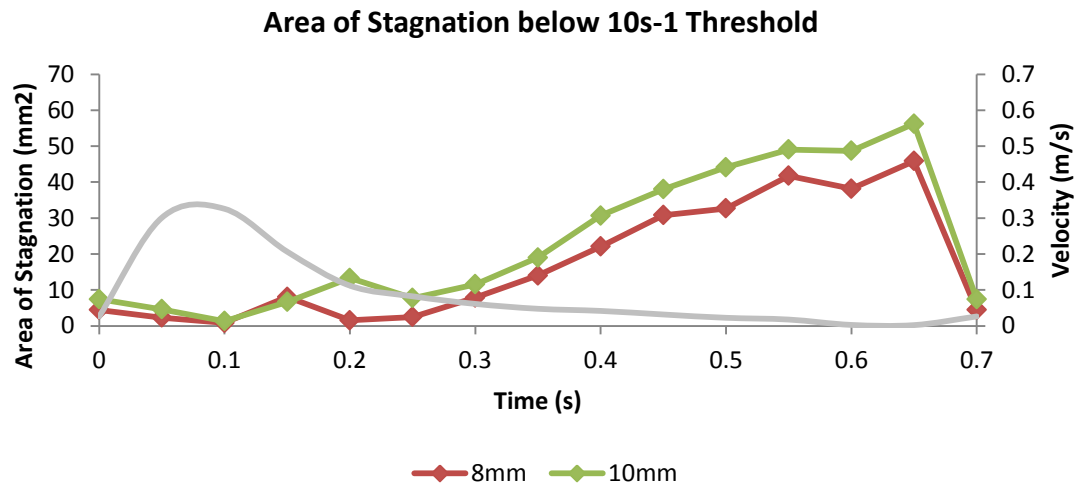


Figure 55. The area of stagnation, measured using the SSR threshold, on the surface of the cavity at each time step for the sharp monophasic velocity profile in the 8mm vessel.

The smaller diameter experiences smaller areas of stagnation throughout the cycle. The smallest areas of stagnation occur during the peak forward flow at 0.1s in both cases.

Vector plots of the flow in the cavity were analysed at time steps of 0.1s and 0.25s and are shown in Figure 56. The vector plots show an increase in velocity of the flow in the cavity for the smaller vessel. The increased velocity causes smaller low velocity regions in both the proximal and distal corners at both time steps.

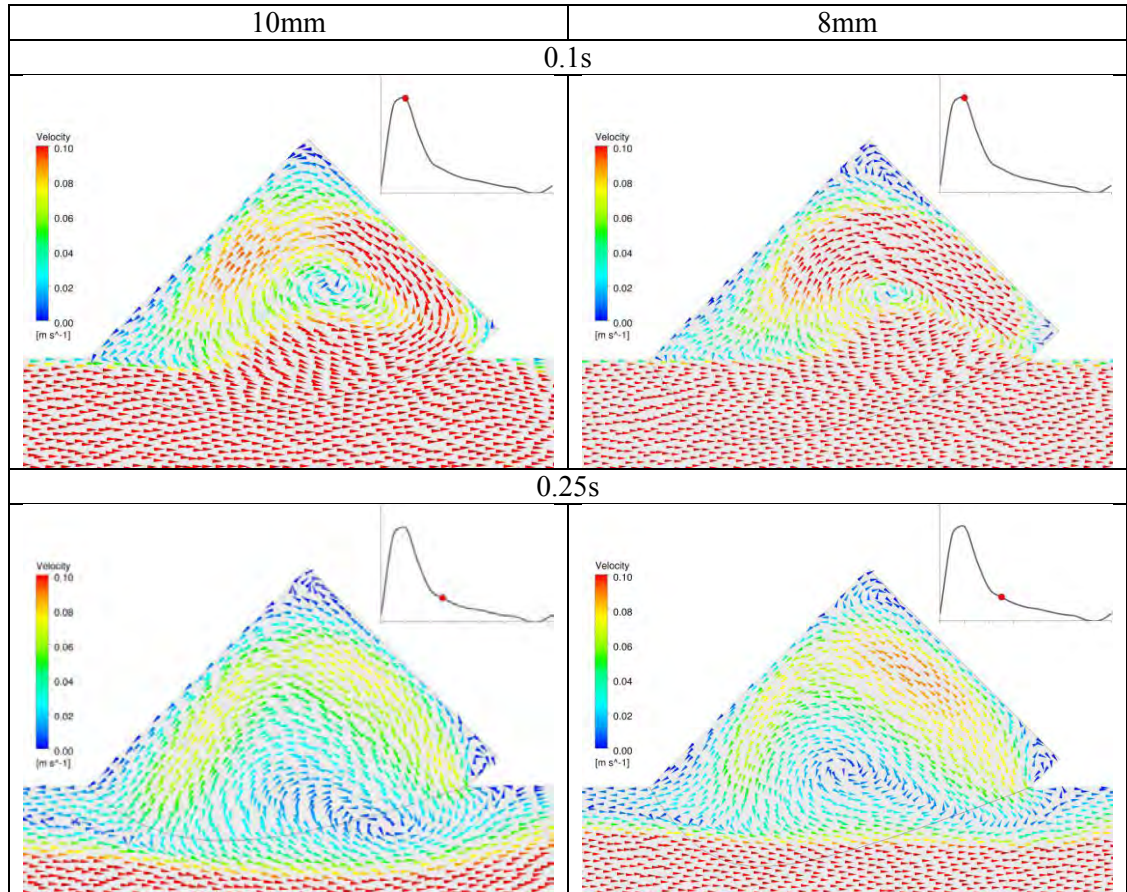


Figure 56. Comparison of the sharp monophasic velocity field for the 8mm and 10mm cases at 0.05, 0.1, and 0.25s.

Figure 57 compares the locations below the SSR threshold for the two time steps and throughout the cycle. The plots reveal a much smaller area of stagnation in the 8mm vessel at both time steps compared to the 10mm vessel. The plots also show that the proximal cavity is flushed out more at 0.25s in the 8mm vessel compared to 0.1s in the 10mm vessel.

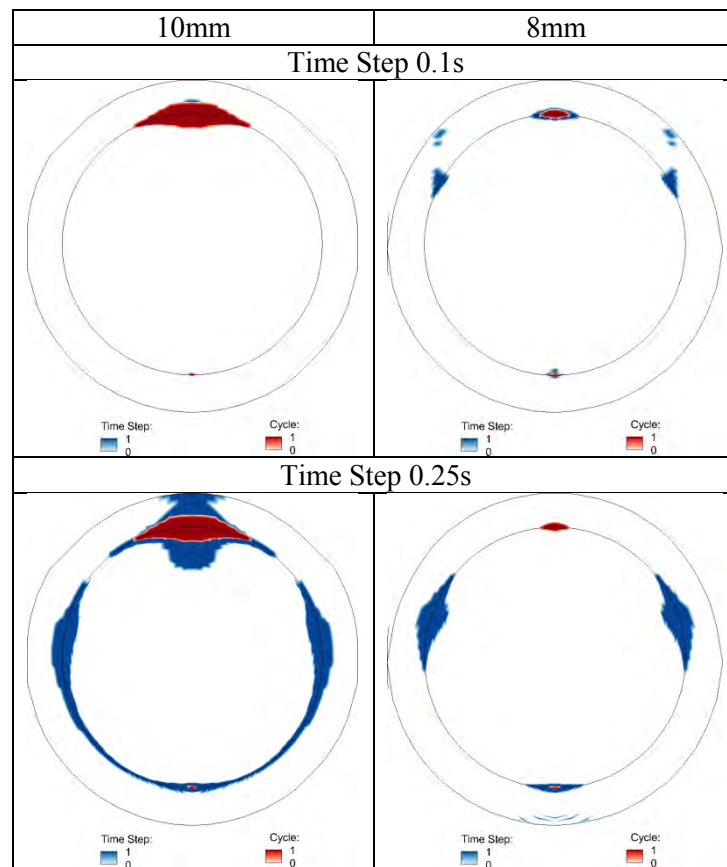


Figure 57. Comparison of the area of stagnation, $SSR < 10s^{-1}$, on the stopper surface between the 10mm and 8mm diameter vessels for the sharp monophasic wave (Red) and for the entire cycle, $SI=1$ (Blue).

The SI and RT on the surface of the cavity are shown in Figure 58. It shows a reduction in the area of stagnation calculated from both the SI and the RT.

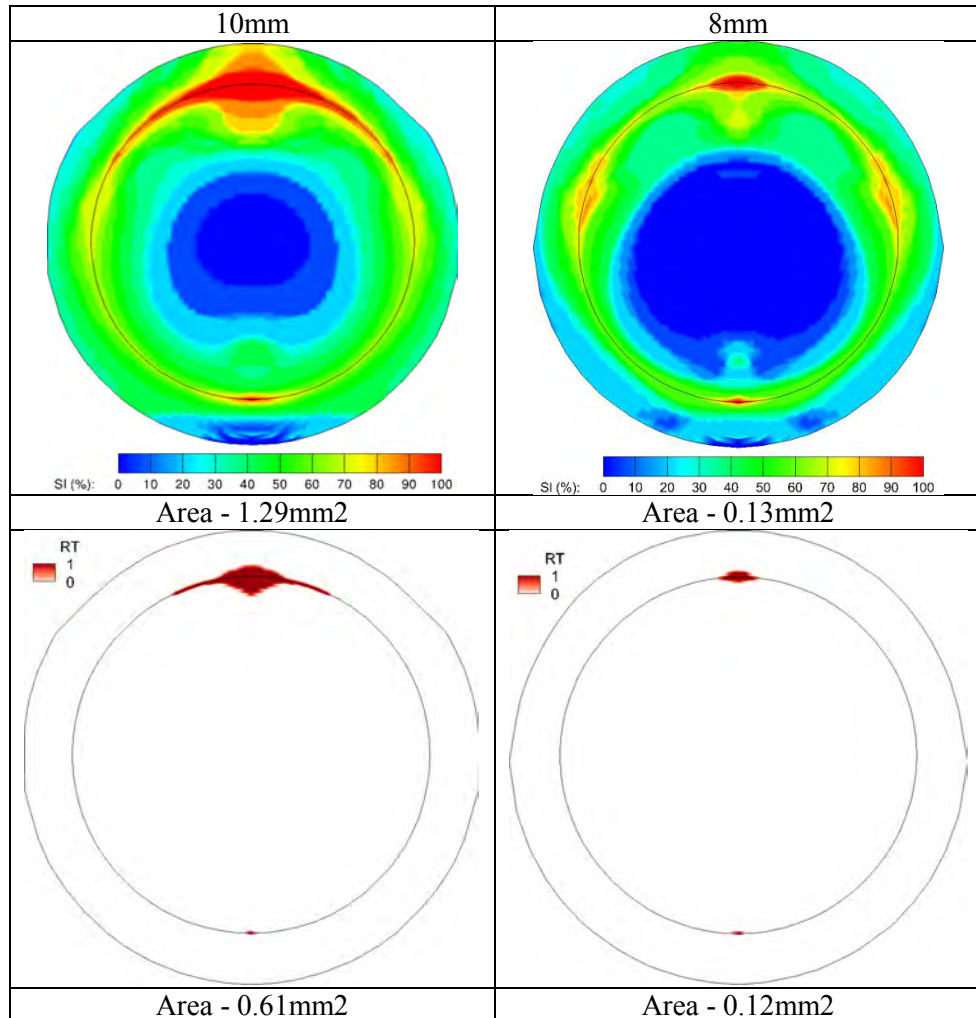


Figure 58. Comparison of the SI and RT (RT>1) between the 10mm and 8mm diameter vessels for the sharp monophasic wave.

4.2.3 Biphasic Velocity Wave

The graph in Figure 59 compares the area of stagnation, calculated from the SSR, at each time step for the 8mm and 10mm vessel diameters with the biphasic velocity wave. The smaller diameter experience smaller areas of stagnation throughout the cycle. The smallest areas of stagnation occur during the peak flow and flow reversal in both cases.

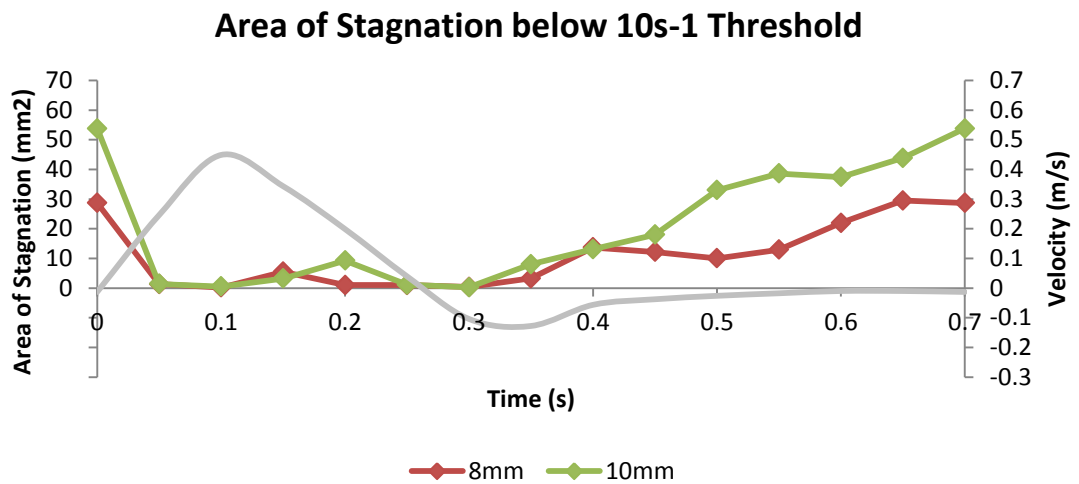


Figure 59. The area of stagnation, measured using the SSR threshold, on the surface of the cavity at each time step for the biphasic velocity profile in the 8mm vessel.

Vector plots of the flow in the cavity were analysed at time steps of 0.1s and 0.25s and are shown in Figure 60. The vector plots reveal high velocities at both time steps in the 8mm vessel compared to the 10mm vessel. The higher velocities cause smaller low velocity regions in both the proximal and distal corners of the device.

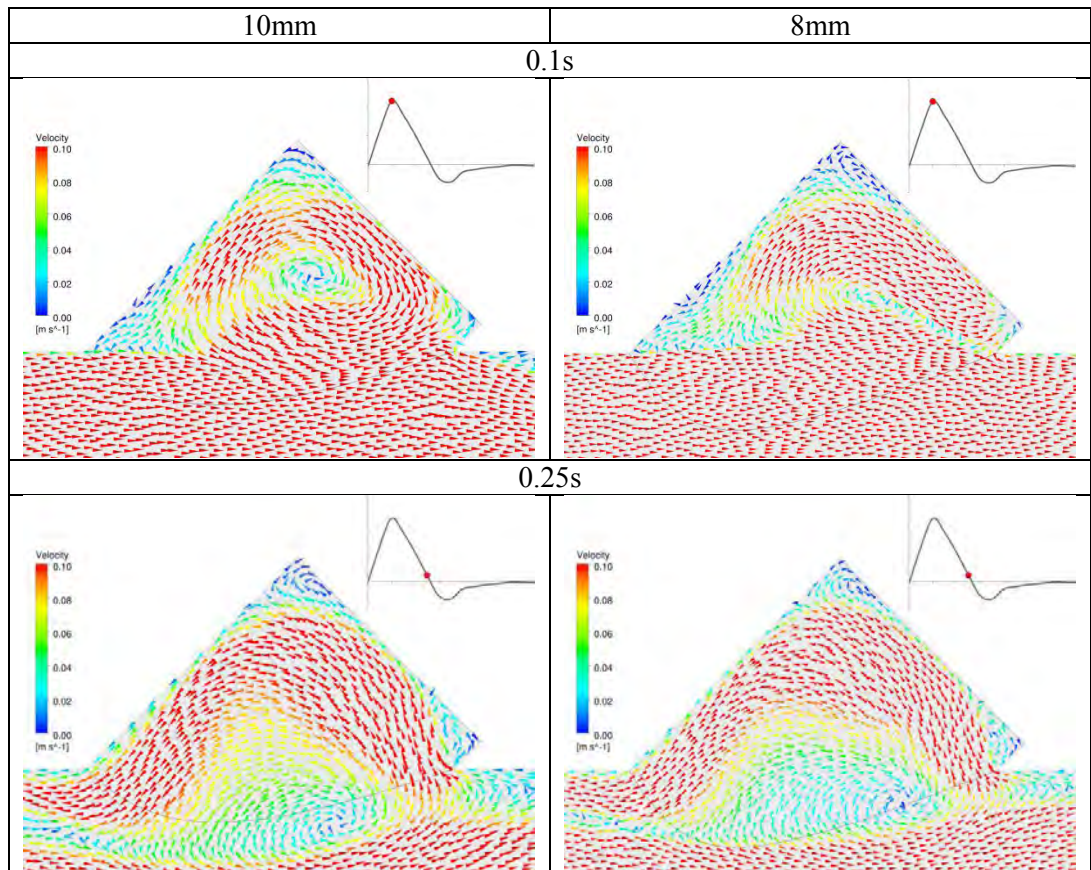


Figure 60. Comparison of the biphasic velocity field for the 8mm and 10mm cases at 0.1 and 0.25s.

Figure 61 compares the locations below the SSR threshold for the two time steps and throughout the cycle. The plots reveal similar areas of stagnation in the 8mm vessel at both time steps compared to the 10mm vessel.

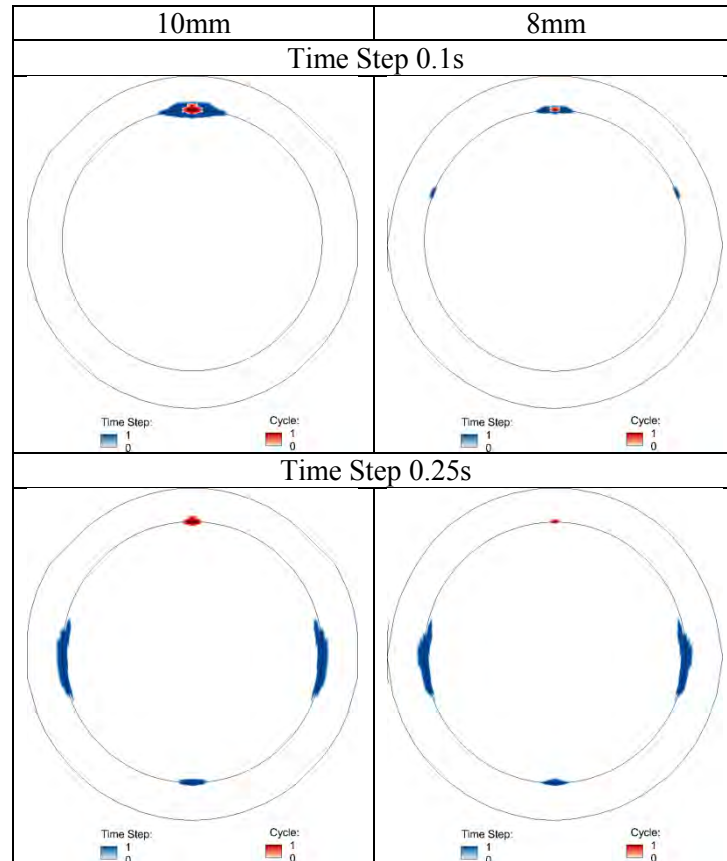


Figure 61. Comparison of the area of stagnation, $SSR < 10\text{s}^{-1}$, on the stopper surface between the 10mm and 8mm diameter vessels for the biphasic wave (Red) and for the entire cycle, $SI=1$ (Blue).

The SI and RT on the surface of the cavity are shown in Figure 62. It shows a reduction in the area of stagnation calculated from both the SI and the RT.

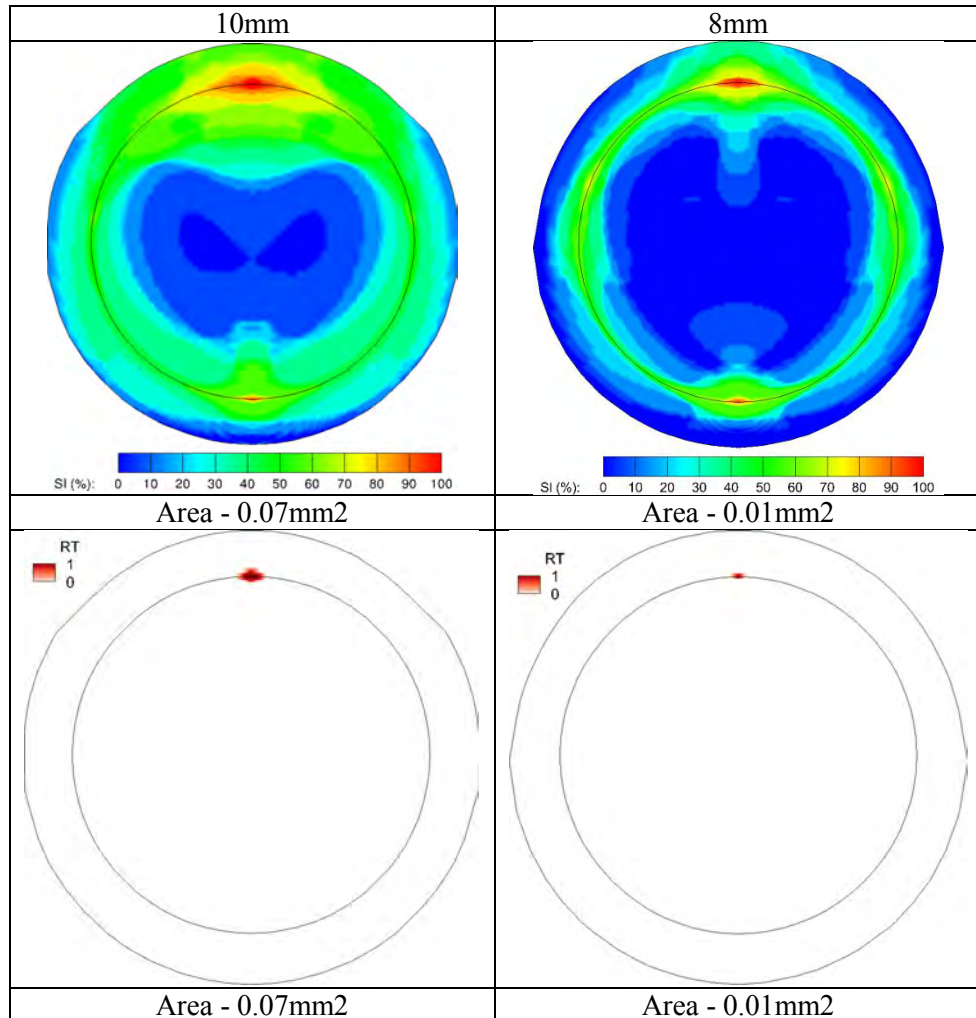


Figure 62. Comparison of the SI and RT (RT>1) between the 10mm and 8mm diameter vessels for the biphasic wave.

4.2.4 Triphasic Velocity Wave

The graph in Figure 63 compares the area of stagnation, calculated from the SSR, at each time step for the 8mm and 10mm vessel diameters with the triphasic velocity wave.

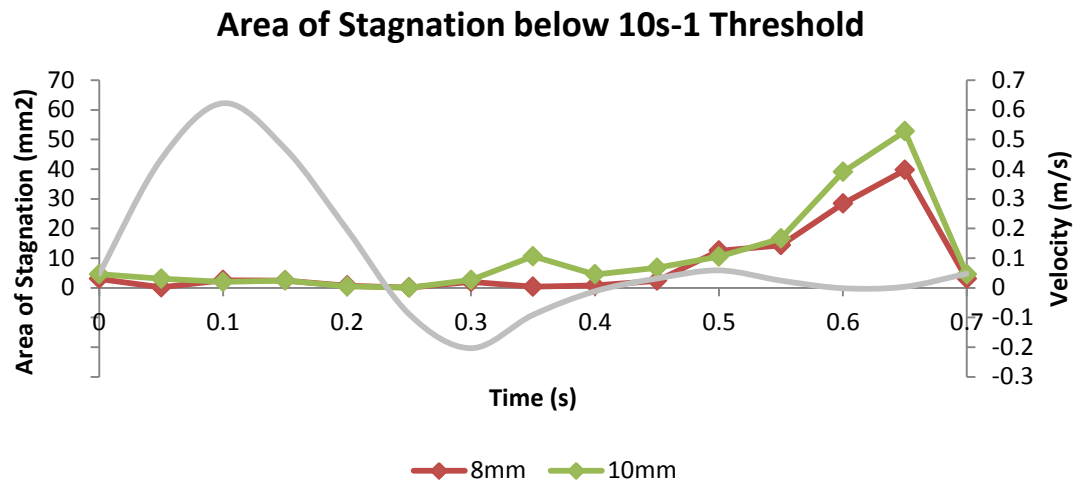


Figure 63. The area of stagnation, measured using the SSR threshold, on the surface of the cavity at each time step for the triphasic velocity profile in the 8mm vessel.

The smaller diameter experience smaller areas of stagnation throughout the cycle. The smallest areas of stagnation occur during the flow reversal between 0.2s and 0.25s in both cases. Vector plots of the flow in the cavity were analysed at time steps of 0.1s, 0.15s, 0.2s, and 0.25s and the results are shown in Figure 64. The vector plots reveal higher velocities during all of the time steps in the 8mm vessel compared to the 10mm vessel. The higher velocities cause smaller low velocity regions in both the proximal and distal corners of the device.

Figure 65 compares the locations below the SSR threshold for the four time steps and throughout the cycle. The plots reveal a slightly smaller area of stagnation in the 8mm vessel during all of the time steps compared to the 10mm vessel.

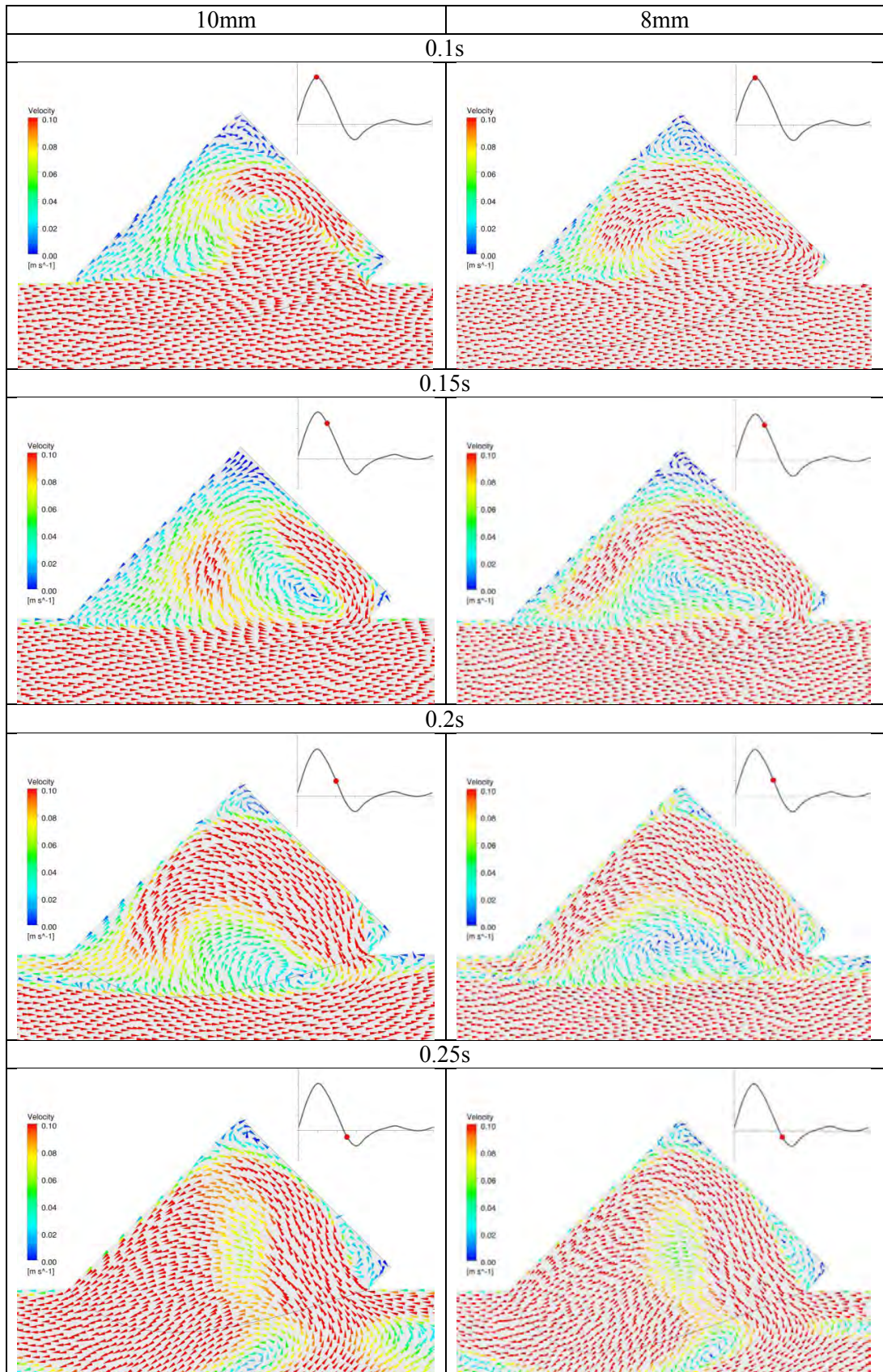


Figure 64. Comparison of the triphasic velocity field for the 8mm and 10mm cases at 0.1, 0.15, 0.2, and 0.25s.

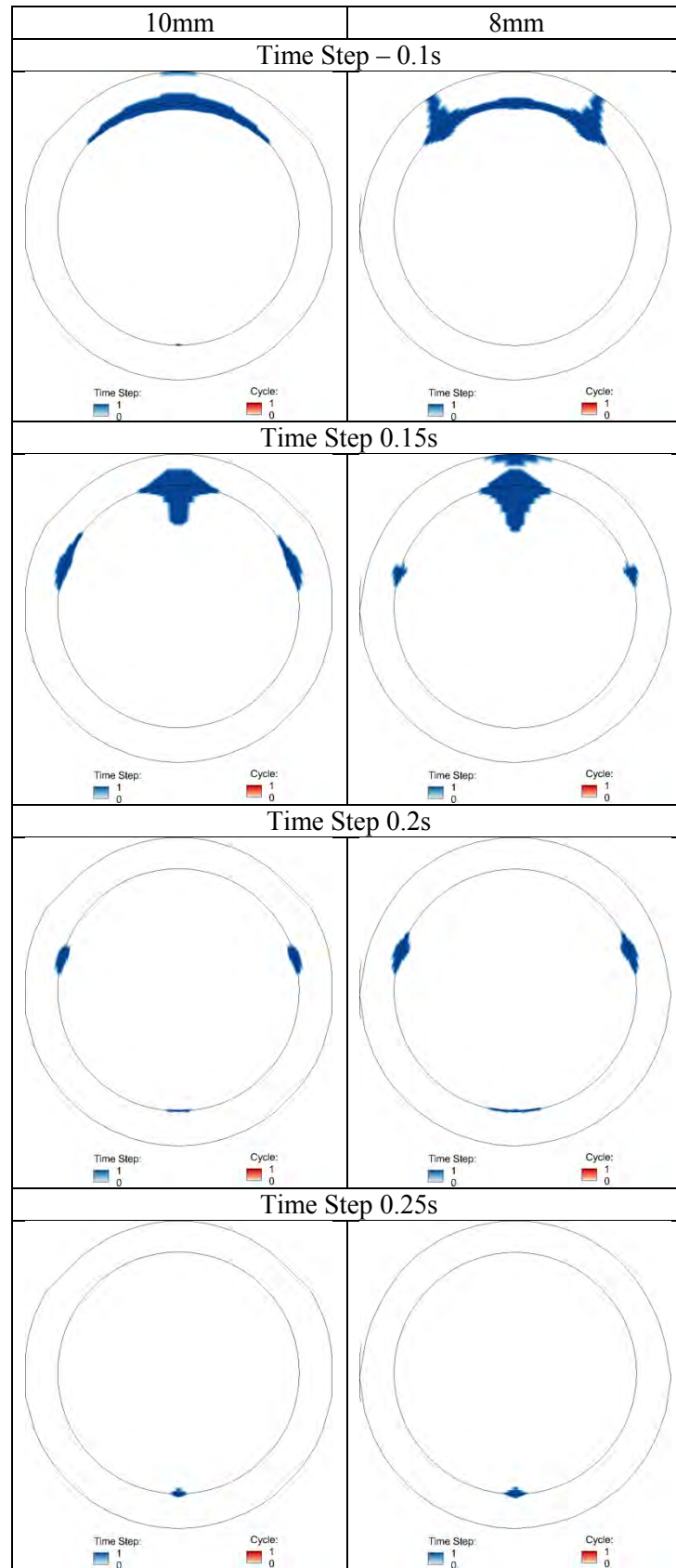


Figure 65. Comparison of the area of stagnation, $SSR < 10s^{-1}$, on the stopper surface between the 10mm and 8mm diameter vessels for the triphasic wave (Red) and for the entire cycle, $SI=1$ (Blue).

The SI and RT on the surface of the cavity are shown in Figure 66 and both reveal similar shear rates across the surface of the cavity and no thrombus formation.

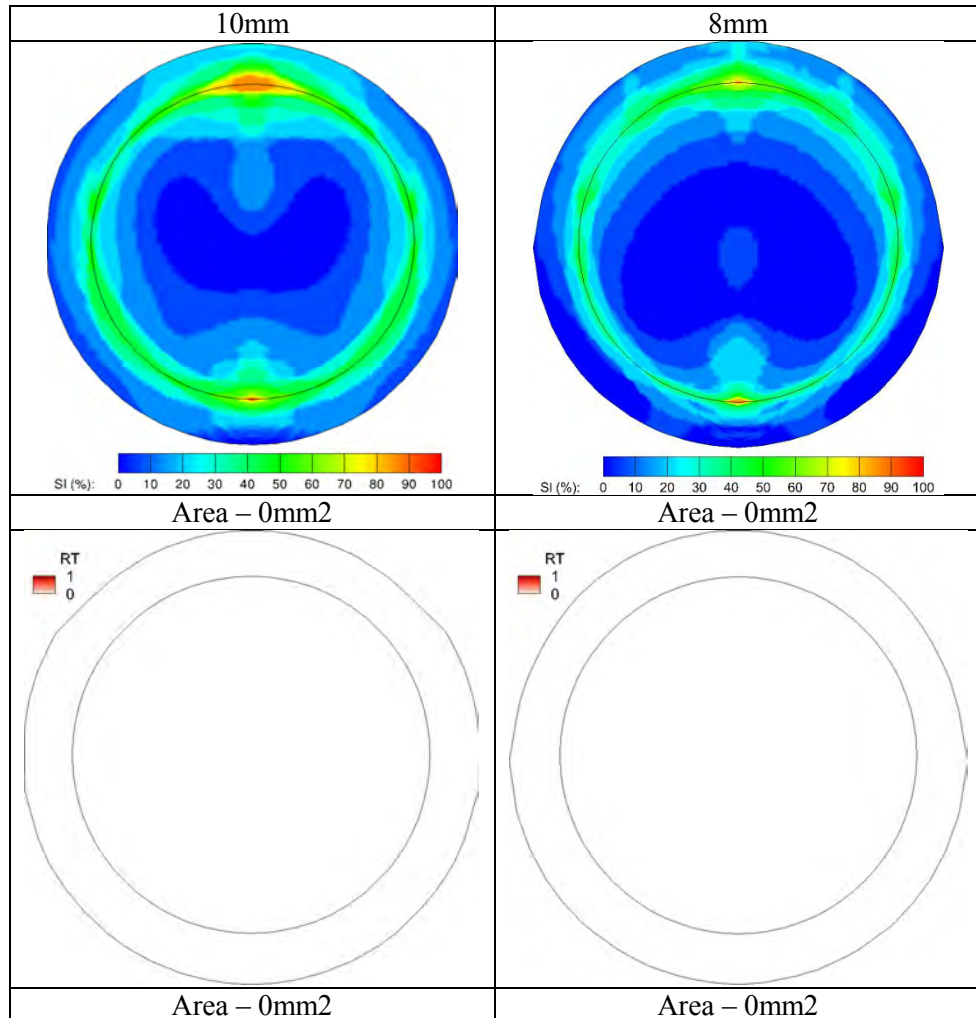


Figure 66. Comparison of the SI and RT (RT>1) between the 10mm and 8mm diameter vessels for the triphasic wave.

CHAPTER 5 - RESULTS

GEOMETRICAL CONDITIONS

The previous chapter explored different flow conditions in the cavity as a result of different physiological factors. This chapter investigates the effect of geometrical factors on the flow conditions in the device and the risk of thrombus formation. The characteristics of the device that were analysed are the distance of the device upstream from the femoral occlusion, the depth of the cavity, and the angle of attachment of the device. The results were used to determine the optimal position of the device for the four physiological velocity waves.

5.1 DISTANCE

The distance of the device from the stenosis was expected to affect the flow in the cavity due to the jetting flow produced by the stenosis and the retrograde flow in the triphasic and biphasic velocity profiles. The device was examined at three distances upstream from the femoral occlusion; 5D, 10D, and 15D for the biphasic and triphasic velocity waves. Figure 67 shows the location and size of the area of stagnation, predicted by RT, for the three different distances. The results reveal that there is no difference in the likelihood of thrombus formation for the three device positions exposed to either velocity wave.

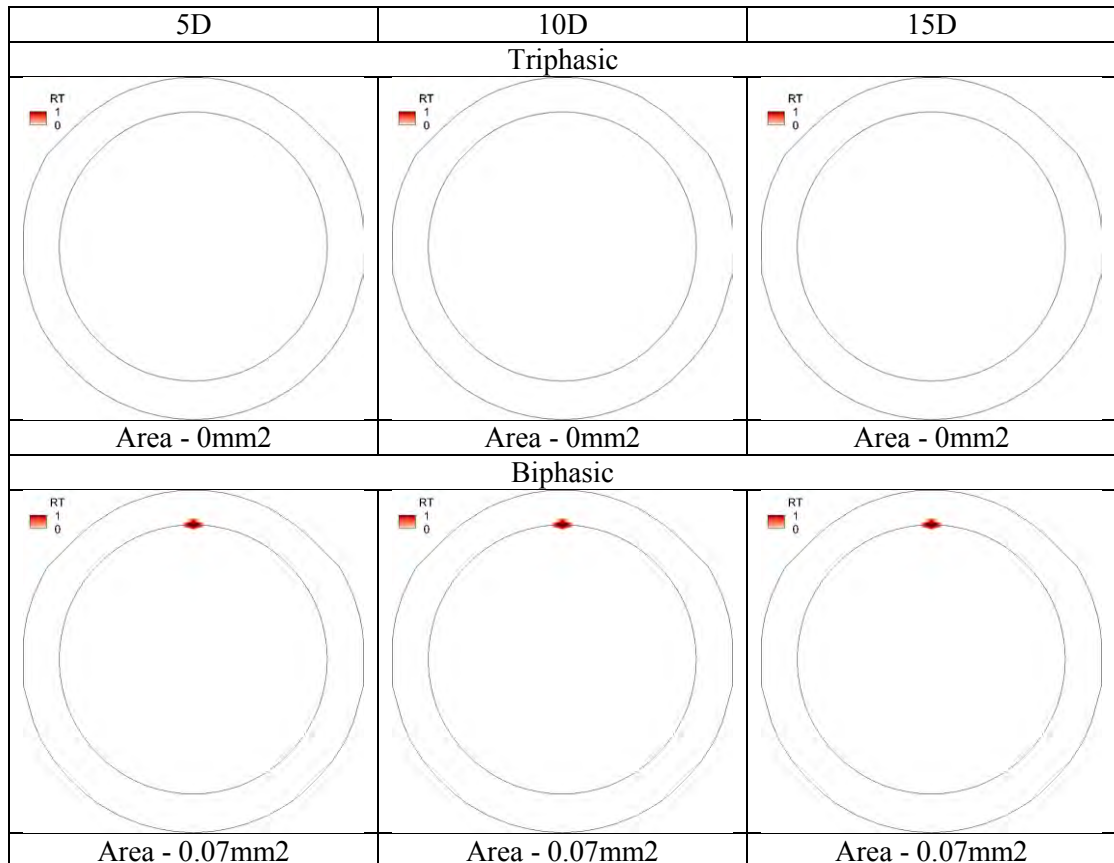


Figure 67. The area of stagnation on the surface of the cavity, $RT > 1$, with the device at 5D, 10D, and 15D upstream of the femoral occlusion.

5.2 DEPTH

An increase in the depth of the cavity results in a greater volume of fluid separated from the main flow in the vessel. Blood closer to the stopper was expected to have a lower velocity than the blood near the vessel and consequently a deeper cavity was expected to produce a larger volume of stagnated blood. The device was analysed at depths of 1mm, 3mm and 5mm for each of the four physiological velocity waves.

5.2.1 Blunt Monophasic

The location and size of the area of stagnation, predicted by RT and SI, for the three depths is shown in Figure 68. It presents the relationship between the depth of the cavity and thrombus formation for the blunt monophasic velocity wave.

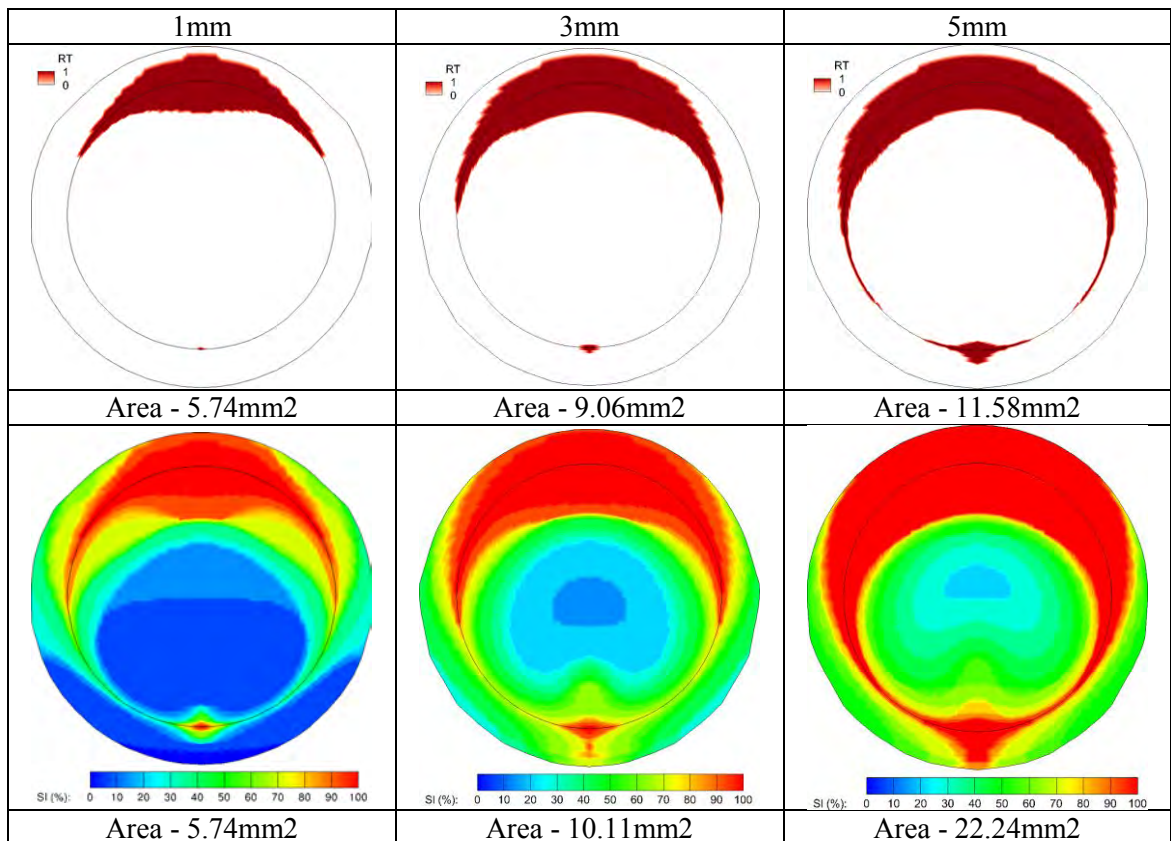


Figure 68. Comparison of RT ($RT > 1$) and SI on the surface of the cavity for the three cavity depths of 1mm, 3mm, and 5mm for the blunt monophasic wave.

The area of thrombus formation increases as the depth increases. It forms in the proximal corner at a depth of 1mm and extends around the edge of the stopper surface as the depth is increased to 3mm and 5mm. The SI shows an increase not only in the area of stagnation, but in the SI on the entire surface as the depth increases.

Figure 69 compares the size and location of the area of stagnation, calculated by the SSR, at time steps that cause the smallest area of stagnation in the cycle. The smallest

area of stagnation occurs during peak flow (0.15s) for the 1mm and 3mm cases and decelerating flow (0.25s) for the 5mm case. The plots show how the area of stagnation increases as the depth of the cavity increases at individual time steps.

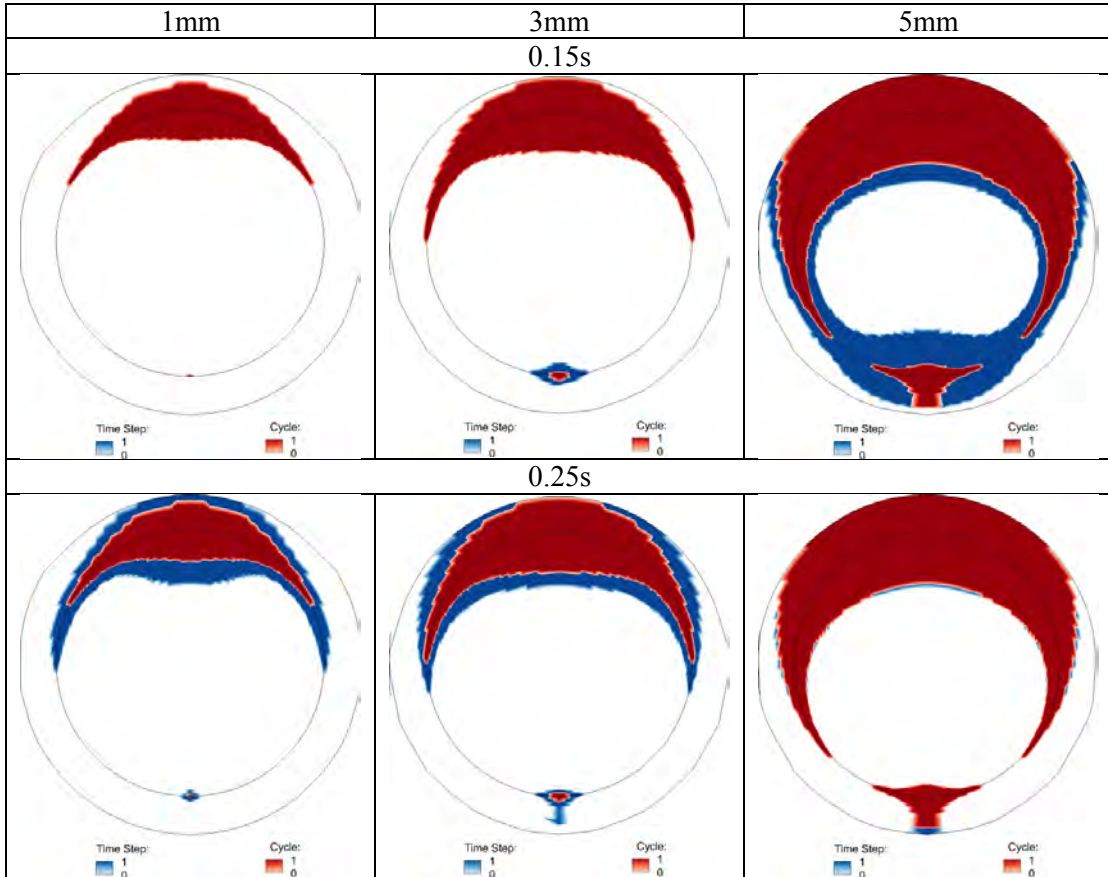


Figure 69. Comparison of the area of stagnation, $SSR < 10s^{-1}$, at 0.15s and 0.25s for the three cavity depths of 1mm, 3mm, and 5mm for the blunt monophasic wave (Red) and for the entire cycle, $SI=1$ (Blue).

Figure 70 compares the velocity in the cavity at the time steps that cause the smallest area of stagnation in the cycle. The vector plots demonstrate the effect of the increase in depth on the flow in the cavity. The flow at the entrance of the cavity is the same and the deeper cavity allows the flow to develop further, but the increase in fluid creates larger regions of low velocity fluid near the stopper surface.

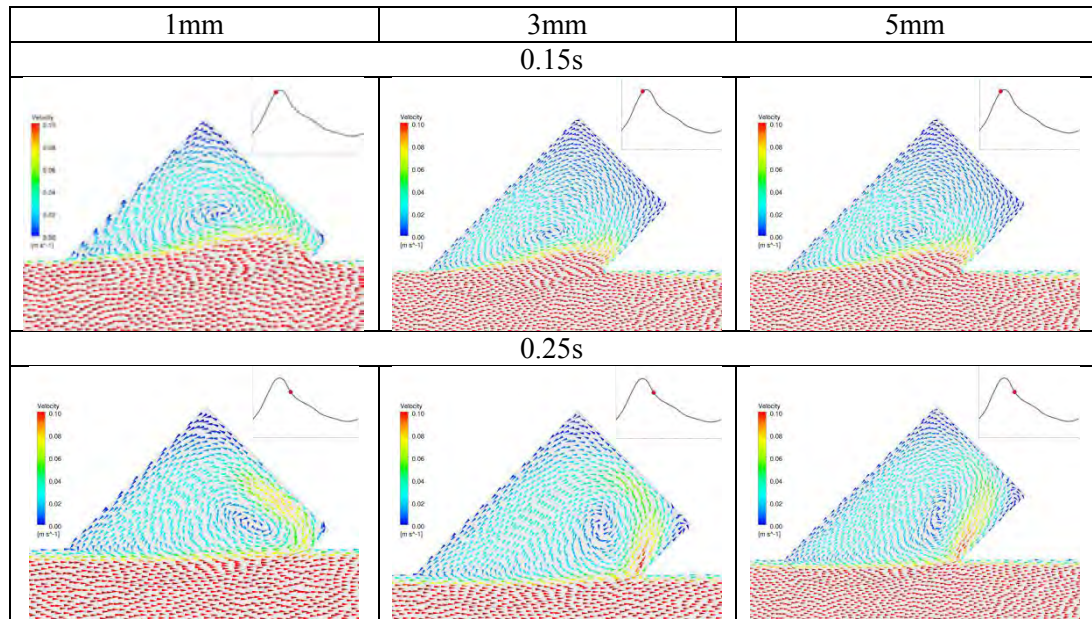


Figure 70. Comparison of the velocity field in the cavity at 0.15s and 0.25s for the three cavity depths of 1mm, 3mm, and 5mm for the blunt monophasic wave.

5.2.2 Sharp Monophasic

The location and size of the area of stagnation, predicted by RT and SI, for the three depths is shown in Figure 71. It identifies the relationship between the depth of the cavity and thrombus formation for the sharp monophasic velocity wave. The area of thrombus formation increases as the depth increases and shows the same progression as the blunt monophasic case. It originates in the proximal corner at a depth of 1mm and extends around the edge of the stopper surface as the depth is increased to 3mm and 5mm. The SI shows an increase not only in the area of stagnation, but in the SI on the entire surface as the depth increases

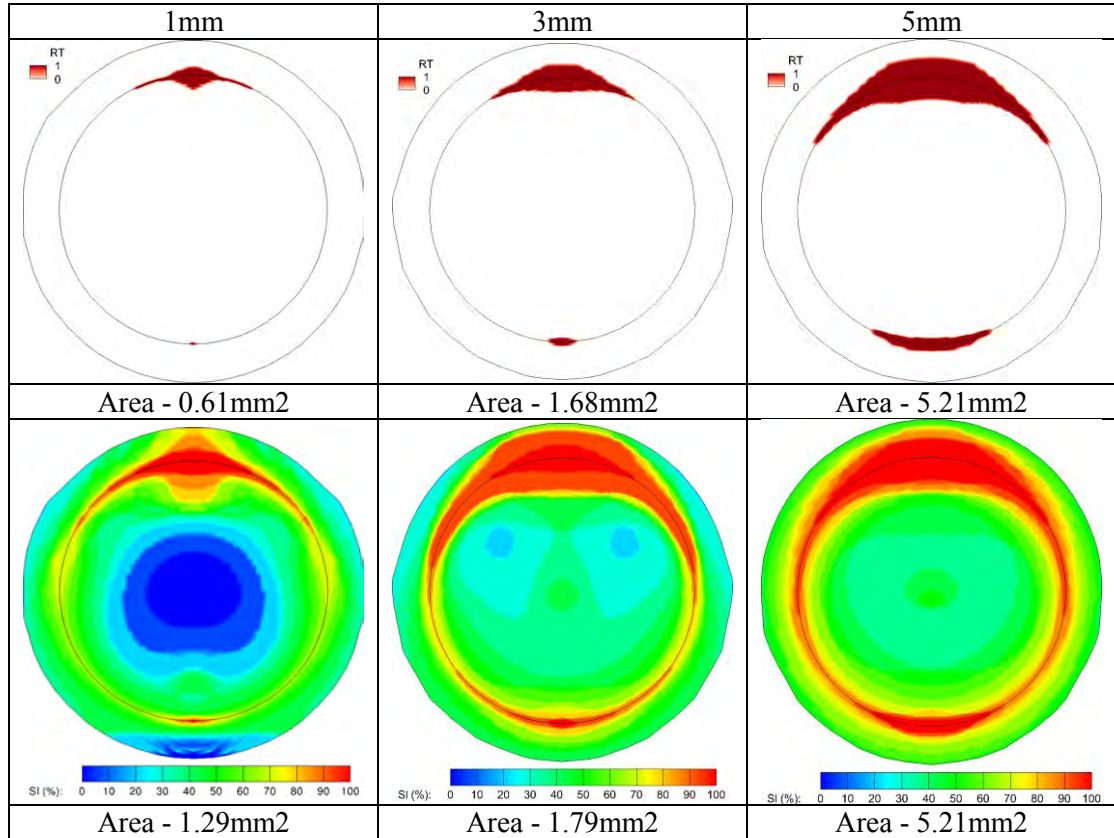


Figure 71. Comparison of the RT (RT>1) and SI on the surface of the cavity for the three cavity depths of 1mm, 3mm, and 5mm for the sharp monophasic wave.

Figure 72 compares the size and location of the area of stagnation, calculated by the SSR, at time steps that cause the smallest area of stagnation in the cycle. The smallest area of stagnation occurs during peak flow (0.1s) for all three depths. The plots show how the area of stagnation increases as the depth of the cavity increases during peak flow.

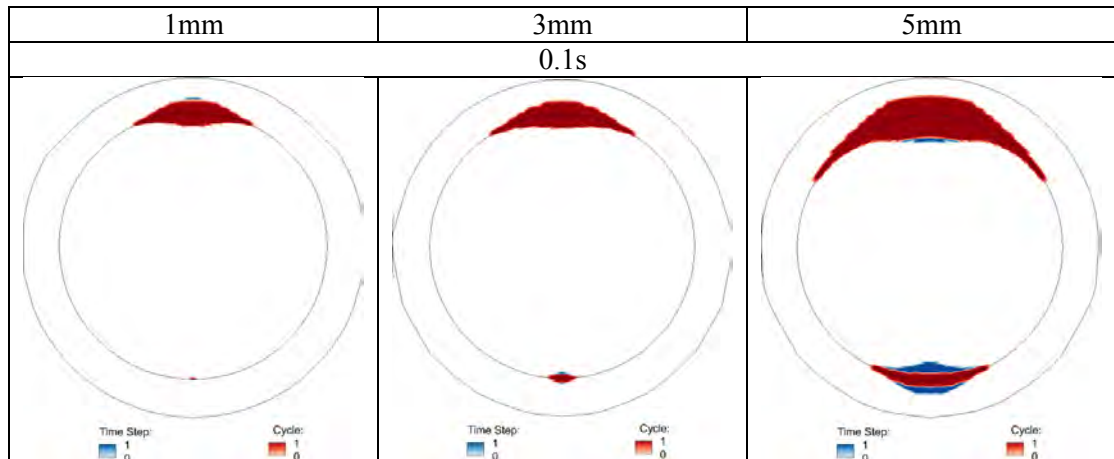


Figure 72. Comparison of the area of stagnation, $SSR < 10s^{-1}$, at 0.1s for the three cavity depths of 1mm, 3mm, and 5mm for the sharp monophasic wave (Red) and for the entire cycle, $SI=1$ (Blue).

Figure 73 compares the velocity in the cavity at the time steps that cause the smallest area of stagnation in the cycle. The vector plots reveal the effect of the increase in depth on the flow in the cavity. As with the blunt monophasic case, the flow in the deeper cavities is an extension of the flow in the 1mm cavity. The increase in fluid and distance from the femoral flow results in larger low velocity regions near the stopper surface.

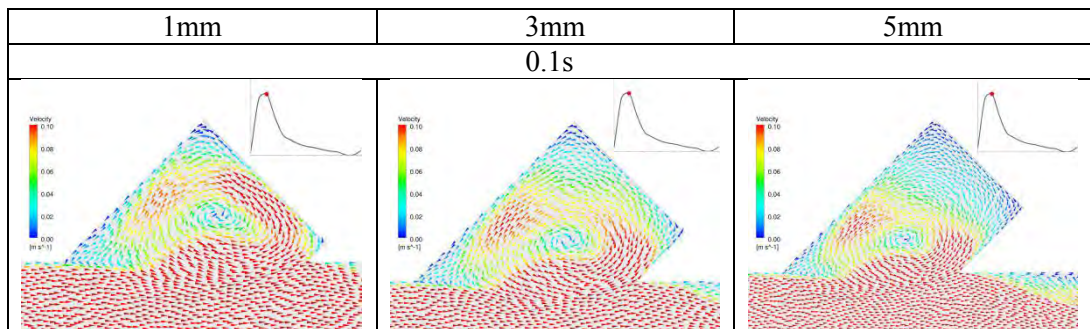


Figure 73. Comparison of the velocity field in the cavity at 0.1s for the three cavity depths of 1mm, 3mm, and 5mm for the sharp monophasic wave.

5.2.3 Biphasic

The location and size of the area of stagnation, predicted by RT and SI, for the three depths is shown in Figure 74. It presents the relationship between the depth of the cavity and thrombus formation for the biphasic velocity wave. The area of thrombus formation increases as the depth increases and is consistent in forming in the proximal corner. The SI shows an increase not only in the area of stagnation, but in the SI on the entire surface as the depth increases.

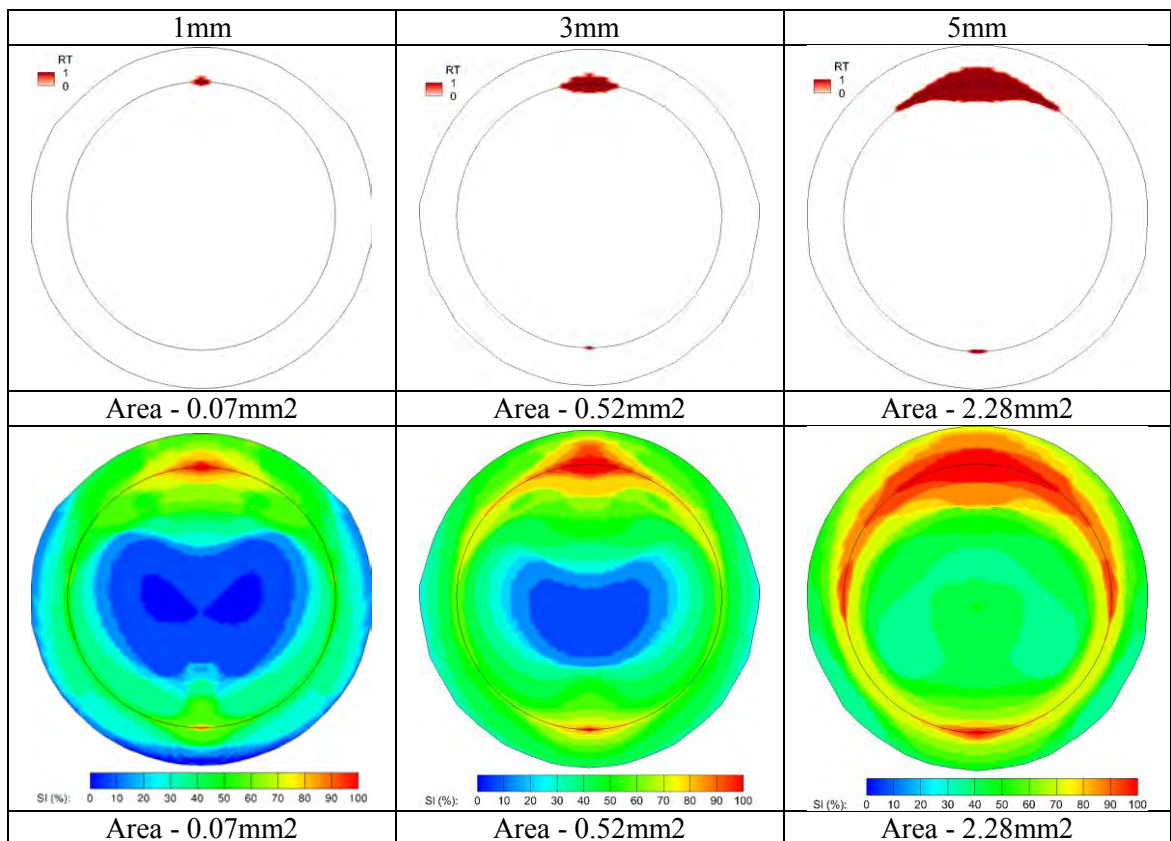


Figure 74. Comparison of the RT (RT>1) and SI on the surface of the cavity for the three cavity depths of 1mm, 3mm, and 5mm for the biphasic wave.

Figure 75 compares the size and location of the area of stagnation, calculated by the SSR, at time steps that cause the smallest area of stagnation in the cycle. The smallest area of stagnation occurs during peak flow (0.1s) for 5mm case and the distal corner for

the 1mm and 3mm cases. The reverse flow (0.3s) results in the smallest area of stagnation in the proximal corner for the 1mm and 3mm cases. The plots show how the area of stagnation increases as the depth of the cavity increases at individual time steps.

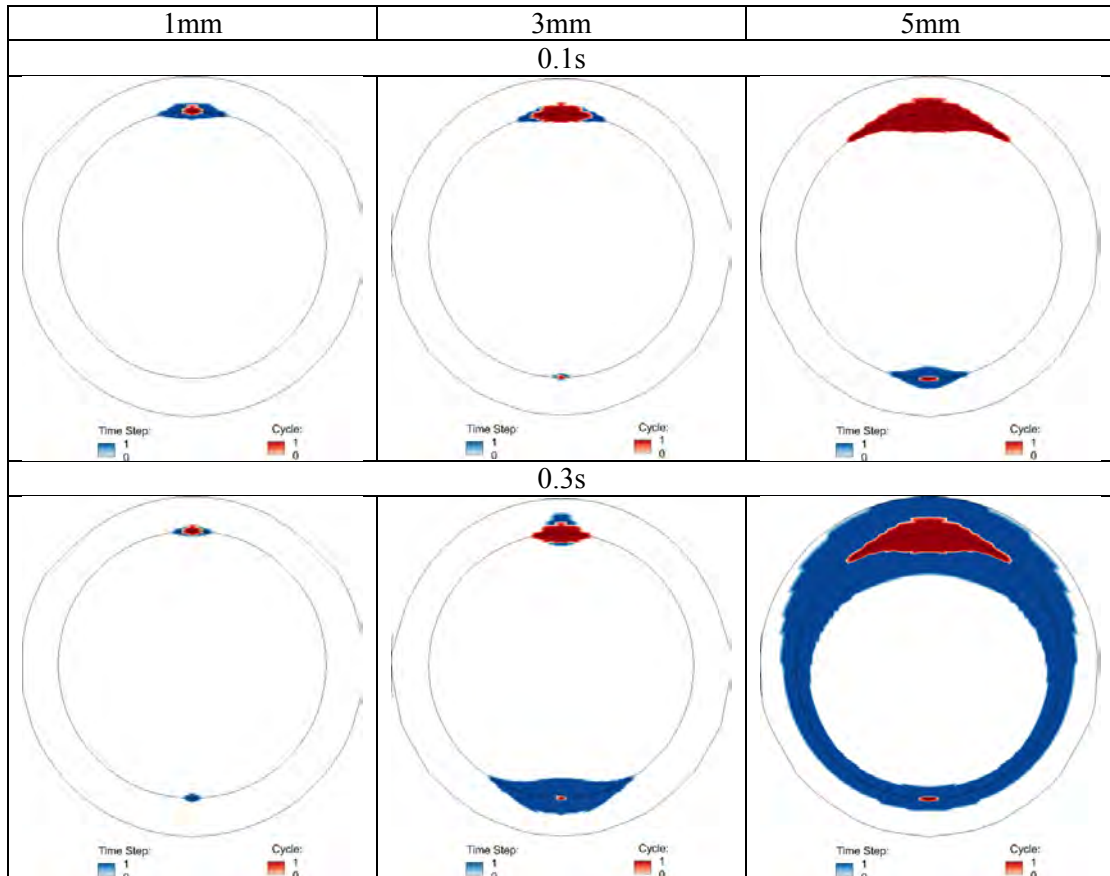


Figure 75. Comparison of the area of stagnation, $SSR < 10s^{-1}$, at 0.1s and 0.3s for the three cavity depths of 1mm, 3mm, and 5mm for the biphasic wave (Red) and for the entire cycle, $SI=1$ (Blue).

Figure 76 compares the velocity in the cavity at the time steps that cause the smallest area of stagnation in the cycle. The vector plots demonstrate the effect of the increase in depth on the flow in the cavity. The flow in the 3mm and 5mm cavities is an extension of the flow in the 1mm cavity, but the increase in fluid creates larger regions of low velocity fluid near the stopper surface.

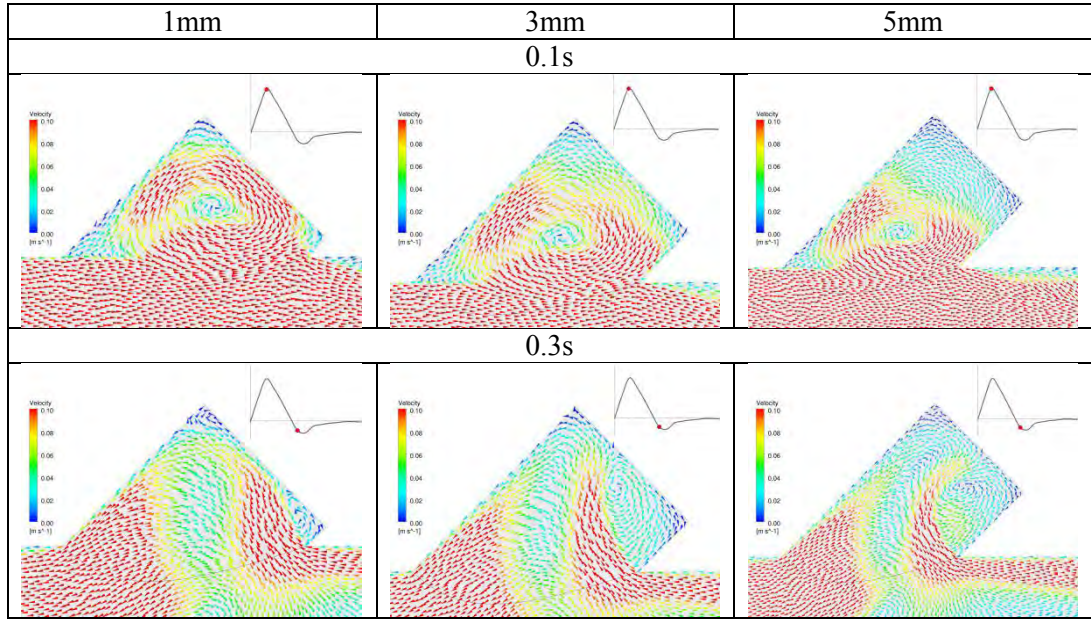


Figure 76. Comparison of the velocity field in the cavity at 0.1s and 0.3s for the three cavity depths of 1mm, 3mm, and 5mm for the biphasic wave.

5.2.4 Triphasic

The location and size of the area of stagnation, predicted by RT and SI, for the three depths is shown in Figure 77. It presents the relationship between the depth of the cavity and thrombus formation for the triphasic velocity wave. The area of thrombus formation increases as the depth increases. There was no area of stagnation for the 1mm case, but a small area of stagnation occurs in the 3mm case in the proximal corner. The area extends along the edge of the stopper from the same location in the 5mm case. The SI shows an increase not only in the area of stagnation, but in the SI on the entire surface as the depth increases.

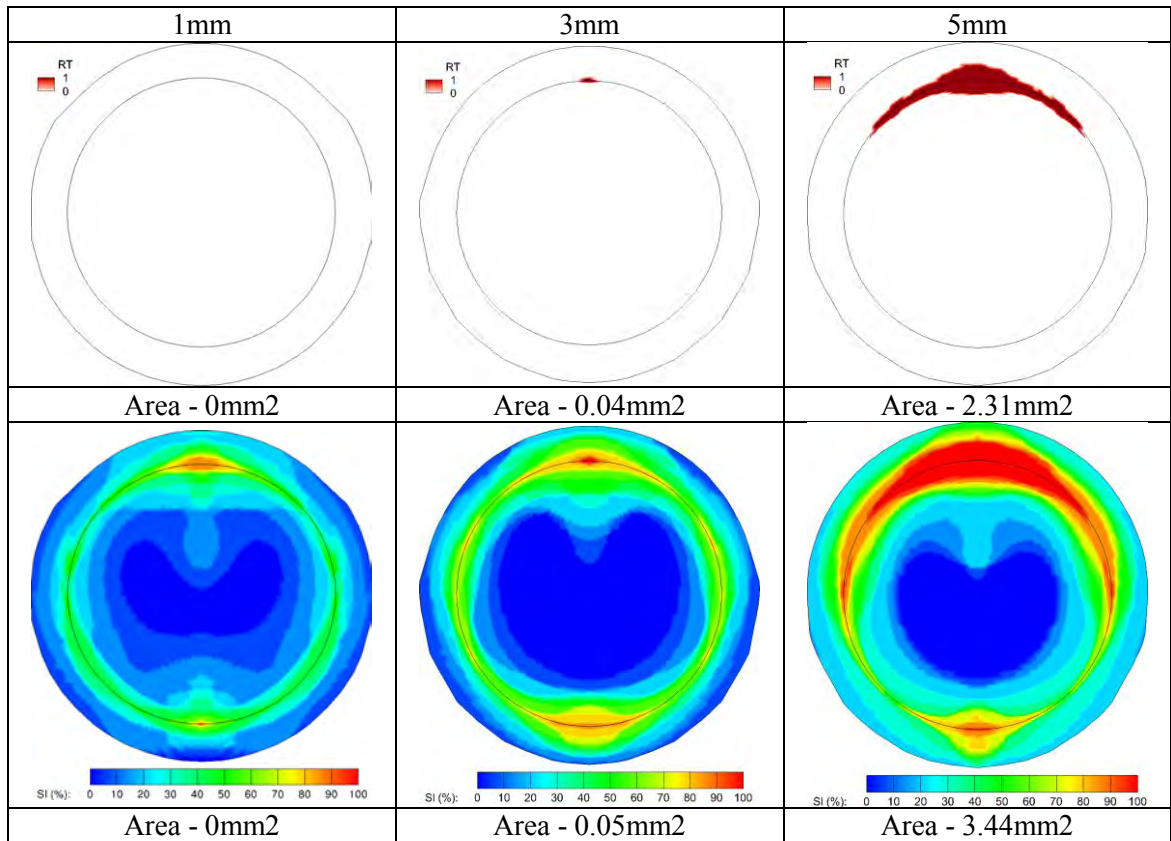


Figure 77. Comparison of the RT ($RT > 1$) and SI on the surface of the cavity for the three cavity depths of 1mm, 3mm, and 5mm for the triphasic wave.

Figure 78 compares the size and location of the area of stagnation, calculated by the SSR, at time steps that cause the smallest area of stagnation in the cycle. The peak flow (01s and 0.15s) results in the smallest area of stagnation in the 5mm case and in the distal corner of the 1mm and 3mm cases. The reverse flow (0.25 and 0.3s) results in the smallest areas of stagnation in the proximal corner of the 1mm and 3mm cases. The plots show how the area of stagnation increases as the depth of the cavity increases at individual time steps.

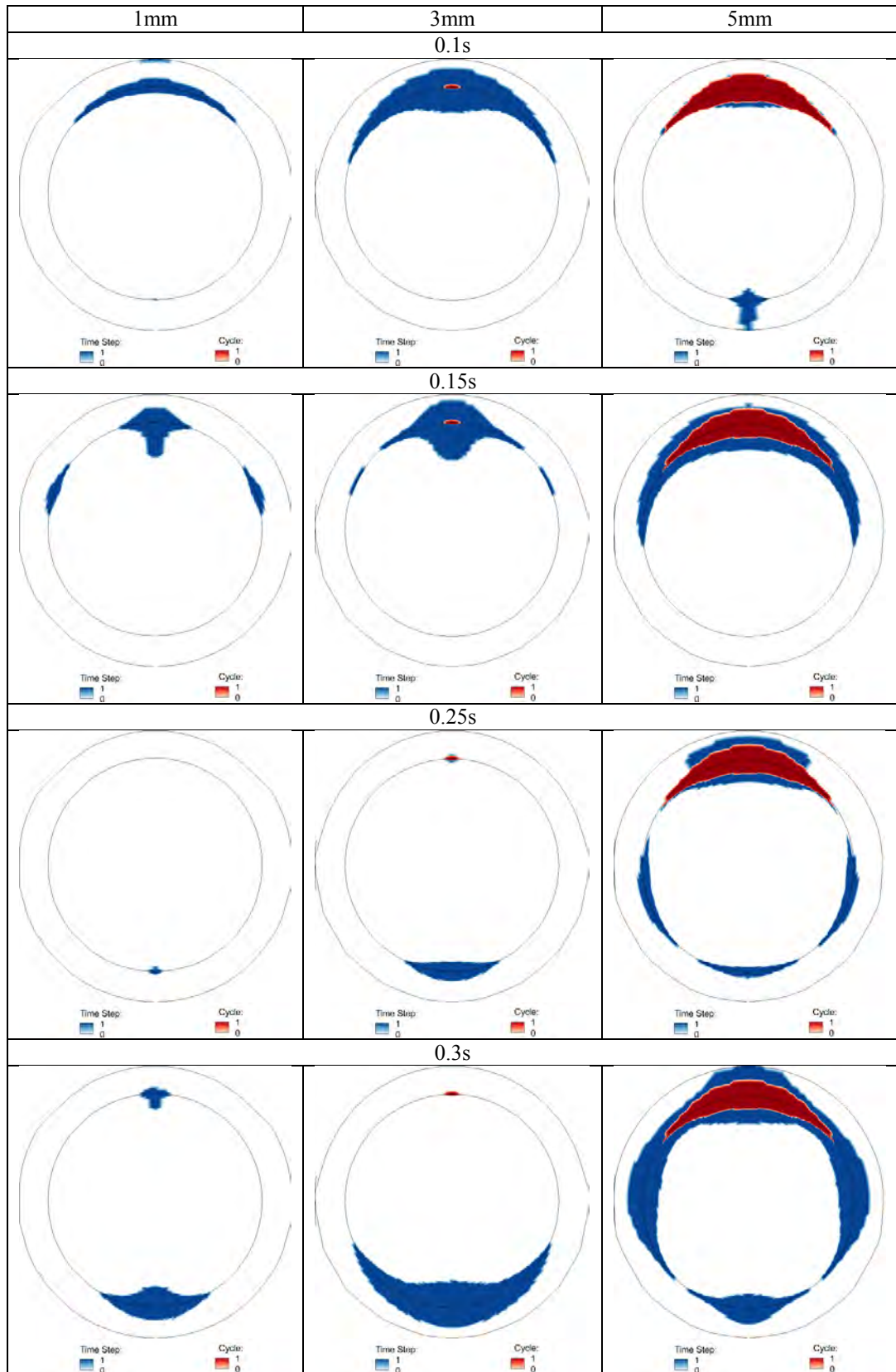


Figure 78. Comparison of the area of stagnation, $SSR < 10s^{-1}$, at 0.1s, 0.15s, 0.25s, and 0.3s for the three cavity depths of 1mm, 3mm, and 5mm for the triphasic wave (Red) and for the entire cycle, $SI=1$ (Blue).

Figure 79 compares the velocity in the cavity at the time steps that cause the smallest area of stagnation in the cycle. The vector plots reveal the effect of the increase in depth on the flow in the cavity. The vector plots show the same result as the other 3 waves; the increase in fluid in the cavity creates larger regions of low velocity fluid near the stopper surface.

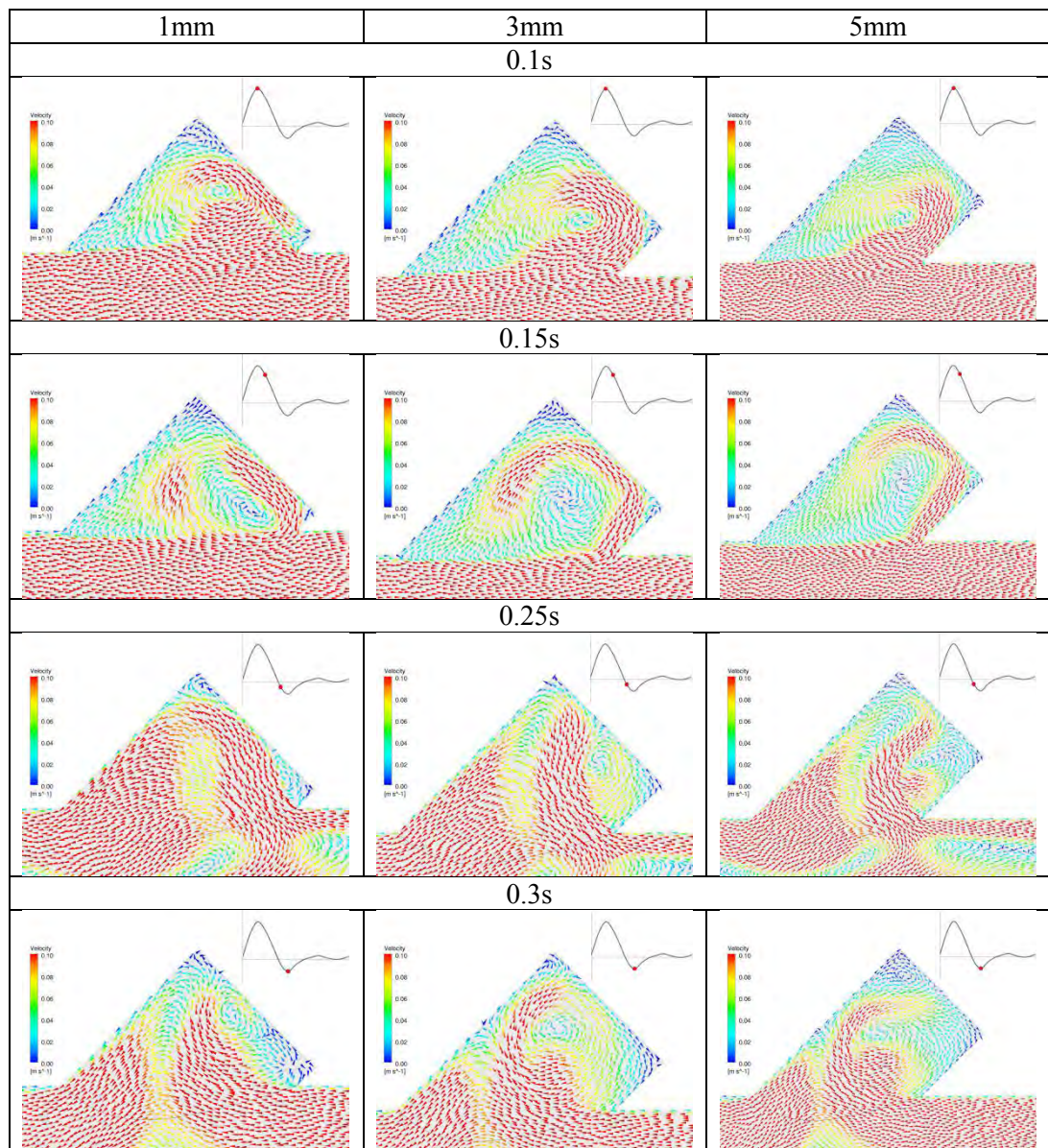


Figure 79. Comparison of the velocity field in the cavity at 0.1s, 0.15s, 0.25s, and 0.3s for the three cavity depths of 1mm, 3mm, and 5mm for the triphasic wave.

All four velocity waves show an increase in the predicted area of stagnation as the depth increases. They exhibit the same pattern between waves with an increase in the area of stagnation as the velocity wave degrades.

5.3 ANGLE

Modifying the angle of the device was expected to provide a greater variation to the flow in the cavity than the other device configurations. The flow conditions in the device were analysed at 45°, 90°, and 135° for each of the four physiological velocity waves. The angle of the device affects not only the flow within the cavity, but also the shape and volume of the cavity itself. The area of stagnation was expected to occur in the deepest section of the cavity, which are the distal corner of the 135° case and either corner for the 90° case.

5.3.1 Blunt Monophasic

The area of stagnation, predicted by RT and SI, for the blunt monophasic wave at the three angles is shown in Figure 80. The size and location of stagnation is substantially different in all three cases. The area of stagnation was located in the proximal corner of the device in the 45° case compared to a very small area in both corners of the 90° case and in both corners, but predominantly in distal corner of the 135° case. The SI shows a much smaller area of stagnation for the 90° case compared to the 45° and 135° cases. The 45° and 135° cases exhibit similar areas of stagnation, but the 135° case shows a higher SI on the rest of the surface.

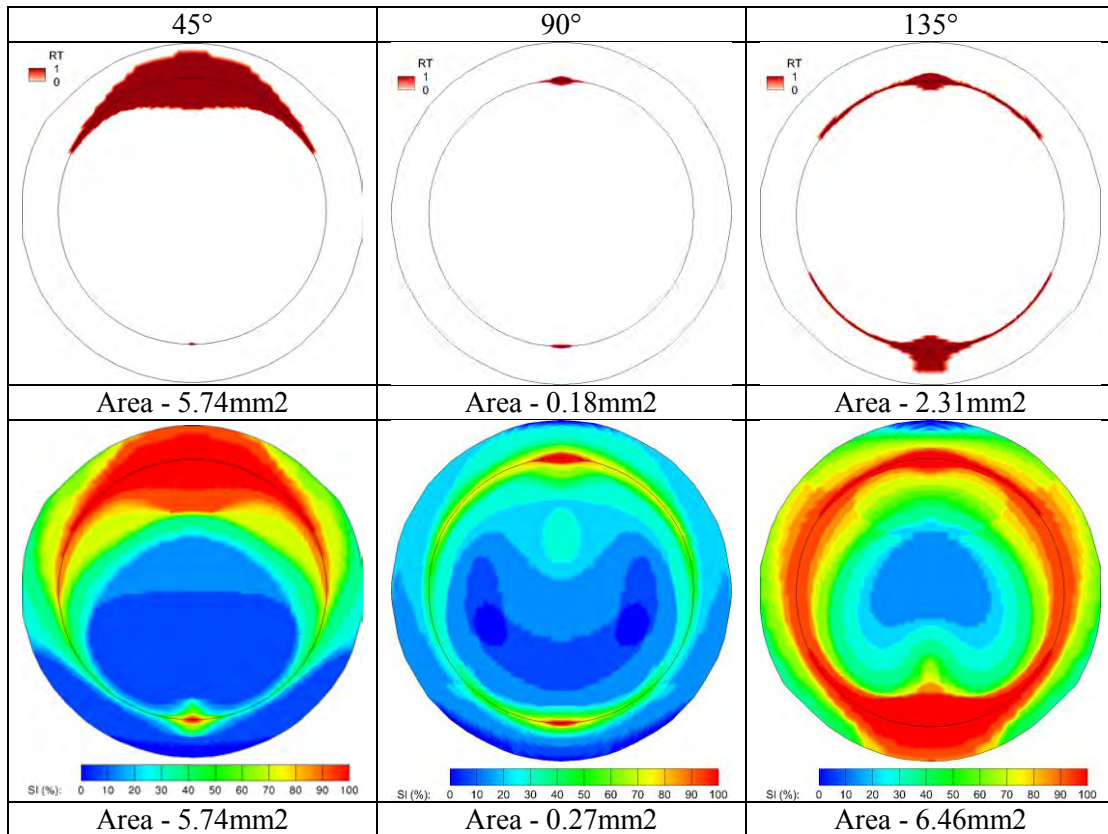


Figure 80. Comparison of the RT ($RT > 1$) and SI on the surface of the cavity for the three device angles of 45°, 90°, and 135° for the blunt monophasic wave.

Figure 81 compares the size and location of the area of stagnation, calculated by the SSR, at time steps that cause the smallest area of stagnation in the cycle. The smallest area of stagnation occurs during peak flow (0.15s) for the 45° and 90° cases, and during acceleration for the 135° case.

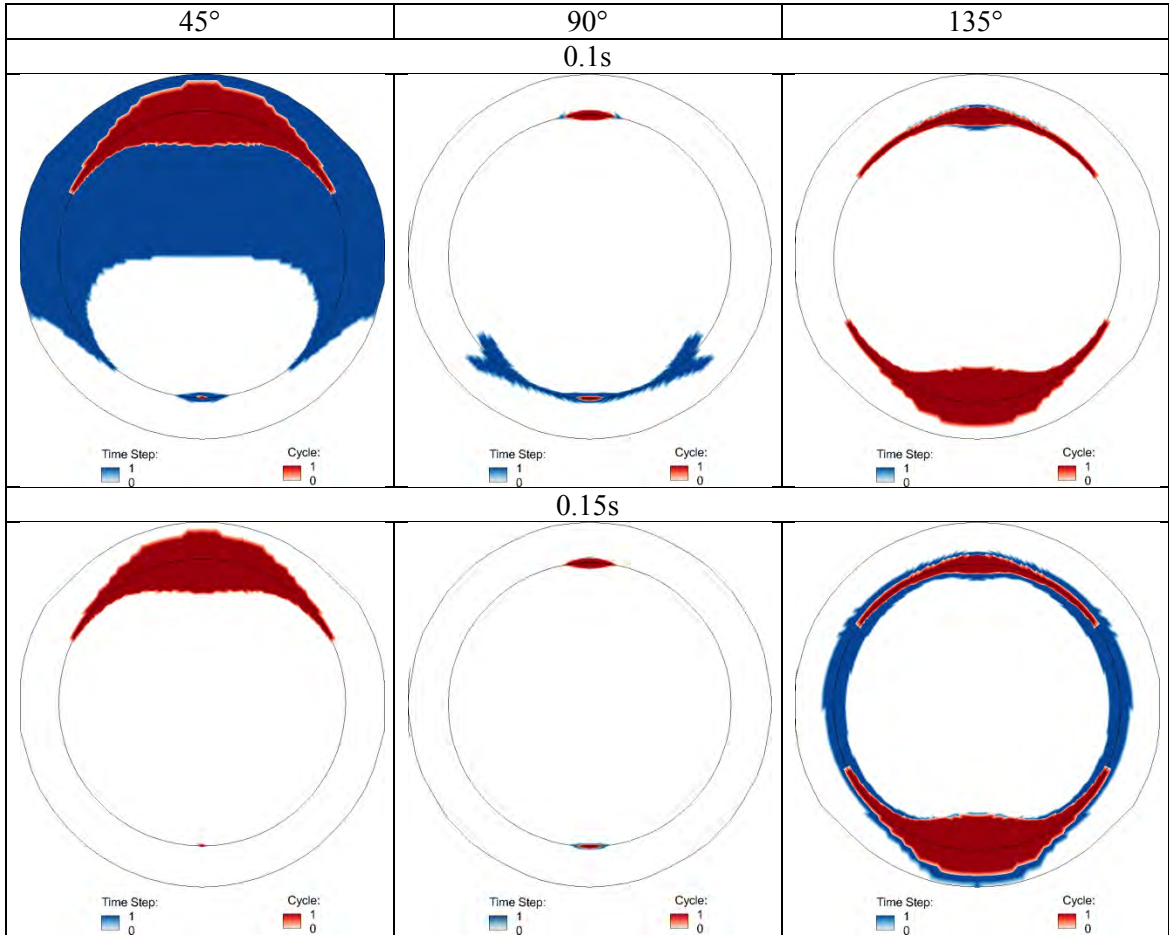


Figure 81. Comparison of the area of stagnation, $SSR < 10s^{-1}$, at 0.1s and 0.15s for the three device angles of 45°, 90°, and 135° for the blunt monophasic wave (Red) and for the entire cycle, SI=1 (Blue).

Figure 82 compares the velocity in the cavity at the time steps that cause the smallest area of stagnation in the cycle. The vector plots show how the flow conditions in the cavity are affected by the angle of the device. The accelerating and peak flow (0.1 and 0.15s) push high velocity fluid into the distal end of the cavity at 90°, resulting in a low velocity recirculation region in the proximal corner. The lack of reverse flow in the blunt monophasic wave leaves the proximal corner of the cavity exposed to low velocities for the entire cycle.

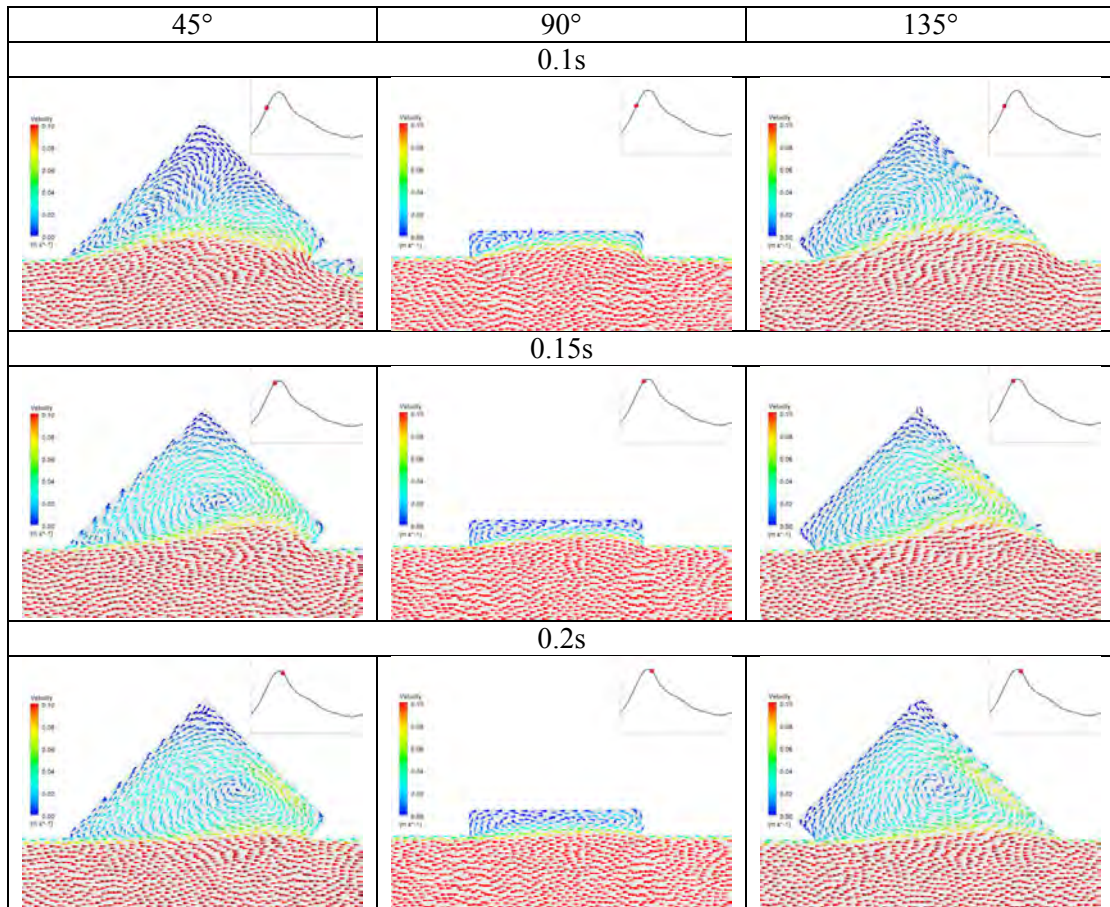


Figure 82. Comparison of the blunt monophasic velocity field in the cavity at 0.1s, 0.15s, and 0.2s for the three device angles of 45°, 90°, and 135°.

The accelerating and peak flow (0.1 and 0.15s) creates high velocity flow that was directed towards the stopper surface in the 45° case, but is directed towards the distal wall of the 135° case. The flow conditions create a vortex that leaves both corners exposed to low velocity flow, but predominantly in the distal corner.

5.3.2 Sharp Monophasic

The area of stagnation, predicted by RT and SI, for the sharp monophasic wave at the three angles is shown in Figure 83. The sharp monophasic wave exhibited similar areas of stagnation in the 45° and 135° cases, but in different locations and the 90° case creates the smallest area of stagnation. The area of stagnation was located in the

proximal corner of the device in both the 45° and 90° cases, but in both corners of the 135° case. The SI shows a much smaller area of stagnation for the 90° case compared to the 45° and 135° cases.

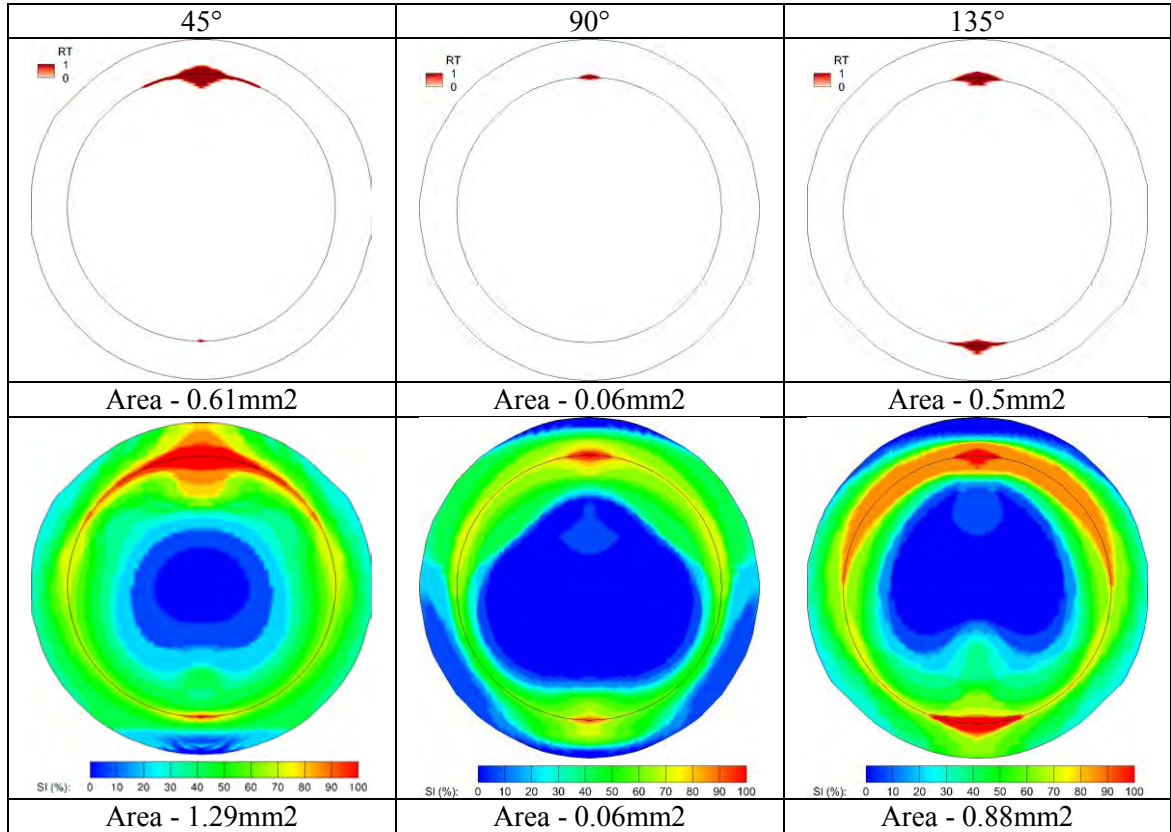


Figure 83. Comparison of the RT (RT>1) and SI on the surface of the cavity for the three device angles of 45°, 90°, and 135° for the sharp monophasic wave.

Figure 84 compares the size and location of the area of stagnation, calculated by the SSR, at time steps that cause the smallest area of stagnation in the cycle. The smallest area of stagnation occurs during peak flow (0.05s and 0.1s) for all three angles. The flow at 0.05s minimises the area of stagnation in the proximal corner for the 90° and 135° cases and the flow at 0.1s minimises the area of stagnation in the 45° case and distal corner of the 90° and 135° cases.

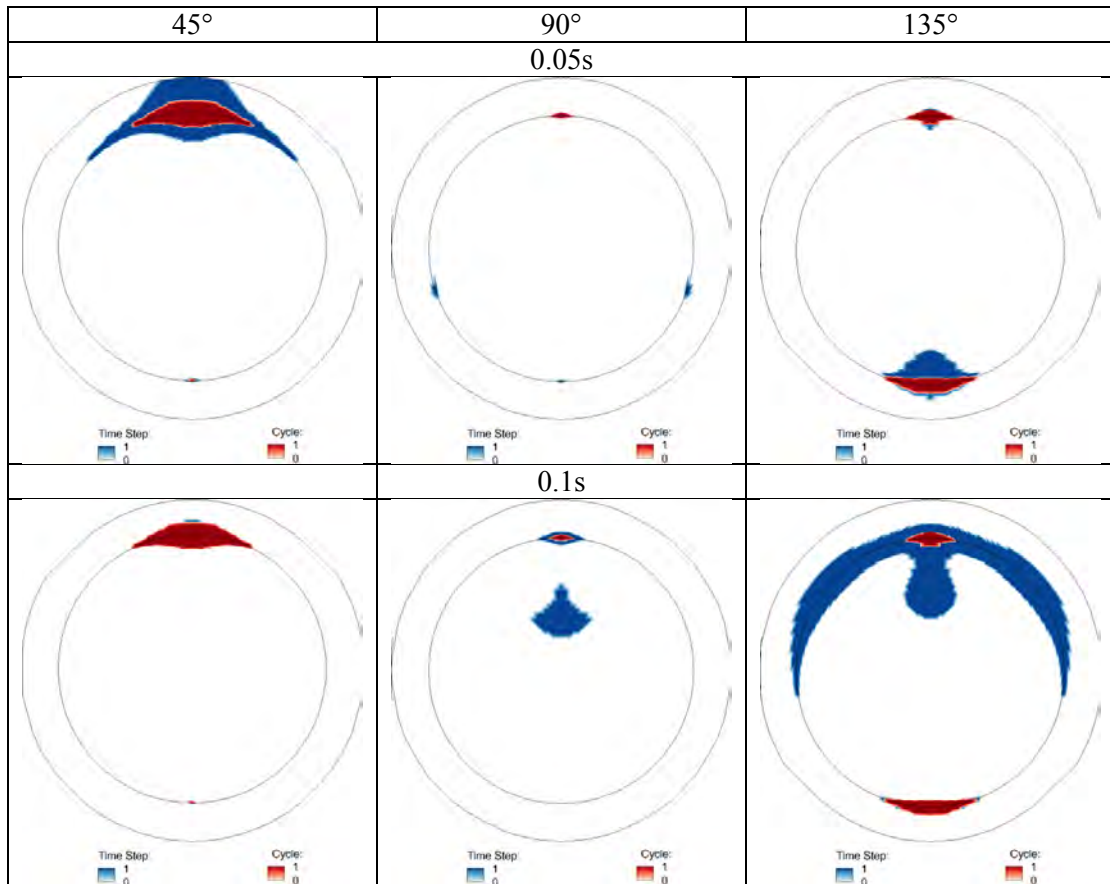


Figure 84. Comparison of the area of stagnation, $SSR < 10s^{-1}$, at 0.05s and 0.1s for the three device angles of 45°, 90°, and 135° for the sharp monophasic wave (Red) and for the entire cycle, $SI=1$ (Blue).

Figure 85 compares the velocity in the cavity at the time steps that cause the smallest area of stagnation in the cycle. The vector plots show how the flow conditions in the cavity are affected by the angle of the device. The peak flow (0.05 and 0.1s) push high velocity fluid into the distal end of the cavity at 90°, which eliminates stagnation there, but leaves a low velocity recirculation region in the proximal corner. The lack of reverse flow in the sharp monophasic wave leaves the proximal corner of the cavity exposed to low velocities for the entire cycle.

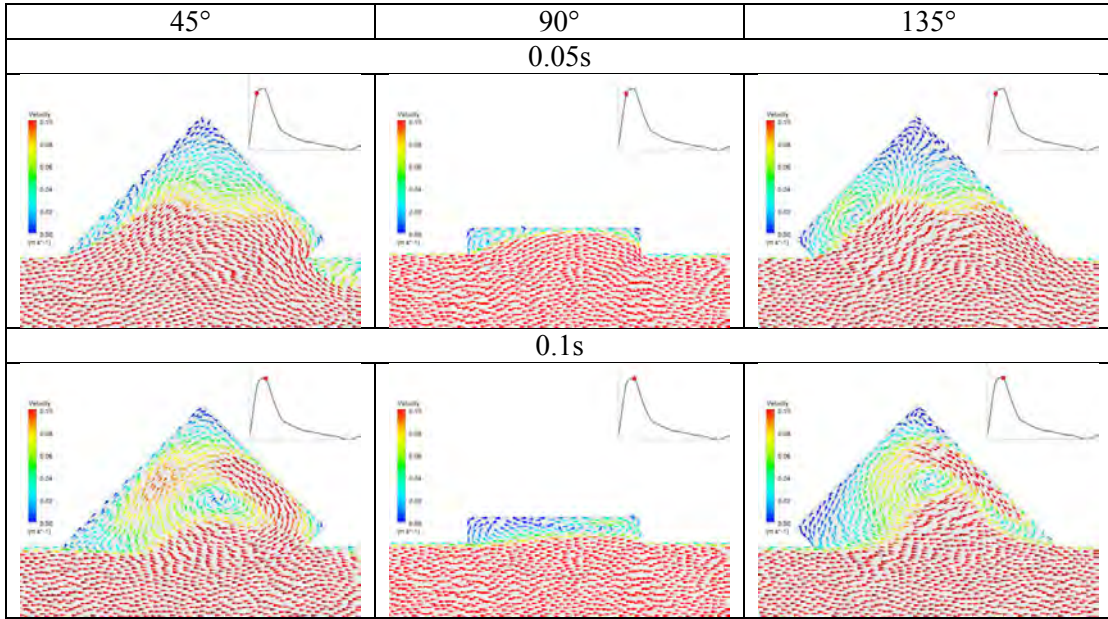


Figure 85. Comparison of the sharp monophasic velocity field in the cavity at 0.05s and 0.1s for the three device angles of 45°, 90°, and 135°.

The peak flow (0.05 and 0.1s) creates high velocity flow that was directed towards the stopper surface in the 45° case, but is directed towards the distal wall of the 135° case. The flow at 0.05s causes a large low velocity region to develop in the distal corner and a smaller region in the proximal corner. The flow at 0.1s creates high velocity flow closer to the distal corner and a large region in the proximal corner.

5.3.3 Biphasic

The area of stagnation, predicted by RT and SI, for the biphasic wave at the three angles is shown in Figure 86. The biphasic wave exhibited similar areas of stagnation in the 45° and 135° cases, and no area of stagnation in the 90° case. The area of stagnation was located in the proximal corner of the 45° case and both corners of the 135° case. The SI shows similar areas of stagnation for the 45° and 90° cases, and an extension along the edge of the stopper for the 135° case. The 45° and 135° cases exhibit similar areas of stagnation, but the 135° case shows a higher SI on the rest of the surface.

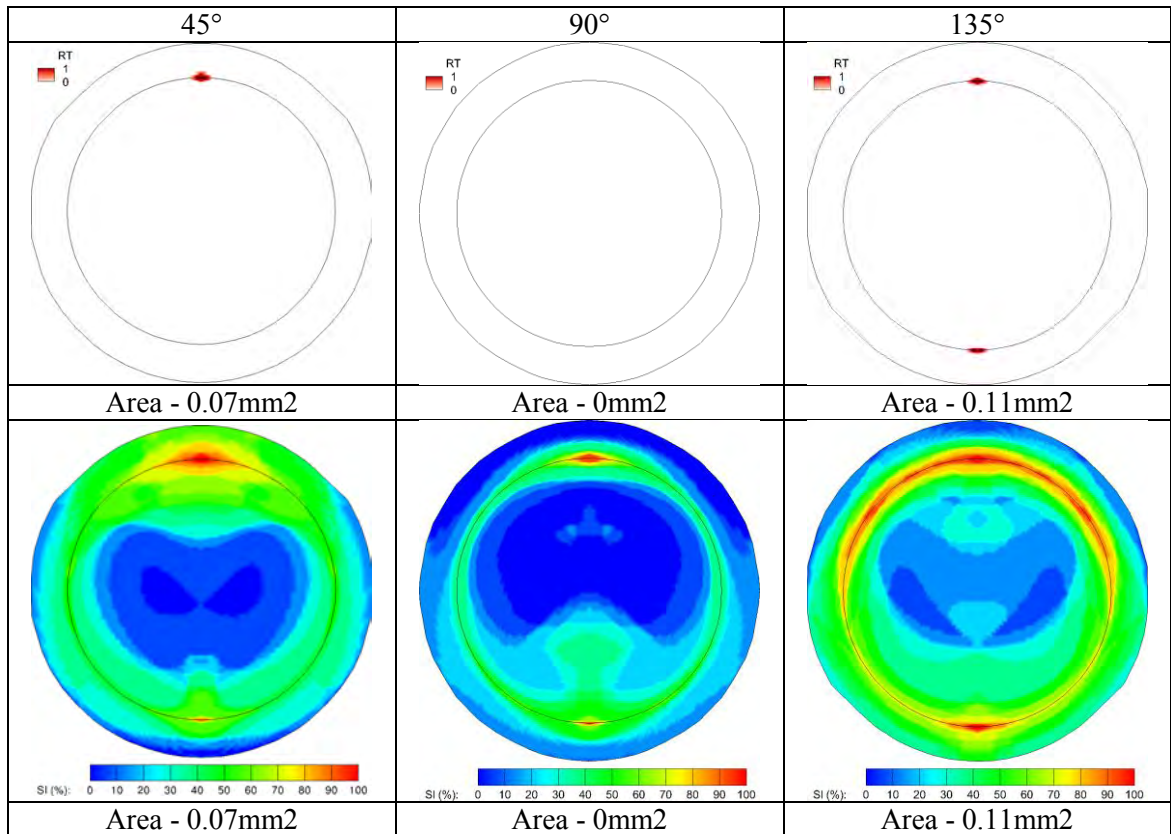


Figure 86. Comparison of the RT (RT>1) and SI on the surface of the cavity for the three device angles of 45°, 90°, and 135° for the biphasic wave.

Figure 87 compares the size and location of the area of stagnation, calculated by the SSR, at time steps that cause the smallest area of stagnation in the cycle. The accelerating flow (0.05s) eliminates stagnation on the proximal corner of the 90° case and minimises it for the 135° case. The peak flow (0.1s) eliminates stagnation on the distal corner of the 45° and 90° cases. The smallest area of stagnation in the proximal corner of the 45° case occurs at 0.15s and the distal corner of the 135° case at 0.2s.

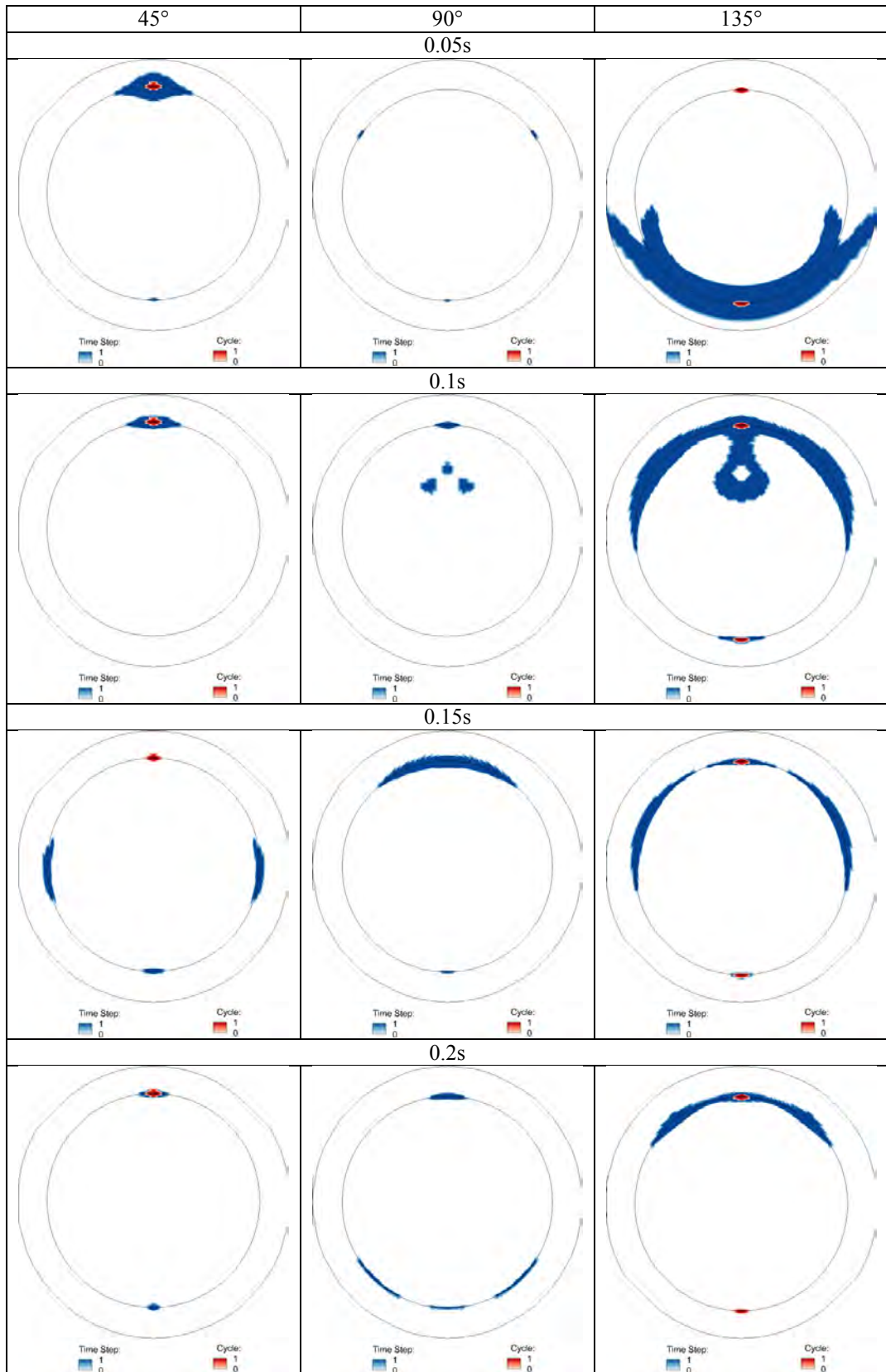


Figure 87. Comparison of the area of stagnation, $SSR < 10s^{-1}$, at 0.05s, 0.1s, 0.15s and 0.2s for the three device angles of 45°, 90°, and 135° for the biphasic wave (Red) and for the entire cycle, SI=1 (Blue).

Figure 88 compares the velocity in the cavity at the time steps that cause the smallest area of stagnation in the cycle. The vector plots show how the flow conditions in the cavity are affected by the angle of the device. The accelerating and peak flow (0.05 and 0.1s) push high velocity fluid into the distal end of the cavity at 90° , resulting in a low velocity recirculation region in the proximal corner; however, the reverse flow of the biphasic wave exposes the proximal corner to high velocity flow, eliminating stagnation from the cavity completely.

The accelerating and peak flow (0.05s and 0.1s) creates similar flow conditions in the 45° and 135° case, but low velocity regions in opposite corners of the cavity. The forward flow is better suited at removing stagnation in the distal corner of the 45° case than the 135° case. The reverse flow provides the ideal opportunity to remove stagnation from the proximal corner, but was not as effective as the forward flow.

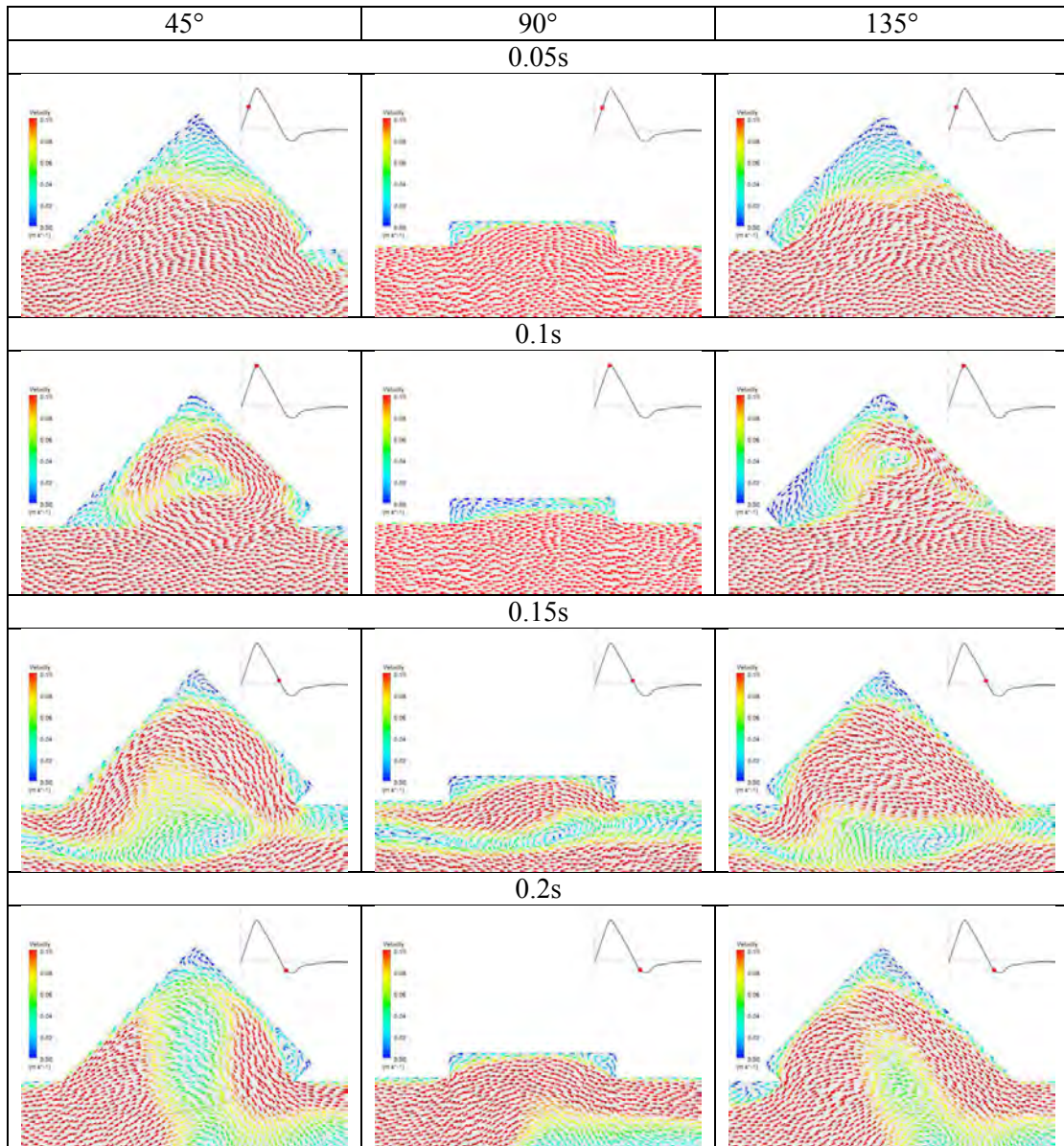


Figure 88. Comparison of the biphasic velocity field in the cavity at 0.05s, 0.1s, 0.15s and 0.2s for the three device angles of 45°, 90°, and 135°.

5.3.4 Triphasic

The area of stagnation, predicted by RT and SI, for the triphasic wave at the three angles is shown in Figure 89. No area of stagnation was predicted in the 45° case and was almost completely removed in the 90° and 135° cases. The area of stagnation was

located in the proximal corner of the device in the 90° and 135° cases. The SI shows similar shear conditions on surface of the cavity for all three cases.

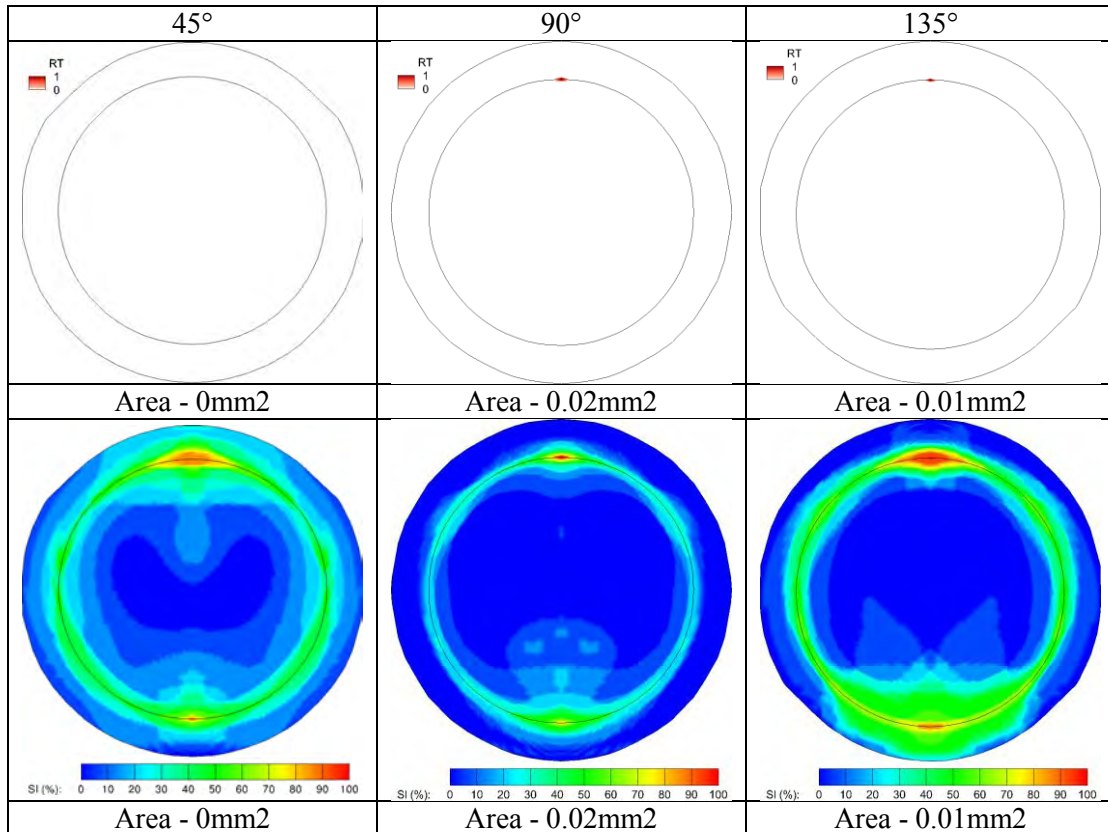


Figure 89. Comparison of the RT ($RT > 1$) and SI on the surface of the cavity for the three device angles of 45°, 90°, and 135° for the triphasic wave.

Figure 90 compares the size and location of the area of stagnation, calculated by the SSR, at time steps that cause the smallest area of stagnation in the cycle. The change in direction of flow (0.25s) results in the smallest area of stagnation for the 90° and 135° cases in both corners and the proximal corner of the 45° case. The forward flow (0.15s) removes the stagnation in the distal corner for the 45° case.

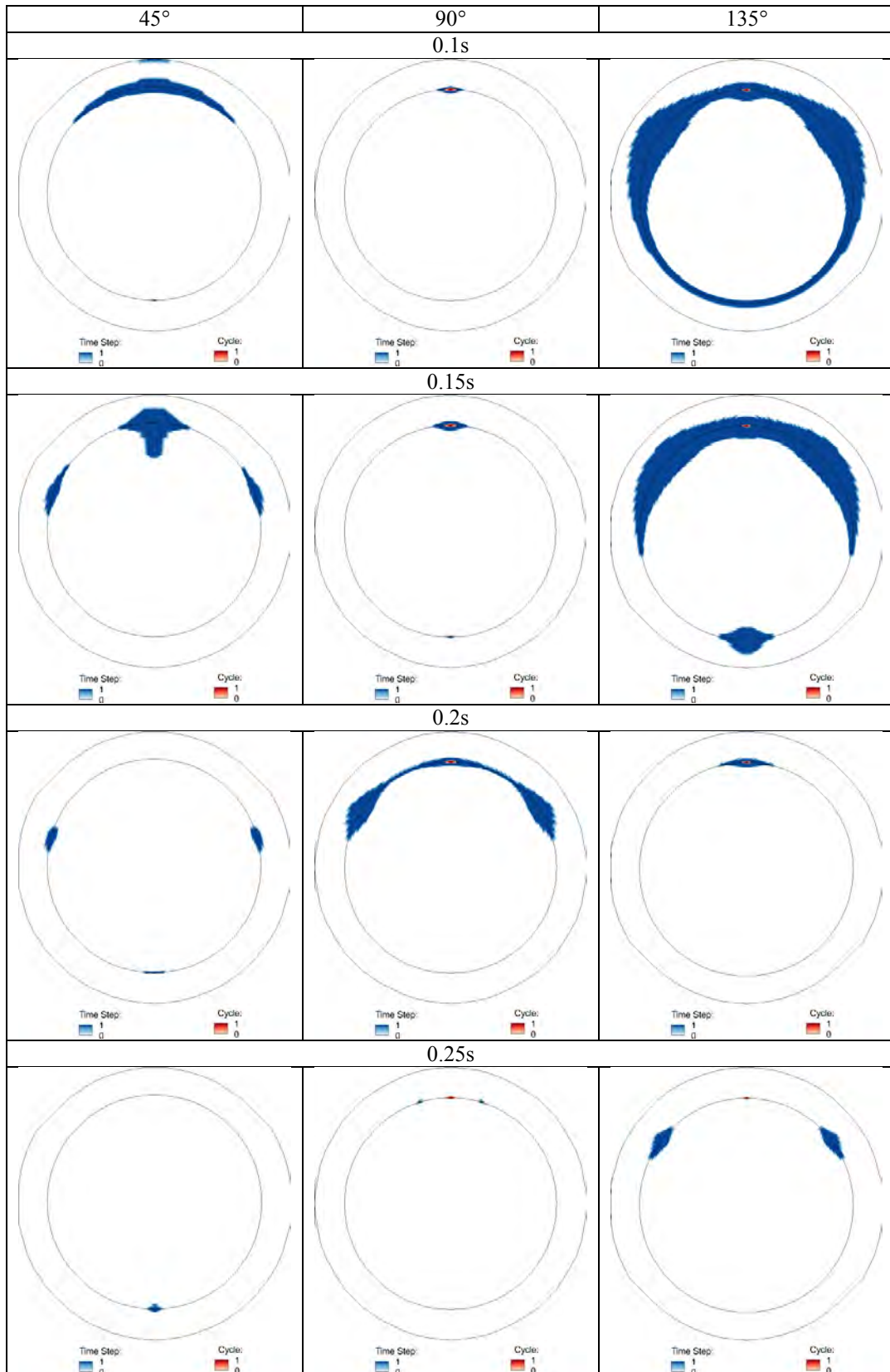


Figure 90. Comparison of the area of stagnation, $SSR < 10s^{-1}$, at 0.1s, 0.15s, 0.2s, and 0.25s for the three device angles of 45°, 90°, and 135° for the triphasic wave (Red) and for the entire cycle, $SI=1$ (Blue).

Figure 91 compares the velocity in the cavity at the time steps that cause the smallest area of stagnation in the cycle. The vector plots show how the flow conditions in the cavity are affected by the angle of the device. The forward flow (0.1 and 0.15s) push high velocity fluid into the distal end of the cavity at 90°, resulting in a low velocity recirculation region in the proximal corner; however, the reverse flow of the triphasic wave exposes the proximal corner to high velocity flow, almost completely removing stagnation from the proximal corner.

The peak flow (0.1s) creates similar flow conditions in the 45° and 135° case, but a much larger low velocity region in the proximal corner of the cavity. The forward flow is better suited at removing stagnation in the distal corner of the 45° case than the 135° case. The reverse flow of the triphasic velocity wave was more effective at removing stagnation in the distal cavity than forward flow.

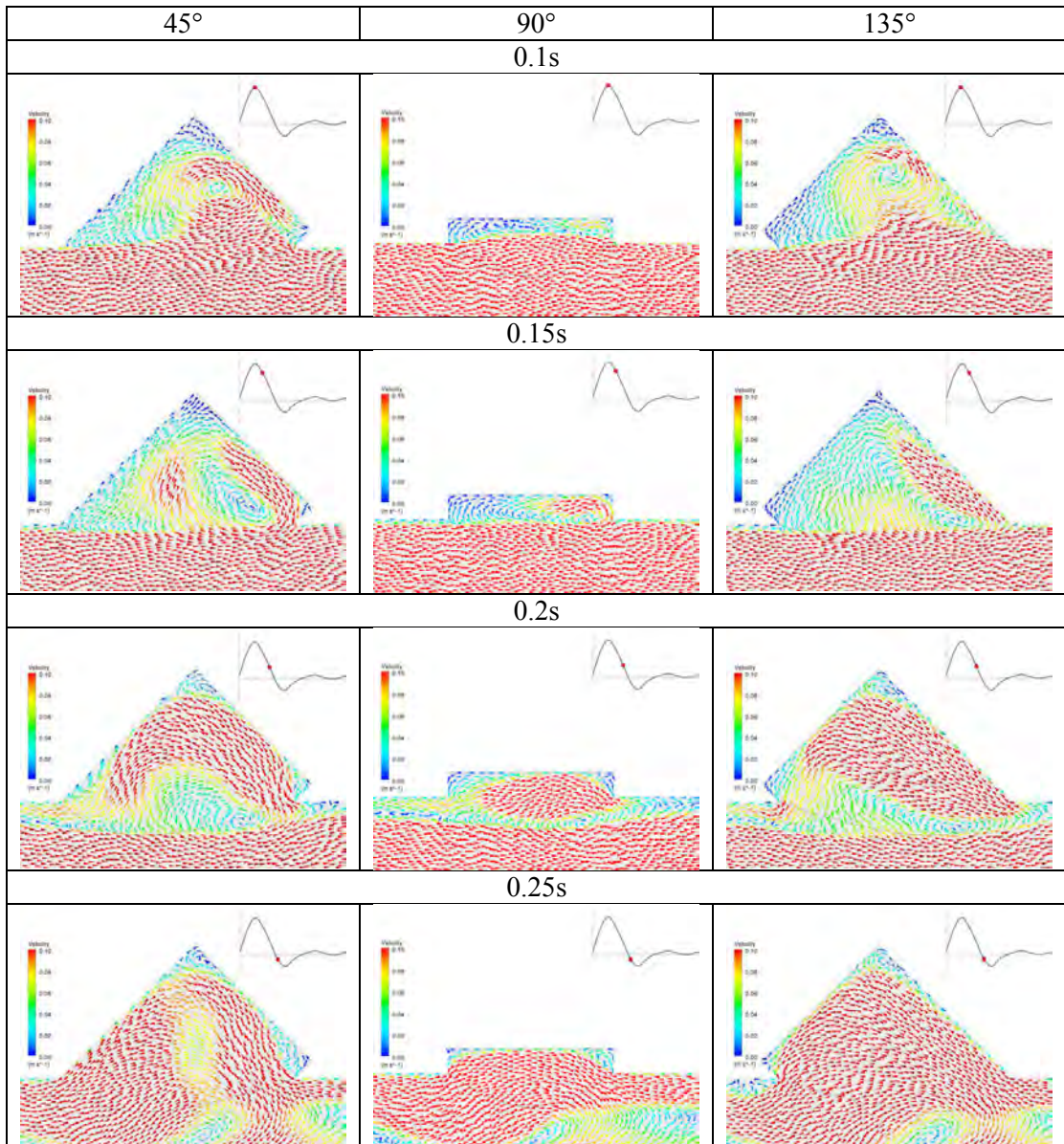


Figure 91. Comparison of the triphasic velocity field in the cavity at 0.1s, 0.15s, 0.2s, and 0.25s for the three device angles of 45°, 90°, and 135°.

5.4 ANGLE + DEPTH

The different device angles produce considerable changes to the flow conditions in the cavity of the device. The depth of the cavity has also been shown to allow the flow in the cavity to develop further into the cavities, but ultimately results in more stagnation

on the surface of the stopper. The angle of the device and depth of the cavity were analysed together to determine if an increase in the depth resulted in similar detrimental flow conditions for the different angles.

Figure 92 compares the area of stagnation, calculated from the RT, for each case. The results are consistent with the initial findings that the area of stagnation increase as the integrity of the velocity wave degrades. It is also shown that the area of stagnation increases for all cases as the depth is increased. Lastly the different angles provide vastly different flow conditions in the cavity and can be used to determine the optimal device position for each physiological wave.

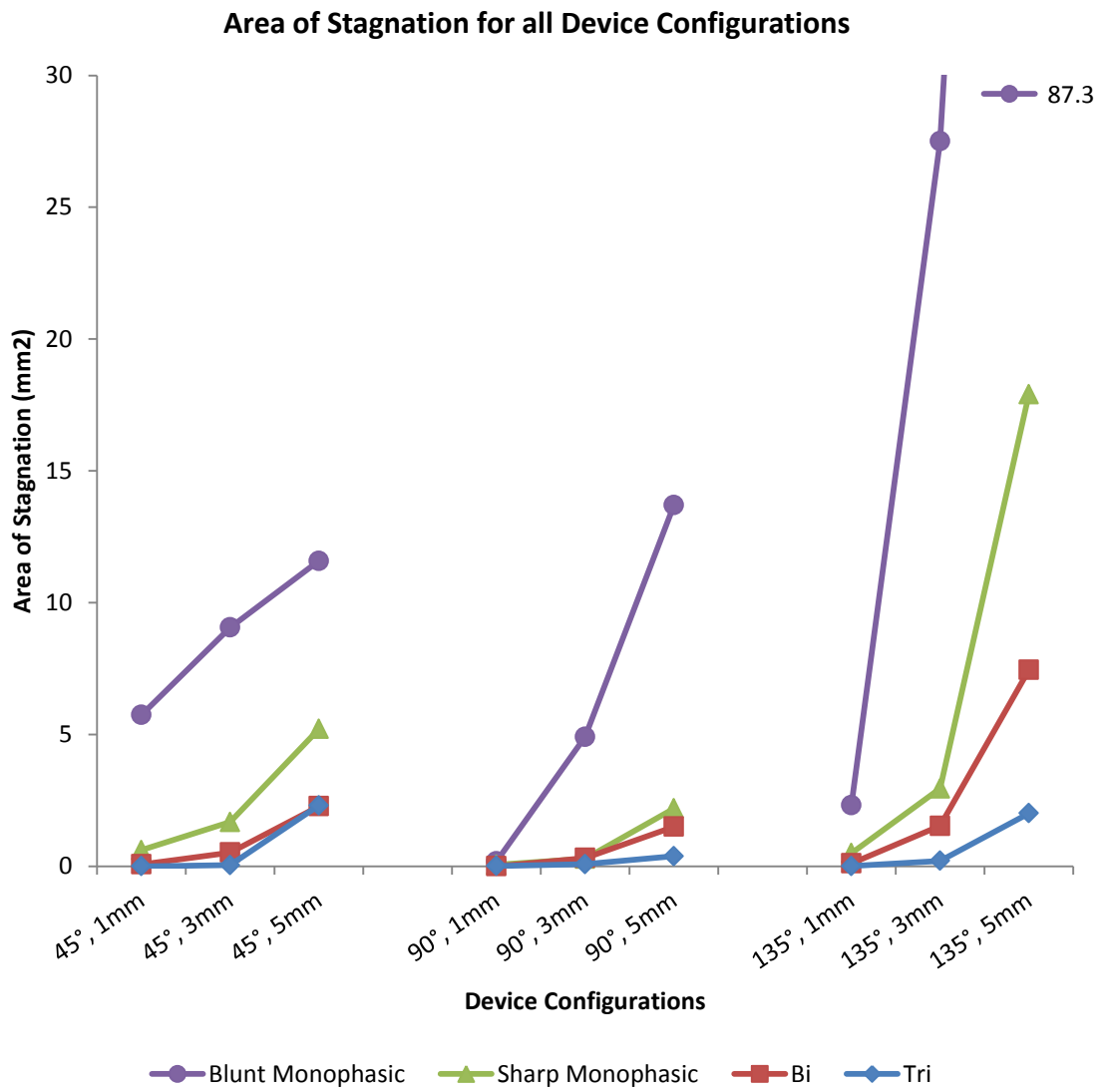


Figure 92. Comparison of the area of stagnation for all of the device configurations.

CHAPTER 6 - DISCUSSION

6.1 STAGNATION

A number of different techniques have been used to locate and predict stagnation. Stagnation in arterial blood flow is usually found at complicated or abnormal geometries and poses a catastrophic risk to the cardiovascular system. Stagnation is found in abnormal flow conditions which can result from branching vessels, stenoses, aneurysms or implanted devices. Stagnation defines a volume of fluid that remains at a fixed location for a prolonged period of time. In the cavity of the extracorporeal access device the corners provide the ideal location for slow flow that remains trapped for an extended period of time.

The techniques used to measure, locate and predict stagnation highlight the importance of understanding and avoiding abnormal flow conditions, especially in device design. Stagnation has previously been measured using velocity [45], WSS [34, 35, 39, 62], SSR [34, 35, 63, 86], OSI [39, 116] and RT [39, 62, 63, 116, 117]. Thresholds were used in these studies for the velocity, WSS and SSR and locations below the threshold value for an extended period of time indicates stagnation and presents a risk of thrombosis. In this thesis, the SSR, OSI and RT were used to identify regions of stagnation. (For a detailed analysis of each measure, see Chapter 1.2).

RT has evolved as the most accurate marker for stagnation and can be determined computationally via particle tracking [62] or calculated from the mechanical properties

of the flow [39]. RT has been used in conjunction with low WSS to provide a better prediction of thrombus formation than both measures alone [62]. This technique was used to identify regions of stagnation in the cavity of the computational model, which were compared to the explanted devices.

The velocity of the fluid was used by Rayz et al [45] to predict areas of stagnation and ultimately thrombus formation. In the vector plots for the triphasic velocity profile, regions of low velocity, less than 0.02m/s, in the corner of the cavity correspond with areas of stagnation measured in the SI and RT plots, and the location of thrombus initiation in the explanted devices. The low velocity regions in the vector plots increase as the number of phases decreases and correspond with an increase in the area of stagnation in the RT plots; however, the size of the low velocity regions are much larger than the area of stagnation. The velocity threshold provides an indication of low velocity flow, but does not account for the direction of the flow. Low velocity fluid in a uniform direction has the potential to move fluid away from the location and avoid stagnation. These results would explain the lack of research that employs a velocity threshold for stagnation.

The WSS and SSR have been used extensively to identify regions of stagnation [34, 35, 39, 62, 63, 86]. In most cases, the initiation of thrombosis occurs on the wall, and the WSS can be used to identify how the fluid behaves close to the wall in areas of stagnation. The SSR is a measure of deformation acting on the fluid and provides a better indication of the forces on the fluid than just the wall. The SSR also provides a more uniform threshold for thrombosis, regardless of the viscosity model. Corbett et al. [34] compared Newtonian and non-Newtonian flow and found thrombus formation

occurred below WSS thresholds of 41Pa and 17Pa respectively and below a SSR threshold of approximately 50s^{-1} .

The WSS and SSR can be used to show the percentage of the cycle the surface is below the threshold value (SI) [34]; however, when compared to the RT they reveal the same limitation as the velocity, i.e. direction of the flow is not considered.. The SI identifies flow at risk of stagnation and shows an increase in the area of stagnation as the number of phases decreases, but it is larger than the area of stagnation calculated from the RT. The vector plots reveal that the difference between the SI and the RT plots are regions of flow in a uniform direction, confirming the flow is not restricted to a location.

The OSI has been used to identify regions of disturbed flow conditions in various situations, including aneurysms, stenosis, and atherosclerosis. The OSI measures the cyclic nature of the flow near a surface and has been used in combination with other markers such as low WSS to predict regions of stagnation. The OSI is only useful as an indicator of the oscillatory nature of the flow and a high OSI indicates a location that experiences the same reverse and forward flow for a period of time. Unfortunately there has been no threshold determined to identify a high OSI. Also the OSI does not account for the magnitude of the flow and a region exposed to larger forward and reverse flow during the period would not be considered stagnant. Similarly regions of very low velocity in a uniform direction may be considered stagnant.

The vector plots provide the opportunity to investigate how the flow in the cavity and low velocity regions are affected by individual aspects of the velocity waves. The SSR quantifies the impact of individual aspects of the velocity wave on stagnation in the

cavity. The SI provides an indication of the surface exposed to low velocity fluid at risk of stagnation and the OSI can identify regions of cyclic flow, where fluid remains trapped. All of these markers can be used to support the area of stagnation calculated from the RT.

RT was developed to overcome the sensitivity of the OSI and includes the time averaged wall shear stress magnitude to determine the time a theoretical particle would remain at a location. High RT indicates flow that stays at the same location for a prolonged time and is inversely proportional to the distance the fluid moves. Locations with a low average WSS and high OSI indicate a region of fluid that does not deviate from the location.

Residence time was employed in to determine if RT was a good predictor of thrombus formation in aneurysms [117] and near stents [62]. Both studies revealed the RT was a good marker for predicting regions of flow that result in thrombus formation. Unfortunately, even the RT is sensitive to the magnitude of the WSS. A point on the wall for sinusoidal flow will provide high RT due to the high OSI and average WSS, but may experience large velocities and movement throughout the cycle and avoid stagnation.

The RT was combined with low WSS and reported better results than both markers alone in a study that measured the residence time of blood in an intracranial aneurysm [62]. Low WSS in combination with RT highlights regions of flow exposed to low velocities, low shear forces, and remains at the same location; the ideal marker for stagnation.

6.2 PHYSIOLOGICAL FACTORS

RT has been applied to determine its usefulness as a predictor for thrombus formation [117], but has not been used to assess the effect of different physiological conditions on stagnation. RT was used to determine the effect of retrograde flow on stagnation and the risk of thrombosis in an extracorporeal access device.

6.2.1 Physiological Velocity Waves

The hyper perfusion treatment was developed for patients with extensive peripheral arterial disease and the success of the device depends on the arterial environment. Peripheral arterial disease causes severe occlusions in the arteries of the leg and a lack of circulation to the lower limb. The treatment is used as a last resort before amputation of the leg and the femoral artery provides the best access to deliver the treatment. The access device is implanted in the femoral artery to provide access to restore the lower limb; however the extensive nature of the disease in these patients suggest occlusions may be present upstream of the femoral artery.

The four physiological waves (triphasic, biphasic, sharp monophasic, and blunt monophasic) identified by Spronk et al. [28] and O'Neill[29] were used to determine the effect of the different pulsatile flow conditions and retrograde flow on the likelihood of thrombus formation. The patients that received the extracorporeal access device all had extensive peripheral arterial disease, which would indicate that a monophasic wave is the most likely to be found in the femoral artery; however, the extent of the disease proximal to the femoral artery is unknown and any of these velocity waves may be present and could affect the success of the device.

The triphasic, biphasic, and sharp monophasic waves can be considered as a progression of the severity of occlusion upstream. The triphasic velocity wave represents a healthy femoral wave which can also exist in an occluded vessel. The biphasic wave represents an increase in the severity of the occlusion upstream, which degrades the integrity of the wave and the loss of the second phase of forward flow. The sharp monophasic wave represents another increase in the severity of the upstream occlusion and the absence of any phase change and retrograde flow. The three waves all approach zero velocity at the end of the cycle and the duration of low velocity flow increases as the number of phases decreases. The blunt monophasic wave is considerably different to the other three waves and represents the most severe occlusion upstream of the vessel. The wave provides continuous forward flow with slow acceleration and deceleration between peak and trough flow and never approaches zero velocity throughout the cycle.

The four physiological waves were expected to provide different flow conditions in the cavity that lead to different degrees of stagnation. The thrombosis in the explanted devices was a result of stagnant fluid in the cavity. The first phase of the triphasic, biphasic and sharp monophasic velocity waves were expected to provide similar flow conditions within the cavity. The low velocity time steps at the end of the three waves are expected to promote stagnation within the cavity. The retrograde flow in the triphasic and biphasic waves in combination with jetting flow from through the stenosis was expected to provide flow conditions that would flush out the cavity. The blunt monophasic velocity wave was expected to isolate the flow in the cavity for the entire cycle due to the continuous flow and slow acceleration and deceleration. Despite being the most likely wave in the femoral artery of the patients receiving the treatment, the

blunt monophasic velocity wave was expected to provide flow conditions in the cavity that promote thrombus formation.

6.2.1.1 Vector Plots

The velocity field in the cavity of the device was described using vector plots on the mid-plane throughout the cycle. The vector plots were used to analyse the behaviour of the blood near the stopper surface of the cavity. The velocity field provides an indication of the flow conditions in the cavity at specific time steps in the cardiac cycle. The results are effective for identifying regions of low velocity fluid throughout the cycle, but were unable to quantify the size of the stagnation. They have the advantage of showing how the flow in the cavity is affected by individual aspects of the velocity wave as well as a summary of the performance of the device over the entire cycle. The vector plots are able to show not only low velocity regions in the cavity but also the flow of the fluid and whether it oscillates and remains trapped or moves on from the same location.

The results in Chapter 4 indicate that the triphasic, biphasic and sharp monophasic cases exhibit a progression in the likelihood of thrombus formation as the velocity wave degrades. These cases were analysed together as they share similar traits in the velocity profile and the blunt monophasic case will be examined as a special case. The first phase of the triphasic, biphasic and sharp monophasic waves provide similar flow conditions in the cavity, but the different velocities and accelerations cause a difference in the penetration of the flow into the corners of the cavity where thrombus is likely to initiate. The low velocity time steps at the end of the cardiac cycle in all three cases correspond to low velocity vectors throughout the entire cavity.

The accelerating flow in the first phase causes high velocities at the entrance of the cavity and on the distal end of the stopper surface. The peak forward flow causes isolation of the flow in the cavity, but the high velocity in the main vessel creates a high velocity vortex in the cavity that generates high velocities on the middle of the stopper surface and proximal wall. Both the accelerating flow and the peak flow wash out the most fluid in the distal corner than any other time step in the cycle, but also leave a small region of stagnation in the proximal corner.

The decelerating flow maintains the isolated flow in the cavity and causes high velocity flow on the middle of the stopper surface and proximal wall. These characteristics of the velocity waves wash out a large portion of the surface of the cavity, but still leave a region of stagnant fluid in the proximal corner of the cavity.

Vector plots reveal the same flow conditions in the first phase for the three waves and show a strong tendency for a reduction in stagnation in the corners. In the first phase of these waves the peak flow flushes out the cavity the most and the different velocity and acceleration between the waves affects the size of the stagnation.

At the end of the first phase, before the flow reverses, the flow at the walls changes direction and causes a disruption to the flow conditions in the cavity. The flow reversal of the triphasic and biphasic waves also shows a strong tendency to reduce flow stagnation in the cavity. In the second phase the change in flow direction causes the greatest disturbance, but unlike the first phase, the flow penetrates deeper into the proximal corner with direct flow rather than a vortex.

The reverse flow component of the triphasic and biphasic cases causes the greatest disturbance to flow in the proximal corner of the cavity and highlights the importance of retrograde flow. The flow in the cavity as the velocity wave changes direction, in particular, causes high velocity flow high on the stopper surface and proximal wall. The reverse flow at the change in phase causes high velocity flow right up into the proximal corner and the lowest area of stagnation in this location during the cycle. The absence of reverse flow means the monophasic cases rely on the peak forward flow to wash out the proximal corner as it also causes the most disturbances in the cavity; however, as shown in the vector plots, even the peak forward flow leaves a region of stagnation in this location. The third phase of the triphasic wave causes a change in flow at the wall but the disruption of this forward flow does not affect the cavity as much as the first two phases.

The vector plots in the blunt monophasic wave reveal a completely different set of flow conditions to the other three waves. The blunt wave does not experience the fast acceleration and deceleration of the other waves, which can cause penetration of flow into the cavity. The vector plots show the flow into the cavity for the blunt wave isolated from the main flow in the vessel for the majority of the cycle. The isolated fluid, combined with the lower peak velocity, lower acceleration, and continuous flow enable a situation in which the velocity of the fluid in the cavity is much lower compared to the other cases. In the blunt monophasic case, peak flow provides the greatest opportunity for washing out the cavity. The velocity of the fluid is considerably lower than the other waves and the proximal third of the stopper surface experiences low velocity flow for the duration of the cycle.

All of the vector plots show agreement with the explanted access devices. The low velocity regions suggest the thrombosis initiates in the proximal corner of the cavity for all waves. The degree of stagnation increases as the integrity of the wave decreases, which may explain the difference in thrombus progression in the explanted devices.

6.2.1.2 SSR

The velocity field provides an indication of the flow in the cavity but is unable to quantify the stagnation. The SSR threshold has been established as a marker for stagnation and was used to quantify the effect of individual aspects of the physiological velocity profile on the stagnation measured in the entire cavity. The area of stagnation was calculated on the surface of the cavity for locations below the threshold. The results were compared against the velocity to determine which aspects of the velocity wave caused the greatest reduction in stagnation.

The triphasic, biphasic, and sharp monophasic waves show similar trends in the first phase with different areas of stagnation occurring as a result of the difference in velocity and acceleration. The blunt wave shows a much larger area of stagnation throughout the cycle with the peak flow contributing the greatest reduction in stagnation. The graphs confirm that the smallest areas of stagnation occur during peak flow for the monophasic cases and between peak flow and reverse flow for the triphasic and biphasic cases. The graphs confirm the observations made from the vector plots that the peak flow in the first phase and the change in flow direction in the second phase cause the greatest disturbance to flow in the cavity.

The sharp and blunt monophasic waves show evidence of correlation between area of stagnation and velocity of the main flow. The Spearman ranked correlation coefficient was used to determine if a relationship exists between the area of stagnation and the velocity of the physiological velocity waves. The results show that the velocity and acceleration are correlated to the area of stagnation in the cavity for all of the physiological waves. This indicates that as the velocity and acceleration increase, the area of stagnation decreases. The difference in velocity and acceleration between waves during similar flow conditions accounts for some of the variation in area of stagnation.

6.2.1.3 Area of Stagnation

The vector plots reveal the flow conditions that lead to stagnation, and the SSR quantifies the size of the area of stagnation, but the SI can be used to show the location of stagnation on the surface of the cavity. The SI shows the percentage of the cycle a location is below the SSR threshold and an SI of 1 indicates a region of stagnation for the entire cycle. The SI confirms the location of consistently low velocity flow described by the vector plots. The SI results that the longer ‘tails’ in the monophasic velocity waves constitute a noticeable increase in the SI in non-critical areas. Three scenarios lead to a high SI on the surface of the cavity: stagnation is a result of low velocity fluid with high oscillations or extremely low uniform velocity fluid that does not move. A high SI may also arise from low velocity fluid in a uniform direction, which is able to wash away and avoid stagnation. The SI of 1 indicates areas below the threshold for the entire cycle, but offers no measure of the oscillatory nature of the flow. The behaviour explains the difference between the area of stagnation for the SI and RT, especially in the blunt monophasic case, which demonstrates large stagnation on the

proximal third of the stopper surface. The vector plots reveal slow uniform flow in some regions with an SI of 1, which suggests low velocity fluid but not stagnation.

RT was used to predict the size and location of stagnation in the cavity created by the extracorporeal access device. The results in Chapter 4 show the location of stagnation for each of the four physiological velocity waves. The stagnation for all four cases was located on the proximal corner of the cavity. Corners exposed to flow provide an opportunity for recirculation and long residence times, the ideal location for thrombosis.

The RT plots of the four physiological velocity waves show a trend in the area of stagnation as the number of phases decrease from triphasic to biphasic to sharp monophasic. These three waves share a similar initial phase comprising of acceleration flow, peak forward flow, and decelerating flow. The blunt monophasic velocity wave has a considerably different shape and profile, which is reflected in the different flow conditions in the cavity and stagnation on the surface of the stopper.

The area of stagnation was least in the triphasic case and increased as the number of phases in the velocity wave decreased. The area of stagnation in the biphasic and sharp monophasic cases appear to grow from the same location as the triphasic case. The blunt monophasic case produces stagnation in the same location as the other cases, but appears to be a special case.

The area of stagnation in the triphasic case is located on the edge of the cavity centred on the deep corner of the mid-plane. The area of stagnation in the biphasic case has expanded and covers up to one third of the edge of the cavity. The sharp monophasic

area of stagnation is greater again and is still located primarily on the deep corner. The area has expanded and covers a substantial surface area of the stopper surface and wall of the cavity near the deep corner. The areas of stagnation on the surface of the cavity correspond to regions of consistent low velocity in the vector plots.

Based on the RT results it can be seen that a number of factors may contribute to the stagnation in the cavity and raise questions about the position of the device and shape of the cavity. The proximal corner provides the largest area of stagnation in all four cases. The edge of the cavity provides the opportunity for stagnation and the proximal corner is the farthest from the flow in the main vessel.

The shape of the cavity is determined by the angle of the device, and at 45° the proximal corner of the stopper surface is in a much deeper position from the main flow than the distal corner. The stagnation in the deepest section of the cavity would suggest that any increase in depth of the cavity negatively affects the performance of the device. The triphasic and biphasic cases experience the lowest areas of stagnation in the cavity as a result of the reverse flow. The proximity of the device to the stenosis and jetting of flow that occurs during reverse flow may impact the flow conditions in the device and provide the high velocity flow to wash out the cavity.

The greatest reduction in the area of stagnation occurs during the change in flow direction for the triphasic and biphasic cases. The vector plots revealed deep penetration into the proximal cavity during the second phase. The lack of retrograde flow in the monophasic cases removes the flow penetration into the proximal cavity and an increase in the area of stagnation. The blunt monophasic wave, which would be the most likely

wave in these patients, would cause the fully occlusive thrombus seen in the explanted devices.

6.2.2 Vessel Diameter

Another physiological condition, such as the diameter of the vessel, may also be attributed to the lack of thrombosis. Holland et al. [110] determined a significant difference in vessel size between genders with females having a smaller femoral artery compared to males, although both exhibited similar flow rates. The smaller artery exhibits a larger velocity to maintain the same flow rate as the larger vessel. The increased velocity in smaller vessels may account for the different levels of stagnation in the explanted devices. The correlation between the velocity and the area of stagnation in the cavity suggests that the smaller vessel with a larger velocity may contribute to the different outcomes of the explanted extracorporeal access devices.

The graphs of area of stagnation calculated from the SSR show a similar trend throughout the cycle. The area of stagnation at each time step was lower in the 8mm vessel than it was in the 10mm vessel. The correlation for the 8mm vessel also shows that the area of stagnation is dependent on the velocity. The correlation between the velocity and area of stagnation in the 10mm vessel revealed that as the velocity increased the area of stagnation decreased. The smaller vessel has a greater velocity than the 10mm vessel in order to maintain the same flow rate, and may cause the area of stagnation to be lower during similar flow conditions.

The vector plots were analysed at specific time steps in the cycle that correspond to the smallest area of stagnation in each phase. The results were compared to the flow

conditions in the vessel with the 10mm diameter. The flow conditions at these time steps showed the same flow conditions exist within the cavity but with an increase in velocity. The increased velocity accounts for a greater penetration into the corners of the cavity and a reduction in the area of stagnation. The first phase in the triphasic, biphasic and sharp monophasic waves create similar flow conditions in the cavity and reduce the stagnation in the distal corner. The reverse flow in the triphasic and biphasic cases also result in similar flow conditions and the same as those in the 10mm vessel. The reverse flow reduces the stagnation in the proximal corner and similar to the 10mm case the absence of reverse flow increases the likelihood that the proximal corner experiences stagnation and thromboses.

The comparison of the SI plots on the surface of the cavity reveal that the area of stagnation and the average SI are smaller in the 8mm vessel than the 10mm vessel. The RT results for the triphasic, biphasic and sharp monophasic show a similar trend to the 10mm case as the number of phases decreases the area of stagnation grows from the proximal corner. The RT reveals a lower area of stagnation for all the physiological waves in the smaller vessel.

The correlation between velocity and area of stagnation reveals that as the velocity of the flow increases the area of stagnation tends to decrease. The smaller vessel generates higher velocities than the large vessel and may account for the lower area of stagnation in the first phase. The acceleration also showed a correlation with the area of stagnation, and the increased deceleration as the flow changes direction in the smaller vessel may account for the lower area of stagnation in the second phase. These two stages of the

velocity profile combined results in a lower area of stagnation in the smaller vessel than the larger vessel.

6.3 GEOMETRICAL FACTORS

RT was used to determine the optimal position of the device for different physiological conditions.

6.3.1 Distance

The vector plots, SSR threshold, SI and RT were used to compare the flow conditions in the cavity as a result of the different distances the device was placed from the stenosis. The vector plots showed the same flow conditions and the SSR showed the same area of stagnation at each time step in the cycle for the three cases. The RT and area of stagnation were used to show that the risk of thrombosis was the same in all three cases and the proximity of the device to the stenosis had no effect on the flow in the cavity.

6.3.2 Depth

The depth of the cavity was analysed to determine how the flow conditions develop further from the main flow. The stagnation in the cavity occurred in the deepest corner in the cavity from the main flow in the vessel, which suggests that minimising the depth of the cavity will reduce the stagnation, just as increasing the depth will increase stagnation.

The SSR shows a similar trend in the area of stagnation for three depths and physiological waves. The waves experience the same reduction in stagnation during the peak forward flow in the first phase and change in direction during the second phase.

The vector plots show the same flow conditions in the cavity, but the increase in depth allows the flow to develop further into the cavity. The increase in fluid within the cavity creates more fluid for the main flow to move and results in lower velocities on the surface. The lower velocities on the surface increase the SI surface in non-critical areas. The size of the area of stagnation also increases as the low velocity regions in the cavity increase.

The blunt monophasic wave experiences low velocity flow on the majority of the stopper surface, but the low velocity regions do not always correspond to an increase in stagnation. The low velocity region flows in a uniform direction and allows the fluid to flow out and not stagnate.

6.3.3 Angle

The angle of the device was used to provide easy access to the femoral artery for the treatment of peripheral arterial disease. The cavity created by the device in the closed state resulted in thrombus formation in some of the explanted devices due to different physiological factors. The different results from the explanted devices suggest that the cavity of the device is not optimal for all of the different physiological waves. Changing the angle of the device considerably changes the shape of the cavity and may reduce the risk of thrombosis as a result of the flow conditions within. The angle of the device was analysed using the different physiological waves to determine which position of the device created the smallest area of stagnation for each wave. The angle changes the geometry of the cavity completely and causes different flow conditions. Different angles present a more suitable cavity to minimise stagnation for each physiological wave.

The device at 45° allowed the flow to push up and into the cavity in the first phase during the acceleration for the triphasic, biphasic and sharp monophasic waves. The flow in the first phase created a vortex close to the entrance of the cavity and flushed out the distal corner of the cavity, but creates recirculation in the proximal corner. The reverse flow in the 45° promoted high velocity fluid in the cavity that was pushed up and into the proximal corner, but isolated the distal corner, creating a low velocity region. Together, the two phases caused the greatest reduction in stagnation in the cavity. The lack of reverse flow in the monophasic case, coupled with lower velocities resulted in larger areas of stagnation.

The device positioned at 90° to the vessel creates a much smaller cavity than the original position of the device. The smaller cavity at 90° provides a greater opportunity for the cavity to be flushed out, but the angle may isolate the proximal corner from the first phase flow. The reverse flow in 90° cavity was expected to penetrate the cavity in the same way as the 45° and isolate the distal corner. The flow was predicted to wash out the proximal corner but not the distal corner.

The vector plots show similar results to the 45° case. The triphasic, biphasic, and sharp monophasic waves show similar flow conditions during the first phase with the difference in velocity again causing the difference in size of the low velocity regions in the cavity. The first phase was effective at washing out the distal corner and the second phase was effective at washing out the proximal corner. The change in direction caused the greatest disturbance in the entire cycle and the acceleration and peak flow contributed to the greatest disturbance in the first phase. The accelerating fluid pushes flow up into the cavity creating recirculation on the proximal corner and flushing out

the distal corner. The flow at the wall reverses before the change in direction of the main flow resulting in similar flow as the acceleration flow but in the opposite direction. The reverse flow flushes out the fluid in the proximal corner, but causes recirculation in the distal corner. The 90° angle provides a smaller opportunity for stagnation due to the smaller size, but the angle makes it easier for recirculation regions to form in the corners. The triphasic and biphasic waves create slightly larger areas of stagnation compared to the 45° . The reverse flow creates a vortex that flushes out the proximal corner in the 45° case, compared to the low velocity flow left in the 90° case. The shallow cavity of the 90° case allows the forward flow from the monophasic cases to penetrate and wash out the distal corner. The shape of the cavity and positive flow of the monophasic waves allows the walls to experience mostly uniform flow. With the device at 90° the volume of fluid is reduced and the increased velocity near the corners in combination with the uniform flow allows the fluid to wash out and not stagnate. The device at 90° to the vessel is a better placement for the sharp monophasic and blunt monophasic velocity waves, indicated by the reduction in area of stagnation.

Compared to the 45° and 90° cases, the 135° geometry of the cavity appears to provide the optimal geometry for the reverse flow to wash out the cavity, but not much opportunity for the forward flow to do so. The vector plots reveal that the first phase of the velocity waves flows into the cavity towards the distal wall and isolates fluid on the surface of the cavity. The flow is unable to wash out either corner and presents a low velocity region during the first phase. The reverse flow allows fluid to push up into the cavity and wash out the proximal corner of the cavity and also creates the greatest disturbance in the distal corner for the entire cycle. Due to the angle of the device the

reverse flow in the triphasic and biphasic cases creates the greatest disturbance to the stagnation in both the proximal and distal corners.

The slow continuous flow of the blunt monophasic wave isolates the majority of the fluid in the cavity from the main flow. Similar to the 45° case the flow in the cavity is trapped in a low velocity anti-clockwise vortex low in the cavity. The flow does not penetrate near the corners of the cavity and the RT shows the area of stagnation located on the entire corner of the stopper surface.

The RT reveals a smaller area of stagnation for the triphasic case along the mid-plane of the cavity, but larger regions of stagnation to the sides of the cavity on the stopper surface. The area of stagnation increases for all cases in the 135° case, except for the biphasic velocity wave, which produces the smallest area of stagnation of the three angles. The angle of the device at 135° provides a greater washout of the cavity during the reverse flow of the biphasic velocity wave.

6.4 EXPLANTED EXTRACORPOREAL ACCESS DEVICES

All of the thrombi in the explanted devices were identified as red blood clots. Red blood clots are composed predominantly of red blood cells and a fibrin mesh and occur due to stagnation in the flow. Thrombosis due to stagnation usually occurs in the venous system, except in circumstances where irregular flow conditions develop, such as an abnormal geometry. Aneurysms, stenoses, and medical implants such as stents can all cause disturbed flow conditions and lead to thrombosis. The thrombi in the explanted devices suggest that thrombus formation begins in the deepest corner of the cavity and

grows both into the cavity and along the edge of the stopper surface, before covering the surface of the stopper completely.

The explanted extracorporeal access devices provide evidence that support an investigation of the different physiological and geometrical conditions that could impact the risk of thrombus formation in the cavity of the device. Explanted devices from five patients were available for analysis and demonstrated results that suggest physiological conditions affect the risk of thrombosis in the cavity. Two of the devices developed an occlusive thrombosis within the cavity that covered the entire surface of the stopper. Two more devices demonstrated the onset of thrombus formation; one case revealing thrombus formation in the deepest corner of the cavity and the other with thrombosis extending to the entire edge of the stopper surface. The last device exhibited no sign of thrombus formation in the cavity at all. The four cases with thrombosis suggest that the device position and location was optimised for the treatment of peripheral arterial disease and that unexpected patient specific conditions existed within the femoral artery to result in thrombus formation.

The explanted devices suggest that physiological factors contribute towards supporting or inhibiting thrombus formation. The devices were all implanted at the same angle upstream of a stenosis, but showed different results implanted in different patients. This suggests that one or more physiological conditions impact the risk of thrombosis and its rate of growth. The physiological factors that can affect the performance of the device are the velocity wave and the size of the vessel.

The area of stagnation predicted by the computational models predicted similar locations and sizes as those in the explanted devices.

- The area of stagnation predicted in the sharp monophasic wave matched the thrombus formation (in the deepest corner) in the explanted device of patient #2.
- The area of stagnation predicted in the blunt monophasic wave matched the region of thrombus formation (around the circumference) in the explanted device of patient #3.
- The thrombus formation (fully occlusive) in the explanted devices of patients #4 and #5 suggest the thrombus formation initiated in the same region as the area predicted in the blunt monophasic wave and progressed along the edge of the stopper and over the surface of the cavity.

CHAPTER 7 - CONCLUSIONS

In conclusion, the research presented investigated the effect of physiological and geometrical factors on the risk of thrombus formation in an extracorporeal access device. The main findings showed:

The different pulsatile conditions in the four physiological velocity waves affect the likelihood of thrombus formation. The presence of retrograde flow reduced the likelihood of thrombus formation in the biphasic case, compared to the monophasic cases, and eliminated it completely in the triphasic case.

A progression in the likelihood of thrombus formation as the integrity of the physiological wave degraded from triphasic to biphasic to sharp monophasic. It also revealed the extreme nature of a blunt monophasic wave with the substantial increase in likelihood of thrombus formation in comparison to the sharp monophasic wave.

The different geometrical configurations of the device attached to the femoral artery affect the likelihood of thrombus formation in the extracorporeal access device. The angle of the device has the greatest impact on the flow in the cavity and thrombus formation, and it was shown that increasing the depth of the cavity created by the device increases the likelihood of thrombus formation. It was also shown that the distance of the device upstream from the stenosis had no effect on the likelihood of thrombus formation.

The increased velocity in smaller femoral arteries reduces the likelihood of thrombus formation for all of the physiological waves.

The findings presented in this research can be used to benefit the clinical application and prescription of the device for the hyper-perfusion treatment. The angle of the device can be adapted to suit the physiological wave exhibited by patients and decrease the likelihood of thrombus formation. The predicted area of thrombus formation for the biphasic, sharp monophasic, and blunt monophasic waves was minimised when the device was positioned at 90° to the femoral artery. The predicted area of thrombus formation was extremely low at 90° and 135° for the triphasic wave, but was non-existent at 45° , making the latter angle the most appropriate for patients exhibiting this physiological wave.

In the presence of numerous studies that validate techniques for predicting thrombus formation, this thesis has examined the role of physiological factors on thrombus formation. By exploring the effect of physiological flow in thrombus formation, this work will provide guidance for the design of medical devices exposed to vascular flow and assist in appropriate prescription of medical devices at a patient-specific level.

7.1 FUTURE WORK

This thesis has initiated the investigation on the effect of physiological conditions on thrombus formation. In particular it focused on the effect of the pulsatility of different physiological waves on thrombus formation. It is evident that further work is required to complete the overall project. This can be achieved in two ways: improving the quality

of the computational model, including a proper patient study, and conducting an experimental analysis that could validate the findings of the computational model.

The computational model incorporated a Newtonian fluid to simulate blood flow in a rigid wall cylindrical vessel that simulated a diseased femoral artery. These conditions were used to provide a foundation for the analysis of the effect of physiological wave and device configurations on the effect of thrombus formation in an extracorporeal access device. The results showed the effect of physiological flow on thrombus formation and have opened the door for a more detailed analysis of the project.

The computational model can be improved by incorporating a non-Newtonian fluid that accurately simulates blood flow over a diverse range of shear rates. The flow of the computational model can include patient specific waveforms for explanted devices that showed signs of thrombus formation. The geometry of the model could be improved in several ways including: physiologically accurate or patient specific stenoses, physiologically accurate or patient specific dimensions for a diseased femoral artery.

The thesis used a computational model to determine the effect of physiological waves on thrombus formation and it would be complemented well by an experimental analysis. Experimental results that validate the computational model would be the first step in the progression of this project and a better understanding of the effect of physiological factors on thrombus formation.

REFERENCES

1. Jude, E.B., et al., *Peripheral arterial disease in diabetic and nondiabetic patients*. Diabetes care, 2001. **24**(8): p. 1433-1437.
2. Hirsch, A.T., et al., *Peripheral arterial disease detection, awareness, and treatment in primary care*. JAMA: the journal of the American Medical Association, 2001. **286**(11): p. 1317-1324.
3. Ouriel, K., *Peripheral arterial disease*. The lancet, 2001. **358**(9289): p. 1257-1264.
4. McDermott, M.M.G., et al., *Leg symptoms in peripheral arterial disease*. JAMA: the journal of the American Medical Association, 2001. **286**(13): p. 1599-1606.
5. Gornik, H.L. and J.A. Beckman, *Peripheral arterial disease*. Circulation, 2005. **111**(13): p. e169-e172.
6. Green, S. and J. Mehlsen, *Peripheral arterial disease*. Exercise and Circulation in Health and Disease, 1999.
7. Golomb, B.A., T.T. Dang, and M.H. Criqui, *Peripheral arterial disease*. Circulation, 2006. **114**(7): p. 688-699.
8. Makin, A., S. Silverman, and G. Lip, *Peripheral vascular disease and Virchow's triad for thrombogenesis*. Qjm, 2002. **95**(4): p. 199-210.
9. Baumgartner, I., R. Schainfeld, and L. Graziani, *Management of peripheral vascular disease*. Annu. Rev. Med., 2005. **56**: p. 249-272.
10. Ogedegbe, H.O., *An overview of hemostasis*. Laboratory Medicine, 2002. **33**(12): p. 948-953.
11. Mackman, N., R.E. Tilley, and N.S. Key, *Role of the extrinsic pathway of blood coagulation in hemostasis and thrombosis*. Arteriosclerosis, Thrombosis, and Vascular Biology, 2007. **27**(8): p. 1687-1693.
12. Gailani, D. and T. RennÅ©, *Intrinsic pathway of coagulation and arterial thrombosis*. Arteriosclerosis, Thrombosis, and Vascular Biology, 2007. **27**(12): p. 2507-2513.
13. Pasi, K.J., *Hemostasis: Components and Processes*. Methods in Molecular Medicine, 1999. **31**: p. 3-21.
14. Sere, K.M. and T.M. Hackeng, *Basic mechanisms of hemostasis*. Seminars in Vascular Medicine, 2003. **3**(1): p. 3-12.
15. Pasi, K., *Hemostasis: components and processes*. Methods in Molecular Medicine, 1999. **31**: p. 3.
16. McMichael, M., *Primary hemostasis*. Journal of Veterinary Emergency and Critical Care, 2005. **15**(1): p. 1-8.
17. Wootton, D.M. and D.N. Ku, *Fluid mechanics of vascular systems, diseases, and thrombosis*, in *Annual Review of Biomedical Engineering* 1999. p. 299-329.
18. Furie, B. and B.C. Furie, *Mechanisms of thrombus formation*. New England Journal of Medicine, 2008. **359**(9): p. 938-949.
19. Nieswandt, B., I. Pleines, and M. Bender, *Platelet adhesion and activation mechanisms in arterial thrombosis and ischaemic stroke*. Journal of Thrombosis and Haemostasis, 2011. **9**(1 S): p. 92-104.

20. Roderique, E. and J. Wynands, *Blood coagulation and haemostasis: A review*. Canadian Journal of Anesthesia / Journal of Anesthesia, 1967. **14**(2): p. 129-151.
21. Troy, G.C., *An overview of hemostasis*. Veterinary Clinics of North America - Small Animal Practice, 1988. **18**(1): p. 5-20.
22. Gentry, P.A., *Comparative aspects of blood coagulation*. Veterinary Journal, 2004. **168**(3): p. 238-251.
23. Hoffman, M. and D.M. Monroe, *Coagulation 2006: A Modern View of Hemostasis*. Hematology/Oncology Clinics of North America, 2007. **21**(1): p. 1-11.
24. Boon, G.D., *An overview of hemostasis*. Toxicologic Pathology, 1993. **21**(2): p. 170-179.
25. Kumar, D.R., et al., *Virchow's contribution to the understanding of thrombosis and cellular biology*. Clinical Medicine and Research, 2010. **8**(3-4): p. 168-172.
26. Favalaro, E.J. and G. Lippi, *Coagulation update: What's new in hemostasis testing?* Thrombosis Research, 2011. **127**(SUPPL. 2): p. S13-S16.
27. Gosling, R., et al., *The quantitative analysis of occlusive peripheral arterial disease by a non-intrusive ultrasonic technique*. Angiology, 1971. **22**(1): p. 52-55.
28. Spronk, S., et al., *Value of the duplex waveform at the common femoral artery for diagnosing obstructive aortoiliac disease*. Journal of Vascular Surgery, 2005. **42**(2): p. 236-242.
29. O'Neill, S., et al., *Do Doppler waveforms at the common femoral artery accurately predict iliac stenosis?* Irish Journal of Medical Science, 2010. **180**(1): p. 247-249.
30. Bluestein, D., *Research approaches for studying flow-induced thromboembolic complications in blood recirculating devices*. Expert Review of Medical Devices, 2004. **1**(1): p. 65-80.
31. Rasche, H., *Haemostasis and thrombosis: An overview*. European Heart Journal, Supplement, 2001. **3**(Q): p. Q3-Q7.
32. Asztalos, B., et al., *Evaluation of shear and recirculation in centrifugal artificial heart by flow visualization*. Journal of Visualization, 2000. **3**(1): p. 79-92.
33. Blackshear, P.L., et al., *A role of flow separation and recirculation in thrombi formation on prosthetic surfaces*. AIAA 9th Aerospace Sciences Meeting, Paper, 1971. **71-103**.
34. Corbett, S.C., et al., *Effect of pulsatile blood flow on thrombosis potential with a step wall transition*. ASAIO Journal, 2010. **56**(4): p. 290-295.
35. Corbett, S.C., et al., *In vitro and computational thrombosis on artificial surfaces with shear stress*. Artificial Organs, 2010. **34**(7): p. 561-569.
36. Day, S.W., et al., *A prototype heartquest ventricular assist device for particle image velocimetry measurements*. Artificial Organs, 2002. **26**(11): p. 1002-1005.
37. Debaene, P., et al., *Determining wall shear stress in artificial blood pumps of heart assist devices*. Bestimmung der Wandschubspannung in künstlichen Blutpumpen von Herzunterstützungssystemen., 2002. **47 Suppl 1 Pt 1**: p. 140-141.
38. Fallon, A.M., et al., *Procoagulant properties of flow fields in stenotic and expansive orifices*. Annals of Biomedical Engineering, 2008. **36**(1): p. 1-13.

39. Gay, M. and L. Zhang, *Numerical studies of blood flow in healthy, stenosed, and stented carotid arteries*. International Journal for Numerical Methods in Fluids, 2009. **61**(4): p. 453-472.
40. Kuramochi, Y., et al., *Hemodynamic factors of thrombus formation in coronary aneurysms associated with Kawasaki disease*. Pediatrics International, 2000. **42**(5): p. 470-475.
41. Tavoularis, S., et al., *Towards optimal control of blood flow in artificial hearts*. Cardiovascular Engineering, 2003. **8**(1-2): p. 20-31.
42. Triep, M., et al., *Investigation of the washout effect in a magnetically driven axial blood pump*. Artificial Organs, 2008. **32**(10): p. 778-784.
43. Yoganathan, A.P. and W.H. Corcoran, *In vitro velocity measurements in the near vicinity of the Bjork-Shiley aortic prosthesis using a laser-Doppler anemometer*. Medical and Biological Engineering and Computing, 1979. **17**(4): p. 453-459.
44. Kakalis, N.M.P., et al., *The haemodynamics of endovascular aneurysm treatment: A computational modelling approach for estimating the influence of multiple coil deployment*. IEEE Transactions on Medical Imaging, 2008. **27**(6): p. 814-824.
45. Rayz, V.L., et al., *Numerical modeling of the flow in intracranial aneurysms: Prediction of regions prone to thrombus formation*. Annals of Biomedical Engineering, 2008. **36**(11): p. 1793-1804.
46. Longest, P.W. and C. Kleinstreuer, *Comparison of blood particle deposition models for non-parallel flow domains*. Journal of Biomechanics, 2003. **36**(3): p. 421-430.
47. Friedrich, P. and A.J. Reininger, *Occlusive thrombus formation on indwelling catheters: In vitro investigation and computational analysis*. Thrombosis and Haemostasis, 1995. **73**(1): p. 66-72.
48. Brinjikji, W., et al., *Patient outcomes are better for unruptured cerebral aneurysms treated at centers that preferentially treat with endovascular coiling: A study of the national inpatient sample 2001-2007*. American Journal of Neuroradiology. **32**(6): p. 1065-1070.
49. Kurre, W. and J. Berkefeld, *Materials and techniques for coiling of cerebral aneurysms: How much scientific evidence do we have?* Neuroradiology, 2008. **50**(11): p. 909-927.
50. Mitsos, A.P., et al., *Haemodynamic simulation of aneurysm coiling in an anatomically accurate computational fluid dynamics model: Technical note*. Neuroradiology, 2008. **50**(4): p. 341-347.
51. Bashir, J., et al., *Thrombosis and failure of a HeartMate II Device in the absence of alarms*. Journal of Heart and Lung Transplantation.
52. Fraser, K.H., et al., *The use of computational fluid dynamics in the development of ventricular assist devices*. Medical Engineering and Physics. **33**(3): p. 263-280.
53. Potapov, E.V., et al., *Managing long-term complications of left ventricular assist device therapy*. Current Opinion in Cardiology. **26**(3): p. 237-244.
54. Hellgren, L., et al., *Biological versus mechanical prosthesis in 3279 patients from the Swedish in-patients register*. Scandinavian Cardiovascular Journal. **45**(4): p. 223-228.

55. Kaufmann, T.A.S., et al., *Transient, three-dimensional flow field simulation through a mechanical, trileaflet heart valve prosthesis*. ASAIO Journal. **57**(4): p. 278-282.
56. Voegelé-Kadletz, M. and E. Wolner, *Bio artificial surfaces - Blood surface interaction*. Materials Science and Engineering C. **31**(6): p. 1195-1200.
57. Rajendran, S., et al., *High on Treatment Platelet Reactivity and Stent Thrombosis*. Heart Lung and Circulation. **20**(8): p. 525-531.
58. Willis, N., R. Sachdeva, and B.F. Uretsky, *Bare-metal stent thrombosis after noncardiac surgery greater than 10 years after stent implantation*. Catheterization and Cardiovascular Interventions. **78**(2): p. 234-236.
59. Texon, M., A.M. Imparato, and M. Helpert, *The role of vascular dynamics in the development of atherosclerosis*. Journal of the American Medical Association, 1965. **194**(11): p. 1226-1230.
60. Müller-Mohnssen, H., *Experimental results to the deposition hypothesis of atherosclerosis*. Thrombosis Research, 1976. **8**(5): p. 553-566.
61. Caro, C.G., J.M. Fitz-Gerald, and R.C. Schroter, *Atheroma and arterial wall shear. Observation, correlation and proposal of a shear dependent mass transfer mechanism for atherogenesis*. Proceedings of the Royal Society of London. Series B. Biological sciences, 1971. **177**(46): p. 109-159.
62. Rayz, V.L., et al., *Flow residence time and regions of intraluminal thrombus deposition in intracranial aneurysms*. Annals of Biomedical Engineering, 2010. **38**(10): p. 3058-3069.
63. Chopard, B., et al., *Lattice Boltzmann modeling of thrombosis in giant aneurysms*. International Journal of Modern Physics C, 2007. **18**(4): p. 712-721.
64. Gambaruto, A.M., D.J. Doorly, and T. Yamaguchi, *Wall shear stress and near-wall convective transport: Comparisons with vascular remodelling in a peripheral graft anastomosis*. Journal of Computational Physics, 2010. **229**(14): p. 5339-5356.
65. Sui, B., et al., *Blood flow pattern and wall shear stress in the internal carotid arteries of healthy subjects*. Acta Radiologica, 2008. **49**(7): p. 806-814.
66. Zhu, G.Y., Q. Yuan, and Z. Chen. *Experimental investigation of blood flow in the vertebral artery bifurcation*. in *IFMBE Proceedings*. 2010.
67. Ku, D.N., et al., *Pulsatile flow and atherosclerosis in the human carotid bifurcation. Positive correlation between plaque location and low oscillating shear stress*. Arterioscler Thromb Vasc Biol, 1985. **5**(3): p. 293-302.
68. He, X. and D.N. Ku, *Pulsatile flow in the human left coronary artery bifurcation: Average conditions*. Journal of Biomechanical Engineering, 1996. **118**(1): p. 74-82.
69. Box, F.M.A., et al., *The influence of flow, vessel diameter, and non-Newtonian blood viscosity on the wall shear stress in a carotid bifurcation model for unsteady flow*. Investigative Radiology, 2005. **40**(5): p. 277-294.
70. Cheng, C., et al., *Atherosclerotic lesion size and vulnerability are determined by patterns of fluid shear stress*. Circulation, 2006. **113**(23): p. 2744-2753.
71. Huo, Y., T. Wischgol, and G.S. Kassab, *Flow patterns in three-dimensional porcine epicardial coronary arterial tree*. American Journal of Physiology - Heart and Circulatory Physiology, 2007. **293**(5): p. H2959-H2970.

72. Kim, Y.H., et al., *Hemodynamic analysis of a compliant femoral artery bifurcation model using a fluid structure interaction framework*. Annals of Biomedical Engineering, 2008. **36**(11): p. 1753-1763.
73. Moore, J.E., et al., *Fluid wall shear stress measurements in a model of the human abdominal aorta: oscillatory behavior and relationship to atherosclerosis*. Atherosclerosis, 1994. **110**(2): p. 225-240.
74. Papaharilaou, Y., et al., *A decoupled fluid structure approach for estimating wall stress in abdominal aortic aneurysms*. Journal of Biomechanics, 2007. **40**(2): p. 367-377.
75. Redaelli, A., et al., *Flow dynamics of the St Jude Medical Symmetry aortic connector vein graft anastomosis do not contribute to the risk of acute thrombosis*. Journal of Thoracic and Cardiovascular Surgery, 2004. **128**(1): p. 117-123.
76. Torii, R., et al., *Fluid-structure interaction analysis of a patient-specific right coronary artery with physiological velocity and pressure waveforms*. Communications in Numerical Methods in Engineering, 2009. **25**(5): p. 565-580.
77. Wu, S.P., et al., *Wall Shear Rates Differ between the Normal Carotid, Femoral, and Brachial Arteries: An In Vivo MRI Study*. Journal of Magnetic Resonance Imaging, 2004. **19**(2): p. 188-193.
78. Himburg, H.A., et al., *Spatial comparison between wall shear stress measures and porcine arterial endothelial permeability*. American Journal of Physiology - Heart and Circulatory Physiology, 2004. **286**(5): p. H1916-H1922.
79. Lee, S.W., L. Antiga, and D.A. Steinman, *Correlations among indicators of disturbed flow at the normal carotid bifurcation*. Journal of Biomechanical Engineering, 2009. **131**(6).
80. Fraser, K.H., et al., *Computational fluid dynamics analysis of thrombosis potential in left ventricular assist device drainage cannulae*. ASAIO journal (American Society for Artificial Internal Organs: 1992), 2010. **56**(3): p. 157.
81. Chopard, B., et al., *Lattice Boltzmann modeling of thrombosis in giant aneurysms*. International Journal of Modern Physics C, 2007. **18**(4): p. 712-721.
82. Zhang, Y., et al., *Design optimization of an axial blood pump with computational fluid dynamics*. ASAIO Journal, 2008. **54**(2): p. 150.
83. Goubergrits, L., et al., *Estimation of wall shear stress in bypass grafts with computational fluid dynamics method*. The International journal of artificial organs, 2001. **24**(3): p. 145.
84. Chopard, B., R. Ouared, and D.A. Rüfenacht, *A lattice Boltzmann simulation of clotting in stented aneurysms and comparison with velocity or shear rate reductions*. Mathematics and Computers in Simulation, 2006. **72**(2): p. 108-112.
85. Yoganathan, A.P., W.H. Corcoran, and E.C. Harrison, *In vitro velocity measurements in the vicinity of aortic prostheses*. Journal of Biomechanics, 1979. **12**(2): p. 135-152.
86. Tamagawa, M., et al., *Simulation of thrombus formation in shear flows using lattice boltzmann method*. Artificial Organs, 2009. **33**(8): p. 604-610.
87. LIU, Z., et al., *Influence of Blood Flow on Thrombosis in Y-Bifurcation Coronary Arteries*. Journal of Beijing University of Technology, 2010.
88. Goodman, P.D., et al., *Computational model of device-induced thrombosis and thromboembolism*. Annals of biomedical engineering, 2005. **33**(6): p. 780-797.

89. Filipovic, N., M. Kojic, and A. Tsuda, *Modelling thrombosis using dissipative particle dynamics method*. Philosophical Transactions of the Royal Society A: Mathematical, Physical and Engineering Sciences, 2008. **366**(1879): p. 3265-3279.
90. Bluestein, D., et al., *Fluid mechanics of arterial stenosis: relationship to the development of mural thrombus*. Annals of Biomedical Engineering, 1997. **25**(2): p. 344-356.
91. Bedekar, A.S., et al., *A computational model combining vascular biology and haemodynamics for thrombosis prediction in anatomically accurate cerebral aneurysms*. Food and Bioproducts Processing, 2005. **83**(2 C): p. 118-126.
92. Sorensen, E.N., et al., *Computational simulation of platelet deposition and activation: I. Model development and properties*. Annals of biomedical engineering, 1999. **27**(4): p. 436-448.
93. Kamada, H., et al., *A three-dimensional particle simulation of the formation and collapse of a primary thrombus*. International Journal for Numerical Methods in Biomedical Engineering, 2010. **26**(3-4): p. 488-500.
94. Burgreen, G.W., et al., *Computational fluid dynamics as a development tool for rotary blood pumps*. Artificial organs, 2001. **25**(5): p. 336-340.
95. Bernsdorf, J., et al., *Applying the lattice Boltzmann technique to biofluids: A novel approach to simulate blood coagulation*. Computers & Mathematics with Applications, 2008. **55**(7): p. 1408-1414.
96. Harrison, S., et al., *Application and validation of the lattice Boltzmann method for modelling flow-related clotting*. Journal of Biomechanics, 2007. **40**(13): p. 3023-3028.
97. Redaelli, A., et al., *Flow dynamics of the St Jude Medical Symmetry aortic connector vein graft anastomosis do not contribute to the risk of acute thrombosis*. The Journal of Thoracic and Cardiovascular Surgery, 2004. **128**(1): p. 117-123.
98. Worth Longest, P. and C. Kleinstreuer, *Comparison of blood particle deposition models for non-parallel flow domains*. Journal of Biomechanics, 2003. **36**(3): p. 421-430.
99. Kunov, M.J., D. Steinman, and C.R. Ethier, *Particle volumetric residence time calculations in arterial geometries*. Journal of Biomechanical Engineering, 1996. **118**: p. 158.
100. Hyun, S., C. Kleinstreuer, and J. Archie Jr, *Hemodynamics analyses of arterial expansions with implications to thrombosis and restenosis*. Medical engineering & physics, 2000. **22**(1): p. 13-27.
101. Lee, K.W. and X.Y. Xu, *Modelling of flow and wall behaviour in a mildly stenosed tube*. Medical Engineering and Physics, 2002. **24**(9): p. 575-586.
102. Buntin, C.M. and F.H. Silver, *Noninvasive assessment of mechanical properties of peripheral arteries*. Annals of Biomedical Engineering, 1990. **18**(5): p. 549-566.
103. Niroomand Oscuii, H., M. Tafazzoli Shadpour, and F. Ghalichi, *Flow characteristics in elastic arteries using a fluid-structure interaction model*. American Journal of Applied Sciences, 2007. **4**(8): p. 516-524.
104. Migliavacca, F. and G. Dubini, *Computational modeling of vascular anastomoses*. Biomechanics and Modeling in Mechanobiology, 2005. **3**(4): p. 235-250.

105. Liu, Q., D. Mirc, and B.M. Fu. *Mechanical mechanisms for thrombosis in microvessels*. in *Annual International Conference of the IEEE Engineering in Medicine and Biology - Proceedings*. 2006. New York, NY.
106. Bathe, M. and R.D. Kamm, *A fluid-structure interaction finite element analysis of pulsatile blood flow through a compliant stenotic artery*. *Journal of Biomechanical Engineering*, 1999. **121**(4): p. 361-369.
107. Steinman, D.A., et al., *A numerical simulation of flow in a two-dimensional end-to-side anastomosis model*. *Journal of Biomechanical Engineering*, 1993. **115**(1): p. 112-118.
108. Ahmed, S.A. and D.P. Giddens, *Pulsatile poststenotic flow studies with laser Doppler anemometry*. *Journal of Biomechanics*, 1984. **17**(9): p. 695-705.
109. Moore, K.L. and A.F. Dalley, *Clinically Oriented Anatomy*. 5th ed. 2006, United States of America: Lippincott Williams & Wilkins.
110. Holland, C.K., et al., *Lower extremity volumetric arterial blood flow in normal subjects*. *Ultrasound in Medicine and Biology*, 1998. **24**(8): p. 1079-1086.
111. Lewis, P., et al., *Measurement of volume flow in the human common femoral artery using a duplex ultrasound system*. *Ultrasound in Medicine and Biology*, 1986. **12**(10): p. 777-784.
112. Lippi, G., M. Franchini, and G. Targher, *Arterial thrombus formation in cardiovascular disease*. *Nature Reviews Cardiology*, 2011.
113. Carpentier, A., *A Blood Sticky Problem*. *New Scientist*, 1976. **72**(1029): p. 524-526.
114. Ahmed, S.A. and D.P. Giddens, *Velocity measurements in steady flow through axisymmetric stenoses at moderate Reynolds numbers*. *Journal of Biomechanics*, 1983. **16**(7): p. 505-516.
115. Ryval, J., A.G. Straatman, and D.A. Steinman, *Two-equation turbulence modeling of pulsatile flow in a stenosed tube*. *Journal of Biomechanical Engineering*, 2004. **126**(5): p. 625-635.
116. Suh, G.Y., et al., *Quantification of particle residence time in abdominal aortic aneurysms using magnetic resonance imaging and computational fluid dynamics*. *Annals of Biomedical Engineering*, 2011. **39**(2): p. 864-883.
117. Basciano, C., et al., *A relation between near-wall particle-hemodynamics and onset of thrombus formation in abdominal aortic aneurysms*. *Annals of Biomedical Engineering*, 2011. **39**(7): p. 2010-2026.